

AD-A283 695



①

NAVAL POSTGRADUATE SCHOOL

Monterey, California



DISSERTATION

COMPUTER SIMULATION OF WAVE PROPAGATION
THROUGH TURBULENT MEDIA

by

Charles A. Davis

June 1994

Dissertation Supervisor:

D.L. Walters

Approved for public release; distribution is unlimited.

155128
94-28014

94 8 30 022

REPORT DOCUMENTATION PAGE

Form Approved
OMB No. 0704-0188

Public reporting burden for this collection of information is estimated to average 1 hour per response, including the time for reviewing instructions, searching existing data sources, gathering and maintaining the data needed, and completing and reviewing the collection of information. Send comments regarding this burden estimate or any other aspect of this collection of information, including suggestions for reducing the burden, to Washington Headquarters Services, Directorate for Information Operations and Reports, 1215 Jefferson Davis Highway, Suite 1204, Arlington, VA 22202-4302, and to the Office of Management and Budget, Paperwork Reduction Project (0704-0188), Washington, DC 20503.

1. AGENCY USE ONLY (Leave blank)		2. REPORT DATE JUN 94		3. REPORT TYPE AND DATES COVERED Ph.D. Dissertation	
4. TITLE AND SUBTITLE COMPUTER SIMULATION OF WAVE PROPAGATION THROUGH TURBULENT MEDIA				5. FUNDING NUMBERS	
6. AUTHOR(S) Davis, Charles A., in conjunction with Walters, D. L.					
7. PERFORMING ORGANIZATION NAME(S) AND ADDRESS(ES) Naval Postgraduate School Monterey, CA 93943-5000				8. PERFORMING ORGANIZATION REPORT NUMBER	
9. SPONSORING/MONITORING AGENCY NAME(S) AND ADDRESS(ES) United States Air Force Phillips Laboratory Kirtland Air Force Base Albuquerque, New Mexico 87117				10. SPONSORING/MONITORING AGENCY REPORT NUMBER	
11. SUPPLEMENTARY NOTES The views expressed in this dissertation are those of the author and do not reflect the official policy or position of the Department of Defense or the U.S. Government.					
12a. DISTRIBUTION/AVAILABILITY STATEMENT Approved for public release; distribution is unlimited.				12b. DISTRIBUTION CODE	
13. ABSTRACT This research used Huygens-Fresnel wave optics computer simulations to investigate the effects of high turbulence strength and inner scale on the normalized irradiance variance and coherence length of electromagnetic waves propagating through a turbulent atmosphere. These investigations developed several guidelines for validity of propagation simulations employing a numerical, split-step, Huygens-Fresnel, method, and within these guidelines, considered five types of turbulence spectrum inner scale: (1) zero inner scale, (2) Gaussian inner scale, (3) Hill's and (4) Frehlich's viscous-convective enhancement inner scales, and (5) turbulence spectrum truncation from the discrete grid representation. The simulation results showed that the normalized irradiance variance generally decreased (~30%) below the zero inner scale values in the Rytov regime with increasing inner scale size, but increased in the saturation regime, and agreed within 2% of the Rytov-Tatarski predictions at low turbulence strengths. The E-field coherence length in a spatially confined beam, with either spherical or plane wave divergence and zero inner scale, followed the Rytov-Tatarski-Fried predictions in the Rytov regime, but departed from the theory in the saturation regime. Increasing inner scale size modified this finite beam behavior by raising the coherence length (up to ~50%) in the saturation regime.					
14. SUBJECT TERMS Coherence length, irradiance variance, inner scale, wave optics propagation, phase screens, atmospheric turbulence				15. NUMBER OF PAGES 185	
				16. PRICE CODE	
17. SECURITY CLASSIFICATION OF REPORT UNCLASSIFIED	18. SECURITY CLASSIFICATION OF THIS PAGE UNCLASSIFIED	19. SECURITY CLASSIFICATION OF ABSTRACT UNCLASSIFIED	20. LIMITATION OF ABSTRACT		

Approved for public release; distribution is unlimited.

Computer Simulation of Wave Propagation Through Turbulent Media

by

Charles A. Davis
Lieutenant, United States Navy
B.S., Duke University, 1983
M.S., Naval Postgraduate School, 1991

Submitted in partial fulfillment of the
requirements for the degree of

DOCTOR OF PHILOSOPHY IN PHYSICS

from the

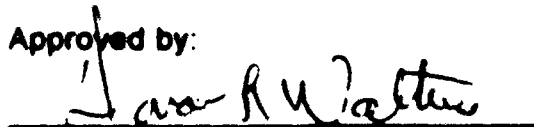
NAVAL POSTGRADUATE SCHOOL
June 1994

Author:



Charles A. Davis

Approved by:



D. L. Walters

Associate Professor of Physics
Dissertation Supervisor



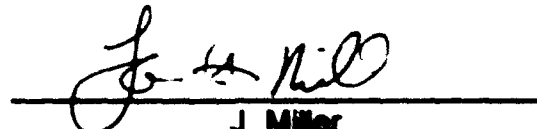
K. E. Woehler

Professor of Physics



D. S. Davis

Associate Professor of Physics



J. Miller


Associate Professor of Electrical
and Computer Engineering



J. N. Eagle

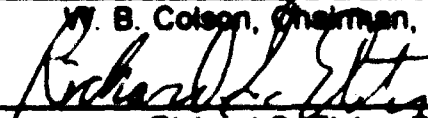
Professor of Operations Research

Approved by:



W. B. Colson, Chairman, Department of Physics

Approved by:



Richard S. Elster, Dean of Instruction

ABSTRACT

This research used Huygens-Fresnel wave optics computer simulations to investigate the effects of high turbulence strength and inner scale on the normalized irradiance variance and coherence length of electromagnetic waves propagating through a turbulent atmosphere. These investigations developed several guidelines for validity of propagation simulations employing a numerical, split-step, Huygens-Fresnel method, and within these guidelines, considered five types of turbulence spectrum inner scale: (1) zero inner scale, (2) Gaussian inner scale, (3) Hill's and (4) Frehlich's viscous-convective enhancement inner scales, and (5) turbulence spectrum truncation from the discrete grid representation. The simulation results showed that the normalized irradiance variance generally decreased (~30%) below the zero inner scale values in the Rytov regime with increasing inner scale size, but increased monotonically in the saturation regime, and agreed within 2% of the Rytov-Tatarski predictions at low turbulence strengths. The E-field coherence length in a spatially confined beam, with either spherical or plane wave divergence and zero inner scale, followed the Rytov-Tatarski-Fried predictions in the Rytov regime, but departed from the theory in the saturation regime. Increasing inner scale size modified this finite beam behavior by raising the coherence length (up to ~50%) in the saturation regime.

Accession For	
NTIS CRA&I	<input checked="" type="checkbox"/>
DTIC TAB	<input type="checkbox"/>
Unannounced	<input type="checkbox"/>
Justification _____	
By _____	
Distribution /	
Availability Codes	
Dist A-1	Avail and/or Special

TABLE OF CONTENTS

I. INTRODUCTION	1
II. BACKGROUND	5
A. CHAPTER OVERVIEW	5
B. WAVE PROPAGATION	5
C. EFFECTS OF TURBULENCE ON THE PROPAGATED WAVE .	13
1. Irradiance Variance and Inner Scale	13
2. Atmospheric MTF and Coherence Length	27
III. COMPUTER SIMULATION	34
A. PROPAGATION CODE	34
B. PHYSICAL PARAMETERS	38
C. COMPUTATION GRID	39
D. SOURCES	47
E. MAXIMUM TURBULENCE STRENGTH	61
F. ADDITIONAL SIMULATION PARAMETERS	95

G. PHASE SCREENS	108
1. Phase Screen Generation	108
2. Low Spatial Frequency Correction	111
H. COHERENCE LENGTH	122
IV. RESULTS	137
A. NORMALIZED IRRADIANCE VARIANCE	137
B. COHERENCE LENGTH	147
V. CONCLUSIONS	169
APPENDIX	173
LIST OF REFERENCES	175
INITIAL DISTRIBUTION LIST	177

ACKNOWLEDGEMENT

I would like to thank Dr. Donald Walters for his continuous guidance and support throughout these investigations and the members of my Ph.D. committee for their time and encouragement. Thanks also to Dr. David Fried for his guidance and valuable discussions and to Brent Ellerbroek and Greg Cochrane of the United States Air Force Phillips Laboratory for their assistance with the computer code. This work received support from Russell Butts and Darrell Spreen of the United States Air Force Phillips Laboratory.

I. INTRODUCTION

Turbulence in a stratified fluid causes random inhomogeneities in temperature and the index of refraction that scatter and diffract a wave propagating through such a medium. Analytical perturbation techniques developed over the past three decades cannot account for the variations observed experimentally in the amplitude and phase distributions of a propagating wave when turbulence levels are high and/or propagation paths are long. Over the past fifteen years, numerical wave optics codes based on the Huygens-Fresnel principle have been developed to address these situations. This research extended these codes to include inner scale in the spectrum of refractive index fluctuations and to examine the coherence length and the effects of inner scale in the Rytov regime (low turbulence strengths and/or short propagation paths) and in the saturation regime (high turbulence strengths and/or long propagation paths).

As a first step, extensive analysis and testing developed guidelines for validity of computer simulations employing Huygens-Fresnel propagation over multiple steps (split-step method). These guidelines include.

- For an NxN grid and propagation distance L, the grid element size should be $\Delta x = \sqrt{\lambda L / N}$.
- The maximum turbulence strengths C_n^2 and propagation distances L for spherical wave propagation with an NxN grid should satisfy $\beta_0^2 \leq 0.1 N^{0.9}$, where $\beta_0^2 = 0.497 C_n^2 k^{7/6} L^{11/6}$.
- Equivalently, the E-field coherence length r_0 should satisfy $r_0 \geq 2.5 \Delta x$, where r_0 represents Fried's coherence length (for spherical waves).
- Use ≥ 30 phase screens/steps for each propagation.
- Use ≥ 30 propagation realizations to get representative statistics.
- Phase screens require low spatial frequency correction to gain 5% accuracy in normalized irradiance variance and as much as 30% in coherence length.
- Half width at half maximum of the atmospheric MTF and an iterative fit r_0 provide the most stable parameterizations of the E-field coherence length.
- Telltale signs of aliasing include a fine-grained irradiance pattern, a boxed perimeter to the irradiance pattern, and peaking of the energy toward the center of the computation grid.

These investigations also examined four choices of E-field source function and refined the methods of normalized irradiance variance and E-field coherence length calculation

These simulations incorporated five types of turbulence spectrum inner scale: (1) zero inner scale, (2) Gaussian inner scale, (3) Hill's and (4) Frehlich's viscous-convective enhancement inner scales, and (5) turbulence spectrum

truncation from the discrete grid representation. For the more physically realistic viscous-convective enhancement inner scale, the computer simulations provided the following results:

- The Hill and Frehlich parameterizations performed almost identically, giving less than 3% difference in normalized irradiance variance over the Rytov and saturation regimes.
- In the Rytov regime, the normalized irradiance variance for an approximately spherically diverging beam increased (~30%) and then decreased (~30%) compared to the zero inner scale values as the inner scale size increased, and the E-field coherence length r_0 decreased slightly (~5%) compared to the zero inner scale coherence length.
- In the saturation regime, increasing inner scale size gave monotonically increasing normalized irradiance variance and increased the coherence length (up to ~50%) compared to the zero inner scale case.

The effect of the Gaussian inner scale on normalized irradiance variance and coherence length was also investigated.

These investigations examined the behavior of the E-field coherence length for E-fields (beams) that were constrained in lateral extent to the grid size but whose divergence approximated that of spherical waves, plane waves, and intermediate beam waves. The computer simulations showed that:

- For the Rytov regime, the spherical and plane wave cases gave coherence lengths within 5% of the Rytov-Tatarski-Fried predictions.
- In the saturation regime, the E-field coherence lengths for the spherical wave approximation decreased ~25% below the theory, while the coherence lengths for the plane wave approximation varied within -5%/+15% of the theory.

- The E-field coherence lengths for the beam wave cases were spaced between the spherical and plane wave values for the Rytov regime, but increased toward the spherical wave values in the saturation regime.

The spatially confined beams used in these simulations showed a departure in behavior of the E-field coherence length in the saturation regime from the predictions of first order perturbation theory.

The organization of this dissertation generally follows the preceding summary of major points. **Chapter II** summarizes the theory of wave optics and the implementation of the Huygens-Fresnel propagation in a computer simulation. It then provides an overview of the Rytov-Tatarski theory for the effect of atmospheric turbulence, including inner scale, on the normalized irradiance variance and E-field coherence length as applied to spherical wave propagation. **Chapter III** discusses the detailed choices of physical and simulation parameters and develops the guidelines to ensure validity of the simulation. **Chapter IV** presents the computer simulation results, first for the inner scale effects on normalized irradiance variance, then for the behavior of the E-field coherence length in the Rytov and saturation regimes, and for the effect of inner scale on coherence length.

II. BACKGROUND

A. CHAPTER OVERVIEW

This chapter summarizes first the theory of electromagnetic wave propagation and the Huygens-Fresnel solution to the scalar wave equation and recasts the Huygens-Fresnel solution into a form utilizing fast Fourier transforms easily implemented in a computer simulation. It then summarizes the Rytov-Tatarski solution to the scalar wave equation which used first order perturbation theory and statistical techniques to describe the spatial variations of the irradiance of an electromagnetic wave propagated through a turbulent medium. The Kolmogorov spectrum of refractive index fluctuations is introduced as well as five types of inner scale which modify the high spatial frequency portion of this spectrum. The chapter concludes by describing Fried's method for parameterizing the coherence length of the E-field for a spherically-diverging wave propagating through a turbulent medium.

B. WAVE PROPAGATION

Maxwell's equations describe of the propagation of electromagnetic waves through a turbulent medium. Assuming a locally homogeneous, isotropic, and linear medium,

$$\nabla \cdot \epsilon \hat{E} = \rho, \quad (1)$$

$$\nabla \cdot \hat{B} = 0, \quad (2)$$

$$\nabla \times \hat{E} = -\frac{\partial \hat{B}}{\partial t}, \quad (3)$$

$$\nabla \times \hat{H} = \sigma \hat{E} + \frac{\partial (\epsilon \hat{E})}{\partial t}, \quad (4)$$

where hatted (^) quantities represent vectors. At the frequencies and field strengths of interest, the medium may be assumed to have zero local free charge density ρ and zero (or negligible) conductivity σ . Laser beams in the atmosphere satisfy these conditions. Expanding the left-hand side of Eq. (1) and combining the curl of Eq. (3) and the time derivative of Eq. (4) gives a vector wave equation for the E-field

$$\nabla^2 \hat{E} + \nabla(\hat{E} \cdot \nabla \ln \epsilon) - \mu \epsilon \frac{\partial^2 \hat{E}}{\partial t^2} = 0. \quad (5)$$

The middle term represents depolarization of the E field and is negligibly small for propagation through a turbulent atmosphere (Tatarski, 1961; Lawrence and Strohbehn, 1970). Neglecting the middle term simplifies the vector wave equation to

$$\nabla^2 \hat{E} - \mu \epsilon \frac{\partial^2 \hat{E}}{\partial t^2} = 0. \quad (6)$$

The Fresnel-Kirchoff diffraction theory provides an approximate scalar solution to this vector wave equation. Following Hecht (1987), the spherical wave solution is

$$E(\xi, t) = \frac{E_0}{\xi} e^{ik\xi - i\omega t}, \quad (7)$$

where E_0 is a constant and $k = 2\pi/\lambda$. Using Eq. (7) with the time dependence factored out, the Kirchoff integral theorem becomes

$$E_P = \frac{1}{4\pi} \left[\iint_S \frac{e^{ik\eta}}{\eta} \nabla E(\xi) \cdot d\mathbf{S} - \iint_S E(\xi) \nabla \left(\frac{e^{ik\eta}}{\eta} \right) \cdot d\mathbf{S} \right], \quad (8)$$

which must be evaluated over a surface S enclosing the field point P . Figure (1) illustrates the relationship between the distances ξ and η . If the wavelength $\lambda \ll \xi, \eta$, Eq. (8) reduces to the Fresnel-Kirchoff diffraction formula

$$E_P = -\frac{E_0}{\lambda} \iint_S \frac{e^{ik(\xi+\eta)}}{\xi \eta} K(\theta) dS, \quad (9)$$

where $K(\theta)$ represents the obliquity factor.

Integrating Eq. (9) over the half sphere S (shown in Fig. (1)) as the radius approaches infinity, the electric field amplitude is appreciable only over a finite aperture area A of the hemisphere's flat side. Then Eq. (9) reduces to the more familiar Huygens-Fresnel expression

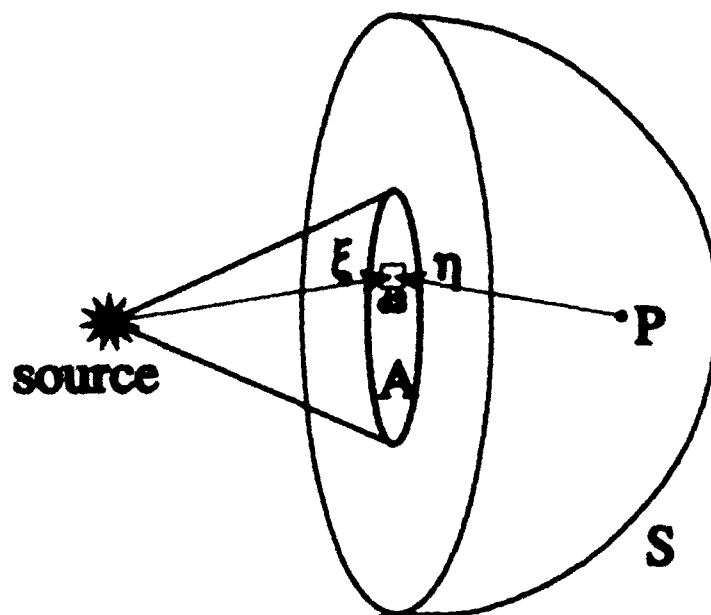


Figure 1 Fresnel-Kirchhoff diffraction geometry showing relationship between source, aperture A, surface S, and field point P.

$$E_P = \frac{-i}{\lambda} \iint_A E_A \frac{e^{ik\eta}}{\eta} K(\theta) dA \quad (10)$$

The complex aperture function E_A contains the source spherical wave factor, $\exp(ik\xi)/\xi$. The E-field at a point P is a function of the E-field over a finite aperture A.

The Huygens-Fresnel formulation , Eq. (10), serves as the basis for calculating the propagation of a wave through turbulence. This formula can now be cast into a form easily implemented in a propagation computer simulation. Applying the Cartesian coordinate system of Fig. (2), the Huygens-Fresnel principle becomes,

$$E(\mathbf{r}, z) = \frac{-i}{\lambda} \iint_A E(\hat{\mathbf{p}}, 0) \frac{e^{ik\sqrt{z^2 + |\mathbf{r} - \hat{\mathbf{p}}|^2}}}{\sqrt{z^2 + |\mathbf{r} - \hat{\mathbf{p}}|^2}} K(\theta) dA. \quad (11)$$

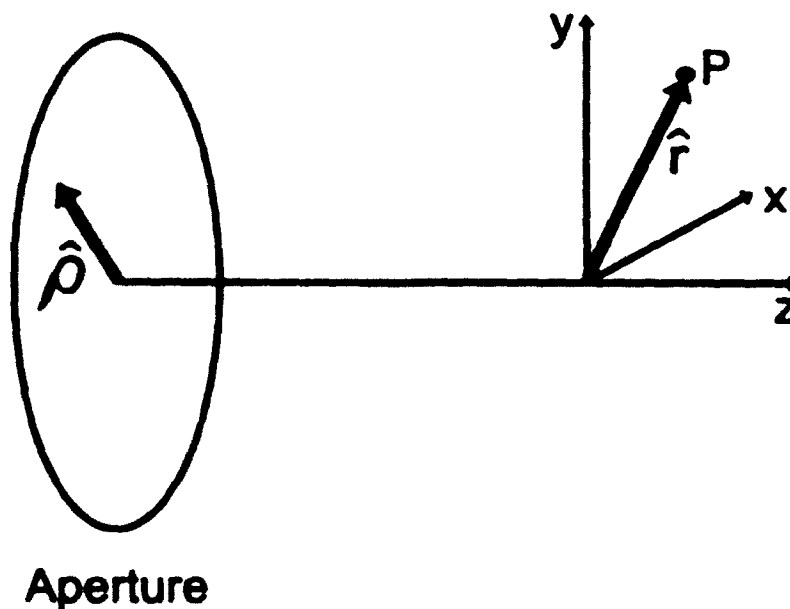


Figure 2 Propagation coordinate system showing relations between the aperture variables and the field variables.

\vec{r} represents the position vector of the observation point P in the x-y plane and

\hat{p} represents the position vector of the radiating point in the aperture plane.

The paraxial approximation assumes that

$$|\vec{r}| < z \quad \text{and} \quad |\hat{p}| < z, \quad (12)$$

where z measures the longitudinal distance of the point P from the aperture.

Consequently, the obliquity factor $K(\theta) = (1 + \cos\theta)/2$ becomes approximately 1

and the denominator of the integrand is approximately z (Jodman, 1968),

$$E(\vec{r}, z) = \frac{-j}{\lambda z} \iint_A E(\hat{p}, 0) e^{jk\sqrt{z^2 + |\vec{r} - \hat{p}|^2}} dA \quad (13)$$

Following Roberts (1966), the Fresnel approximation assumes that the lateral

displacement between the radiating point and the observation point

$|\vec{r} - \hat{p}| \ll z$. Then, using the lowest order terms for the series expansion

of the complex exponential's argument, Eq. (13) becomes

$$\begin{aligned} E(\vec{r}, z) &= \frac{-j}{\lambda z} \iint d\hat{p} E(\hat{p}, 0) e^{-\frac{jkz}{1} \sqrt{1 - \frac{|\vec{r} - \hat{p}|^2}{z^2}}} \\ &= \frac{-j}{\lambda z} \iint d\hat{p} E(\hat{p}, 0) e^{-\frac{jkz}{1} (1 - \frac{1}{2} \frac{|\vec{r} - \hat{p}|^2}{z^2})} \\ &= \frac{-j}{\lambda z} e^{-\frac{jkz}{1}} \iint d\hat{p} E(\hat{p}, 0) e^{\frac{jk}{2z} |\vec{r} - \hat{p}|^2}. \end{aligned} \quad (14)$$

The factor $\exp(-2\pi iz/\lambda)$ represents the change in phase of the optical wave from the center of the aperture plane to the plane of the observation point P. It applies to the whole E-field and depends only on the propagation distance z. It does not affect the phase variation across the E-field nor the amplitude of the E-field, and will be dropped in the following expressions for simplicity.

Equation (14) can be recast into a form utilizing Fourier transforms. Expanding the aperture field $E(\hat{\rho}, 0)$ in Eq. (14) using the Fourier transform identity

$$E(\hat{\rho}, 0) = \int d\hat{\rho}' e^{2\pi i \hat{\rho} \cdot \hat{\rho}'} \int d\hat{\rho}'' e^{-2\pi i \hat{\rho}'' \cdot \hat{\rho}'} E(\hat{\rho}'', 0), \quad (15)$$

Eq. (14) becomes

$$E(\hat{\rho}, z) = -\frac{i}{\lambda z} \int d\hat{\rho} \left[\int d\hat{\rho}'' e^{2\pi i \hat{\rho} \cdot \hat{\rho}''} \int d\hat{\rho}' e^{-2\pi i \hat{\rho}' \cdot \hat{\rho}''} E(\hat{\rho}'', 0) \right] e^{\frac{i\pi}{\lambda z} |\hat{\rho} - \hat{\rho}'|^2}. \quad (16)$$

(Note: these equations use spatial frequency $\hat{\rho}$ (m^{-1}) instead of spatial wavenumber $\hat{k} = 2\pi \hat{\rho}$ (rad/m) because the discrete Fourier transform computer subroutines used in these investigations are written with spatial frequency $\hat{\rho}$.) Making the change of variables $\hat{\rho}' = \hat{\rho} - \hat{\rho}''$ gives

$$\begin{aligned}
 E(\vec{r}, z) = & -\frac{i}{\lambda z} \int (-d\vec{r}') \left[\int d\vec{\rho} e^{i\vec{r} \cdot \vec{\rho}} \int d\vec{\rho}' e^{-i\vec{r}' \cdot \vec{\rho}'} E(\vec{\rho}', 0) \right] e^{\frac{ik}{2z} |\vec{r}'|^2}, \\
 & - \frac{i}{\lambda z} \int d\vec{\rho} e^{i\vec{r} \cdot \vec{\rho}} \int d\vec{\rho}' e^{-i\vec{r}' \cdot \vec{\rho}'} E(\vec{\rho}', 0) \left[\int d\vec{r}' e^{-i\vec{r}' \cdot \vec{\rho}'} e^{\frac{ik}{2z} |\vec{r}'|^2} \right].
 \end{aligned}
 \tag{17}$$

The last integration over $d\vec{r}'$ is the Fourier transform of a Gaussian function,

$$\int d\vec{r}' e^{-i\vec{r}' \cdot \vec{\rho}'} e^{\frac{ik}{2z} |\vec{r}'|^2} = i\lambda z e^{-ik\lambda z |\vec{\rho}'|^2}.
 \tag{18}$$

Substituting $\vec{\rho}$ for $\vec{\rho}'$, the E-field of Eq. (17) becomes

$$E(\vec{r}, z) = \int d\vec{\rho} e^{i\vec{r} \cdot \vec{\rho}} e^{-ik\lambda z |\vec{\rho}|^2} \int d\vec{\rho}' E(\vec{\rho}', 0) e^{-i\vec{r}' \cdot \vec{\rho}}.
 \tag{19}$$

Equation (19) may be symbolically written as

$$E(\vec{r}, z) = \text{IFT} [e^{-ik\lambda z |\vec{\rho}|^2} \text{FT}[E(\vec{\rho}, 0)]].
 \tag{20}$$

where FT and IFT represent the two-dimensional Fourier transform and inverse Fourier transform, respectively. Equation (20) expresses the E-field at a propagation distance z in terms of Fourier transforms of the E-field at $z = 0$ represented in a Cartesian coordinate system. This form of the Huygens-Fresnel principle is useful for a simulation that subdivides the propagation path into a sequence of short Fresnel propagation steps.

C. EFFECTS OF TURBULENCE ON THE PROPAGATED WAVE

1. Irradiance Variance and Inner Scale

The next step in modeling the propagation of an E-field through a turbulent medium requires a statistical characterization of the turbulence and its effect on the spatial statistics of the propagating wave. To begin understanding the effect of turbulence upon the wave, consider a spherical wave incident upon a medium with randomly varying index of refraction, as shown in Fig. (3). For small variations in the index of refraction about the mean value, scattering occurs predominantly in the forward direction (Tatarski, 1961). The regions of index of refraction fluctuation accelerate/retard portions of the wavefront over short propagation distances and cause variations in phase across the reference spherical wavefront. Subsequent diffraction and interference then create variations in irradiance across the wavefront. Compared to propagation through zero turbulence (Fig. (4)), a spherically diverging beam now exhibits significant variations in phase and amplitude (irradiance) (Fig. (5)).

A statistical description of the refractive index fluctuations is needed to calculate the E-field variations. The index of refraction, n , in air depends upon the temperature T and pressure P (Tatarski, 1961). At visible wavelengths,

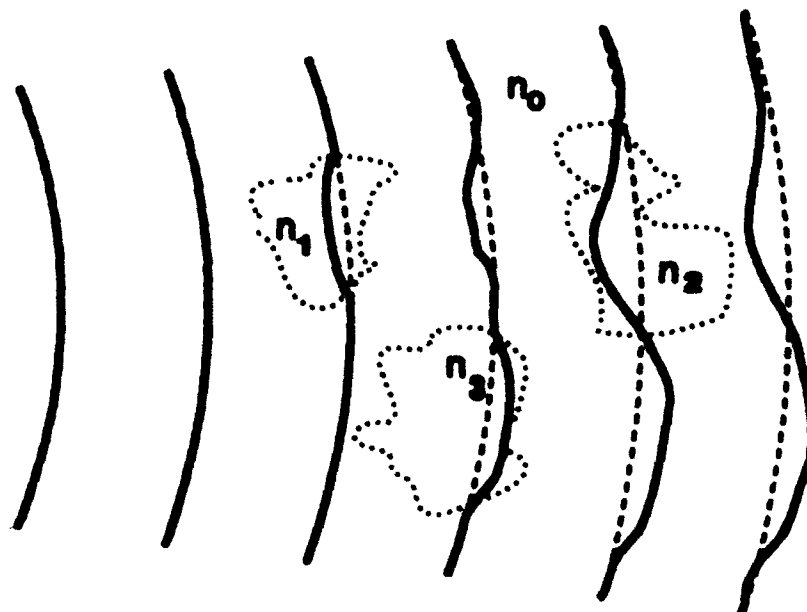


Figure 3 Wave propagating through a medium having random inhomogeneities in index of refraction.

$$n - 1 = 79 \times 10^{-6} \frac{P \text{ (millibars)}}{T \text{ (K)}}. \quad (21)$$

The temperature profile in the atmosphere possesses significant stratification, as shown in Fig. (6) (Walters, 1994). Velocity shear between different layers in the atmosphere causes turbulence which disrupts the interface between these layers, mixing regions of different temperatures. The velocity fluctuations generated by the turbulence at the interface between layers generally follow the Kolmogorov spectrum,

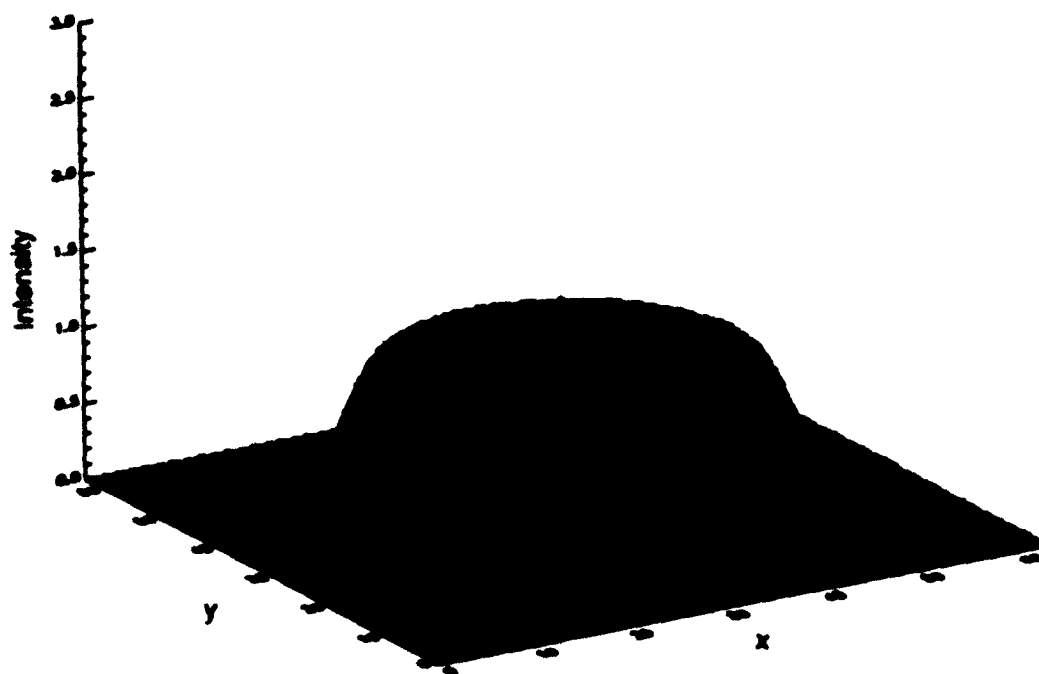


Figure 4 Irradiance plot for a spherically diverging beam propagated through zero turbulence.

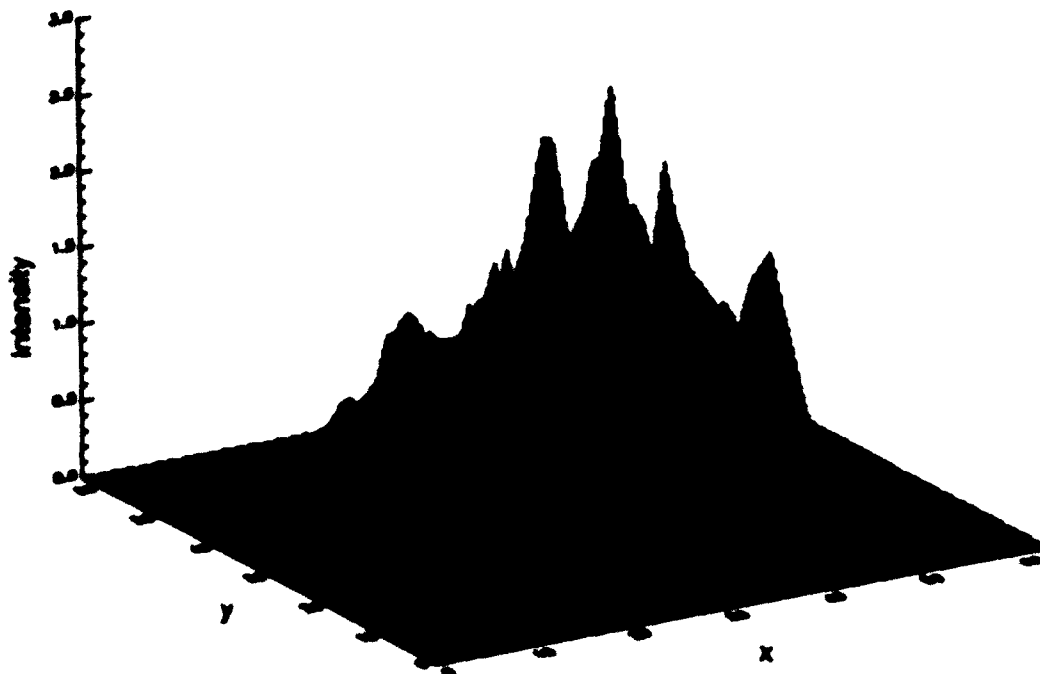


Figure 6 Irradiance plot for spherically diverging beam propagated through turbulence.

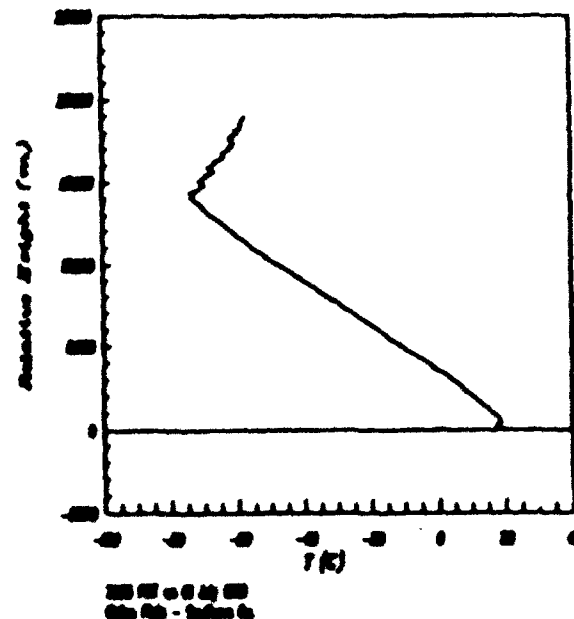


Figure 6 Vertical profile of temperature in the atmosphere.

$$\Phi(\kappa) = \kappa^{-11/3}, \quad (22)$$

assuming isotropic and homogeneous turbulence. κ represents spatial wavenumber in rad/m. Temperature is a "passive additive" (Tatarski, 1961) in the atmosphere, meaning that it does not affect the dynamics of the turbulence. Thus, the three-dimensional spectrum of temperature fluctuations also follows the Kolmogorov spectrum. Since Eq. (21) relates the index of refraction to temperature, the spectrum of refractive index fluctuations is also Kolmogorov (Tatarski, 1961)

$$\Phi_n(\kappa, z) = 0.033 C_n^2(z) \kappa^{-11/3}, \quad (23)$$

where $C_n^2(z)$ is a constant of proportionality indicating the strength of the turbulence. In reality, this spectrum only applies to an intermediate range of wavenumbers known as the inertial subrange, shown in Fig. (7). The boundaries at the high and low spatial wavenumbers are the inner and outer scales, respectively, and are discussed below.

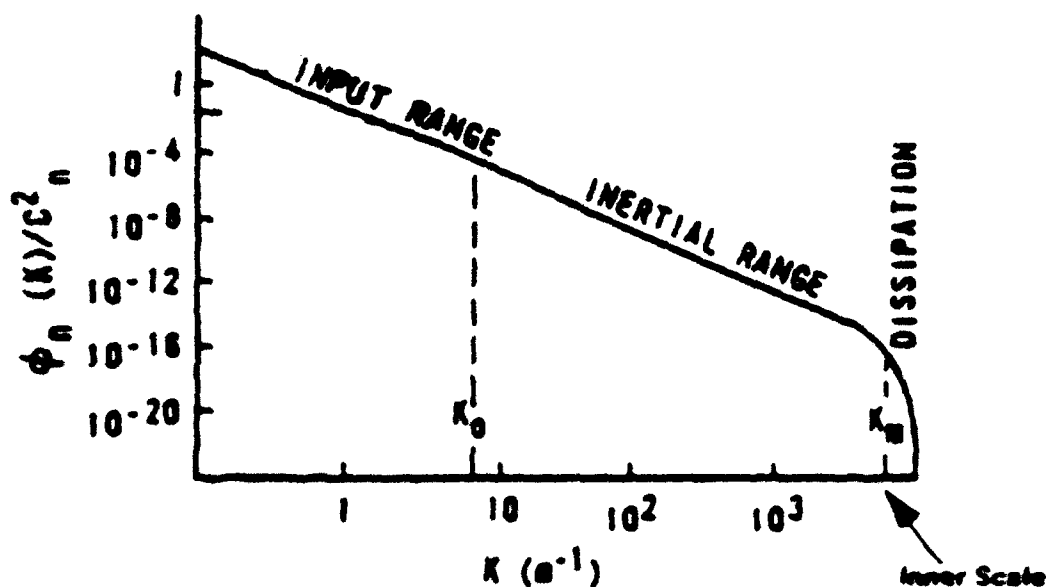


Figure 7 Atmospheric spectrum of refractive index fluctuations showing inertial subrange and outer and inner scales.

With this understanding of the effect of turbulence on a propagating E-field, Tatarski (1961) derived expressions for the statistical properties of the amplitude, phase, and irradiance of a spherical wave propagating through a turbulent medium as follows. Consider a scalar component of the vector wave equation Eq. (6) and assume a harmonic time

dependence for the E-field

$$E(\mathbf{r}, t) = u(\mathbf{r}) e^{i\omega t}. \quad (24)$$

Perform the time derivatives and introduce the wavenumber $k = 2\pi/\lambda$ and the index of refraction

$$n = c \sqrt{\mu \epsilon} \quad (25)$$

(where c = velocity of light in vacuum, μ = magnetic permeability of the medium, ϵ = electric permittivity of the medium) to get the scalar wave equation

$$\nabla^2 u + k^2 n^2(\mathbf{r}) u = 0. \quad (26)$$

Expressing the index of refraction as

$$n(\mathbf{r}) = 1 + n_1(\mathbf{r}), \quad (27)$$

where $|n_1(\mathbf{r})| \ll 1$, and using the Rytov method of smooth perturbations that employs $u = \exp(\Psi)$, $\Psi = \Psi_0 + \Psi_1 + \dots$, and $u = u_0 + u_1 + \dots$, the wave equation becomes

$$\nabla^2 \Psi_1 + 2 \nabla \Psi_0 \cdot \nabla \Psi_1 + 2 k^2 n_1(\mathbf{r}) u_0 = 0. \quad (28)$$

This has a solution

$$\Psi_1(\mathbf{r}) = \frac{k^2}{2\pi u_0(\mathbf{r})} \int_V n_1(\mathbf{r}') u_0(\mathbf{r}') \frac{\exp(i k |\mathbf{r} - \mathbf{r}'|)}{|\mathbf{r} - \mathbf{r}'|} dV'. \quad (29)$$

For a spherical wave

$$u_0(|r|) = \frac{Q \exp(ik|r|)}{|r|}, \quad (Q = \text{constant}) \quad (30)$$

and for small wavelengths $\lambda \ll \ell_0$, where ℓ_0 (the inner scale) characterizes the size of the smallest fluctuations in the index of refraction, the Fresnel approximation in Cartesian coordinates reduces Eq. (29) to

$$\Psi_1(r) = \frac{k^2 z}{2\pi} \int_V n_1(r') \frac{\exp(ik \frac{z^2(x'^2 + y'^2) + z'^2(x^2 + y^2) - 2zx'(xx' + yy')}{2zz'(z-z')})}{z'(z-z')} dV'. \quad (31)$$

The statistics of the turbulence appear in Ψ_1 and n_1 in terms of spectral expansions where n_1 contains the three-dimensional spatial frequency spectrum of refractive index fluctuations, $\Phi_n(\kappa)$. The Rytov approximation introduces the log amplitude fluctuation X

$$X = \ln \frac{A}{A_0}, \quad (32)$$

where A and A_0 are the amplitudes of the turbulence perturbed E-field u and the free space E-field u_0

$$\begin{aligned} u &= A e^{iS} \\ u_0 &= A_0 e^{iS_0}. \end{aligned} \quad (33)$$

Then, after an extended series of manipulations (see Tatarski, 1961) that assume local homogeneity and isotropy, the variance of the log amplitude

fluctuation X of a spherical wave propagating over a distance L becomes

$$\overline{X^2} = 4\pi^2 k^2 \int_0^\infty dx \kappa \int_0^L dz \Phi_n(\kappa, z) \sin^2 \left[\frac{\kappa^2 z (L - z)}{2 k L} \right]. \quad (34)$$

where $k = 2\pi/\lambda$, and κ = spatial wavenumber (rad/m), which is used here instead of spatial frequency f (1/m) to be consistent with previous work.

Assuming that the irradiance follows a log normal distribution (Tatarski, 1961), the normalized irradiance variance is a function of the log amplitude variance

$$\frac{\sigma_I^2}{\bar{I}^2} = \exp(4 \overline{X^2}) - 1. \quad (35)$$

The assumption of isotropic, homogeneous turbulence gives a Kolmogorov spectrum of refractive index fluctuations of the form $\Phi_n(\kappa, z) = 0.033 C_n^2(z) \kappa^{-11/3}$ (Tatarski, 1961). Assuming, for computational convenience, that this $\kappa^{-11/3}$ power law dependence holds over the entire range of spatial wavenumbers κ , and that the turbulence strength $C_n^2(z)$ is uniform along the path, then integration of Eq. (34) gives the log amplitude variance for a spherical wave as

$$\overline{X^2} = 0.124 C_n^2 k^{7/3} L^{11/3}. \quad (36)$$

The normalized irradiance variance of Eq. (35) becomes

$$\frac{\sigma_I^2}{\gamma^2} = \exp(4 \overline{X^2}) - 1 = \exp(0.497 C_n^2 k^{7/6} L^{11/6}) - 1. \quad (37)$$

Low turbulence (small C_n^2) and/or short path lengths make the exponent small enough to apply the approximation $\exp(\alpha) \approx 1+\alpha$, giving

$$\frac{\sigma_I^2}{\gamma^2} = 0.497 C_n^2 k^{7/6} L^{11/6} = \beta_o^2, \quad (38)$$

where the new parameter β_o^2 , defined by this equation, serves as the baseline normalized irradiance variance for comparing modifications to the spectrum of refractive index fluctuations. β_o^2 also facilitates plotting normalized irradiance variance over a broad range of integrated turbulence strengths.

The above steps characterize the effects of the turbulent medium upon the irradiance statistics of a spherical wave assuming a simple Kolmogorov spectrum of refractive index fluctuations. Incorporating a high spatial frequency rolloff at the inner scale, as shown in Fig. (7), modifies the irradiance statistics. The inner scale ℓ_0 represents the physical size where viscosity of the medium smooths the velocity fluctuations by dissipating kinetic energy and thermal diffusion smooths the temperature fluctuations (thus refractive index fluctuations), removing the turbulent character of the medium at this scale. This smoothing causes a rolloff of the high spatial frequency energy

of the refractive index spectrum. Flatté, Wang, and Martin (1993) write the three-dimensional isotropic spectrum as

$$\Phi(\kappa, z) = 0.033 C_n^2(z) \kappa^{-11/3} F(\kappa \ell_0), \quad (39)$$

where $F(\kappa \ell_0)$ represents a particular functional form of the inner scale. The parameter $\kappa \ell_0$ consists of the spatial wavenumber κ (radians / meter) and the inner scale parameter ℓ_0 (meters). For zero inner scale (i.e. no high spatial frequency rolloff),

$$F(\kappa \ell_0) = 1, \quad 0 < \kappa < \infty. \quad (40)$$

For theoretical and computational convenience, a Gaussian rolloff inner scale is often used (Tatarski, 1961) to represent the high spatial frequency rolloff from viscosity

$$F(\kappa \ell_0) = \exp\left(-\left(\frac{\kappa \ell_0}{5.9}\right)^2\right). \quad (41)$$

The more realistic viscous-convective enhancement inner scale advocated by Hill (1978) and Frehlich (1992) exhibits an enhanced spectrum for the wavenumbers slightly less than the rolloff point. Viscosity attenuates the kinetic energy and lowers the velocity fluctuations over regions near the inner scale size and smaller before thermal diffusion can smooth all the temperature fluctuations within these regions. This disparity alters the temperature and

corresponding index of refraction spectra. Inner-scale-sized patches of air have different temperatures but have little internal velocity variation. Since the Kolmogorov spectrum is based upon the spectrum of velocity fluctuations, these residual temperature fluctuations cause an enhancement to the Kolmogorov spectrum around the inner scale size. At higher spatial frequencies beyond the inner scale, thermal diffusion does smooth out these residual temperature fluctuations and the spectrum falls off sharply.

Hill provides a plot of $F(\kappa \ell_0)$ versus $\kappa \ell_0$ for the viscous-convective enhancement, that is suitable for implementing the viscous-convective enhancement inner scale for numerical integrations and computer simulations (Flatté, Wang, and Martin, 1993). Frehlich presents a similar characterization of the viscous-convective enhancement inner scale based upon laser scintillation measurements and provides a four parameter fit to describe this version of the viscous-convective enhancement inner scale.

Since most numerical simulations, such as the one used here, utilize discrete Fourier transforms, the spatial frequency grid mesh chosen for calculations introduces a maximum spatial frequency κ_{\max} established by the Nyquist sampling criterion (discussed in Chapter III). This limit creates a grid cutoff inner scale at κ_{\max} .

$$F(\kappa \ell_0) = \begin{cases} 1, & 0 < \kappa < \kappa_{\max} \\ 0, & \kappa > \kappa_{\max} \end{cases} \quad (42)$$

Figure (8) illustrates these five inner scales for eight inner scale sizes. Solid curves represent the Hill version of the viscous-convective inner scale, dashed curves represent the Frehlich version of the viscous-convective inner scale, and dotted curves represent Gaussian inner scales. The solid line with the box shape represents the numerical grid cutoff inner scale at $\kappa_{\max} = 318 \text{ rad/m}$ for a 1024×1024 mesh. The inner scale values of 2, 3, 4, 5, 6, 7, 10, and 15 cm refer to stratospheric propagation over 200 km, assuming an optical wavelength of 500 nm.

The outer scale L_0 , corresponding to the spatial wavenumber $\kappa_m = 2\pi/L_0$, represents the upper size limit to which the Kolmogorov spectrum applies. For scale sizes larger than L_0 (or spatial wavenumbers less than κ_m), the refractive index fluctuations level off to a finite value as κ approaches zero. Physically, such a limitation exists as the spatial wavenumbers approach zero because the refractive index fluctuations cannot become arbitrarily large, or equivalently, the energy represented by the spectrum must remain finite (Tatarski, 1961). Estimates of the outer scale for the stratosphere lie in the range of tens to hundreds of meters. However, the outer scale proves to be much more problematic to include in the spectrum of refractive index fluctuations because the atmosphere is anisotropic at these large sizes (Tatarski, 1961). The Von Kármán spectrum (Tatarski, 1961),

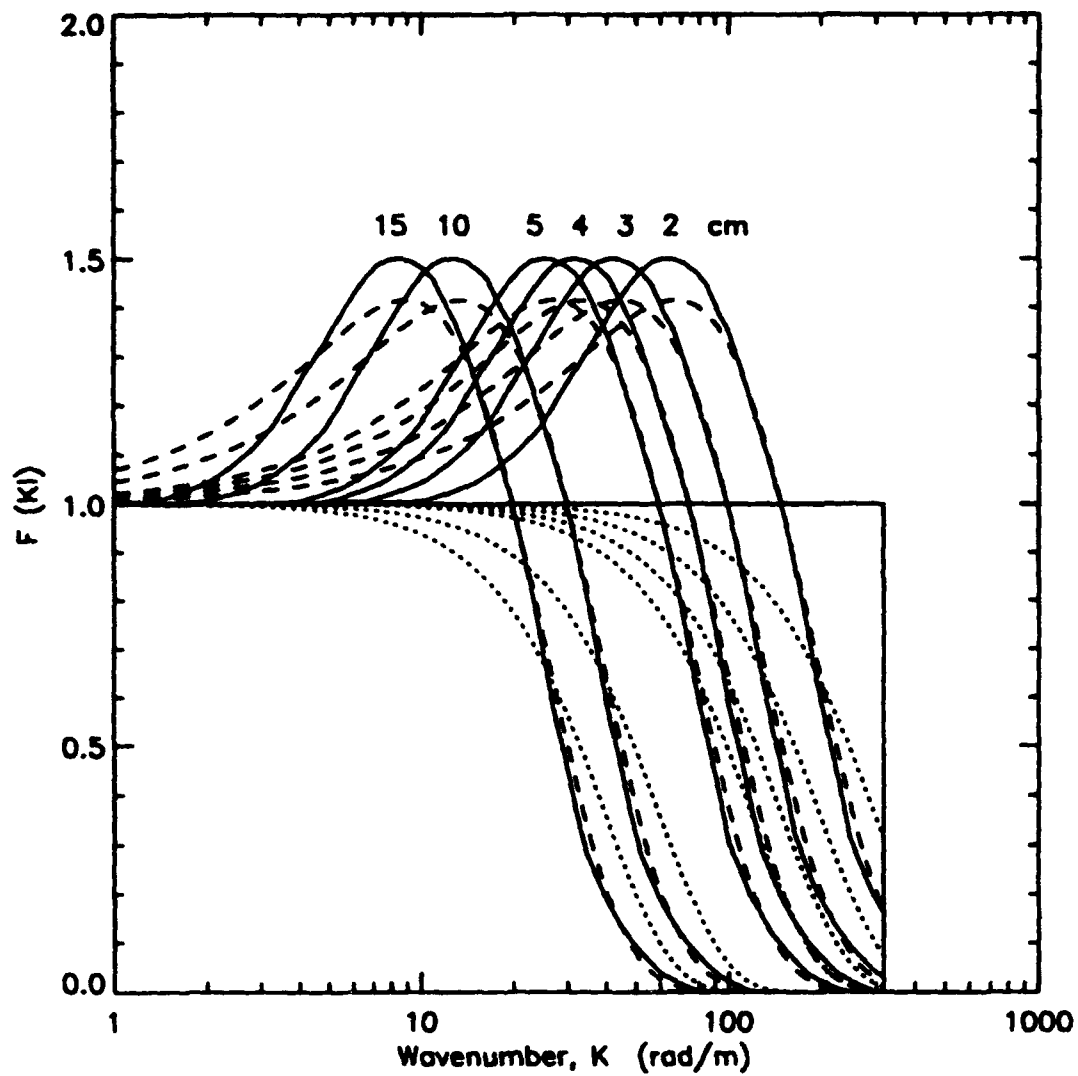


Figure 8 Inner scale function $F(\kappa l_0)$ for the grid cutoff (box), Gaussian (dotted), Hill (solid), and Frehlich (dashed) inner scales, plotted for 1024x1024 grid, $L = 200$ km, and $\lambda = 500$ nm.

$$\Phi_n(\kappa) = \frac{0.033 C_n^2}{(\kappa^2 + \kappa_0^2)^{-11/6}} e^{-\left(\frac{\kappa}{\kappa_m}\right)^2}. \quad (43)$$

which has been used to incorporate an outer scale for some calculations, is based upon computational convenience more than physical understanding. Additionally the computer simulation results were compared against the Rytov-Tatarski predictions, which were derived without an outer scale. Therefore, these investigations did not incorporate an outer scale.

2. Atmospheric MTF and Coherence Length

Propagation through a turbulent medium not only affects the irradiance statistics, but also reduces the spatial coherence of the wave as characterized by the transverse coherence length. Fried (1966, p. 1372-1379) derived a long exposure modulation transfer function (MTF) for a spherical wave propagating through a turbulent atmosphere and used this to parameterize the E-field transverse coherence length, r_0 . Following the method and notation of Fried (which used spatial frequency f in (m^{-1})), consider the spatial Fourier transform of the intensity of an E-field propagated through the turbulent medium and imaged by a thin lens

$$\tau(f) = B \int d\hat{x} u^*(\hat{x}) u(\hat{x}) e^{i2\pi f \cdot \hat{x}}, \quad (44)$$

where $u(\hat{x})$ represents the E-field in the image plane and B represents a

normalization constant. Fried calls this the "MTF of the image-forming optical system", assuming a unit impulse (point) illumination and anticipating the fact that the ensemble average of $\tau(f)$, which incorporates the effects of atmospheric turbulence, turns out to be real. Utilizing the Fourier transform property of a thin lens,

$$u(x) = A \int d\vartheta U(\vartheta) e^{-\frac{2\pi}{\lambda R} x \vartheta}, \quad (45)$$

where A is another normalization constant and $U(\vartheta)$ represents the E-field in the plane of the thin lens aperture, the MTF becomes

$$\tau(f) = A^2 B \int d\vartheta U^*(\vartheta - \lambda R f) U(\vartheta). \quad (46)$$

Expressing the E-field $U(\vartheta)$ as the product of a zero turbulence propagation part, $W(\vartheta)$, and an atmosphere-induced perturbation, $V(\vartheta)$,

$$U(\vartheta) = W(\vartheta) V(\vartheta) = W(\vartheta) e^{i(\eta + \phi(\vartheta))}. \quad (47)$$

$W(\vartheta)$ represents the uniformly illuminated aperture function. $\eta(\vartheta)$ represents fluctuations in the log amplitude of the E-field and $\phi(\vartheta)$ represents phase fluctuations.

Taking the ensemble average $\langle \rangle$ of Eq. (46) over many realizations and substituting in Eq. (47) gives the long exposure MTF

$$\langle \tau(\vec{r}) \rangle_{\text{long exposure}} = A^2 B \int d\vec{\rho} W^*(\vec{\rho} - \lambda R \vec{r}) W(\vec{\rho}) \langle V^*(\vec{\rho} - \lambda R \vec{r}) V(\vec{\rho}) \rangle. \quad (48)$$

Fried denotes the expectation of the fluctuations as the "atmosphere's MTF",

$$MTF_{\text{atmos}}(\vec{r}) = \langle V^*(\vec{\rho} - \lambda R \vec{r}) V(\vec{\rho}) \rangle, \quad (49)$$

and Hufnagel and Stanley (1964) call this the average mutual coherence factor.

Substituting from Eq. (47),

$$\langle V^*(\vec{\rho} - \lambda R \vec{r}) V(\vec{\rho}) \rangle = \langle e^{i[\ell(\vec{\rho}) - \ell(\vec{\rho} - \lambda R \vec{r})]} \cdot e^{i[\phi(\vec{\rho}) - \phi(\vec{\rho} - \lambda R \vec{r})]} \rangle. \quad (50)$$

Using the fact that ϕ and ℓ are Gaussian random variables, Fried shows that the atmosphere's MTF reduces to

$$\langle V^*(\vec{\rho} - \lambda R \vec{r}) V(\vec{\rho}) \rangle = e^{-\frac{1}{2} D(\lambda R |\vec{r}|)}, \quad (51)$$

where $D(\lambda R |\vec{r}|)$ represents the wave structure function and is related to the phase structure function D_ϕ and the log amplitude structure function D_ℓ by

$$D(r) = D_\ell(r) + D_\phi(r), \quad \text{where } r = |\vec{\rho} - \lambda R \vec{r}|. \quad (52)$$

The log amplitude structure function D_ℓ and phase structure function D_ϕ are defined as

$$D_\ell(r) = \langle [\ell(\vec{\rho}) - \ell(\vec{\rho} - \lambda R \vec{r})]^2 \rangle, \quad (53)$$

$$D_\phi(r) = \langle [\phi(\vec{\rho}) - \phi(\vec{\rho} - \lambda R \vec{r})]^2 \rangle,$$

and describe the expected variation in the log amplitude and phase, respectively, at two points a distance λRf apart. Denoting the MTF of the aperture function $W(\vartheta)$ as

$$\tau_o(f) = A^2 B \int d\vartheta W^*(\vartheta - \lambda Rf) W(\vartheta), \quad (54)$$

and using the fact that the atmospheric MTF of Eq. (51) is independent of ϑ , the long exposure MTF of Eq. (48) now becomes

$$\langle \tau(f) \rangle_{\text{long exposure}} = \tau_o(f) e^{-\frac{1}{2} D(\lambda Rf)}, \quad (55)$$

or,

$$e^{-\frac{1}{2} D(\lambda Rf)} = \frac{\langle \tau(f) \rangle_{\text{long exposure}}}{\tau_o(f)}. \quad (56)$$

The long exposure MTF is related to the mutual coherence of the E-field. The mutual coherence function (MCF) describes the autocorrelation between the E-field at two points and is defined as (Goodman, 1985)

$$MCF = \langle U^*(r_1, t_1) U(r_2, t_2) \rangle, \quad (57)$$

where U represents the complex E-field. For these investigations $t_1 = t_2$ and explicit time notation will be dropped. Assuming homogeneity, the MCF becomes the spatial autocorrelation of the E-field

$$MCF(\eta) = \int d\mathbf{r}' U^*(\mathbf{r}') U(\mathbf{r}' + \eta). \quad (58)$$

Taking the ensemble average of Eq. (46) shows that the long exposure MTF comes from the average mutual coherence function (autocorrelation) of the E-field in the aperture of the lens

$$\langle \tau(\eta) \rangle = A^2 B \langle \int d\mathbf{r} U^*(\mathbf{r} - \lambda R \hat{\mathbf{r}}) U(\mathbf{r}) \rangle = \langle \langle U^*(\mathbf{r}) U(\mathbf{r} + \lambda R \hat{\mathbf{r}}) \rangle \rangle. \quad (59)$$

Rewriting Eq. (56),

$$\bullet^{-\frac{1}{2}} \alpha(\eta) = \frac{\langle \tau(\eta) \rangle_{\text{long exposure}}}{\tau_0(\eta)} = \frac{\langle \langle U(\mathbf{r}') U(\mathbf{r}' + \eta) \rangle \rangle}{\langle W(\mathbf{r}') W(\mathbf{r}' + \eta) \rangle}. \quad (60)$$

Equation (60) is suitable for investigating the wave structure function $D(r)$ since computer simulations provide the E-fields U and W on the right hand side of Eq. (60).

Fried (1966, p.1380-1384) derived the wave structure function for a spherical wave based on the three-dimensional spatial frequency spectrum of refractive index fluctuations, $\Phi_n(\kappa, z)$,

$$D(r) = 8\pi^2 k^2 \int_0^L dz \int_0^\infty \left[1 - J_0\left(\frac{\kappa r}{L}\right) \right] \Phi_n(\kappa, z) \kappa d\kappa, \quad (61)$$

where z represents the position along the optical path length, $0 < z < L$. Fried analytically solves Eq. (61) for a spherical wave and simple Kolmogorov

turbulence that has an index of refraction structure function

$$D_n(r, z) = C_n^2(z) r^{5/3}, \quad (62)$$

and a three-dimensional spatial spectrum of refractive index fluctuations

$$\Phi(\kappa, z) = 0.033 C_n^2(z) \kappa^{-11/3}. \quad (63)$$

Substituting Eq. (63) into Eq. (61) and integrating over spatial frequency κ gives

$$D(r) = 2.91 k^2 r^{5/3} \int_0^L dz C_n^2(z) \left(\frac{z}{L}\right)^{5/3}. \quad (64)$$

Assuming $C_n^2(z) = \text{constant}$ along the optical path gives

$$D(r) = 1.089 k^2 C_n^2 L r^{5/3}. \quad (65)$$

This equation relates the wave structure function $D(r)$ to physical parameters $k=2\pi/\lambda$, C_n^2 , and L for the propagation through turbulence. Following Fried and defining the constant r_0 ,

$$r_0 = \left(\frac{0.86}{1.089 k^2 C_n^2 L} \right)^{3/5}, \quad (66)$$

Eq. (65) becomes

$$D(r) = 0.86 \left(\frac{r}{r_0} \right)^{5/3}. \quad (67)$$

The parameter r_0 characterizes the coherence length of the E-field because the

resolution allowed by the turbulent atmosphere is $\theta_R = \lambda / r_0$ (Fried, 1966, p. 1380-1384).

Substituting Eq. (67) into Eq. (60) gives

$$e^{-2.44 \left(\frac{W}{r_0} \right)^{5/3}} = \frac{\langle \langle U(r') U(r'+r) \rangle \rangle}{\langle \langle W(r') W(r'+r) \rangle \rangle}, \quad (68)$$

and now directly relates a measure of the coherence length, r_0 , to the E-fields produced by computer simulation. Similarly, substituting the integral form of the wave structure function, Eq. (61), into Eq. (60) and numerically integrating for spectra $\Phi_n(x, z)$ with different inner scales allows comparing theory and computer simulation. This comparison facilitates validation of the computer simulations incorporating an inner scale at low turbulence strengths where the perturbation-based theory remains valid, and provides a mechanism to explore conditions of high turbulence strength and/or long propagation path lengths (the saturation regime) where the perturbation theory may no longer hold.

III. COMPUTER SIMULATION

A. PROPAGATION CODE

These investigations utilized a wave optics computer simulation code written by Brent Ellerbroek at the United States Air Force Phillips Laboratory in Albuquerque, New Mexico that incorporates phase screen generation routines written by Greg Cochrane, also with the Phillips Laboratory. The code, known as YAPS (Yet Another Propagation Simulation), is a general purpose adaptive optics simulation code written in FORTRAN that models optical propagation through a turbulent atmosphere, sensing of the wavefront with Hartmann elements (Hudgin, 1977) and a CCD array, optimized phase correction calculation, and phase compensation via a deformable mirror, all within a time indexed framework. These investigations utilized only the propagation portions of the code, modified the code to parameterize turbulence strength with C_n^2 instead of r_0 , added different source configurations, incorporated Gaussian, Hill, and Frehlich inner scales, and reduced the memory requirements.

The computer simulation utilizes the split-step method to simulate propagation of the E-field through turbulence, as illustrated in Fig. (9). A source E-field (left) was propagated in steps (with zero turbulence) over the propagation distance L with a random phase screen applied to the field at each

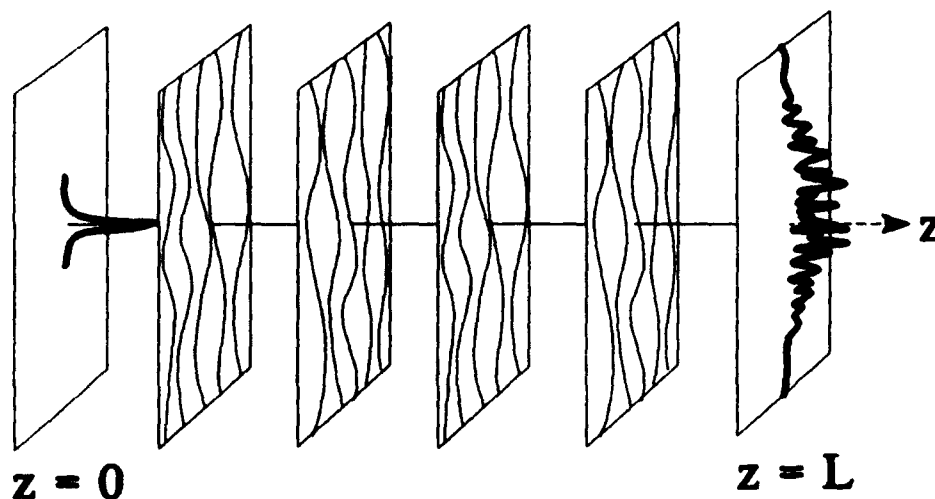


Figure 9 Computer simulation using the split-step method. The source (left) is propagated in steps out to $z = L$, with phase screens applied at each step.

step. This method was based upon the extended Huygens-Fresnel principle (Yura, 1992)

$$E_p = \frac{-i}{\lambda} \iint_A E_A \frac{e^{ik\eta}}{\eta} K(\theta) e^{\gamma} dA, \quad (69)$$

which is Eq. (10) with an extra e^{γ} factor that incorporates the random variations in log amplitude ℓ and phase ϕ

$$e^{\gamma} = e^{\ell} e^{i\phi}. \quad (70)$$

For paraxial propagation, if the distances η are short enough, diffraction and

interference will not have a chance to cause significant log amplitude fluctuations ℓ , allowing the approximation

$$\overline{e^{\ell}} = e^{\ell^2/2}. \quad (71)$$

Inserting this approximation into Eqs. (11) - (19) gives

$$E(\hat{r}, z) = \int d\hat{r}' e^{i2\pi\hat{r}'z/\lambda} e^{-i\pi\lambda z|\hat{r}'|^2} \int d\hat{\rho} E(\hat{\rho}, 0) e^{i\phi(\hat{\rho})} e^{-i2\pi\hat{\rho}\hat{r}'}. \quad (72)$$

Thus, a single step of the split-step method requires applying the phase screen $e^{i\phi}$ to the E-field and propagating the result a distance z using the Huygens-Fresnel propagator.

To implement this sequence of steps, the YAPS code followed a user-defined list of tasks (stored as an input file) and called the appropriate routines to accomplish those tasks. For these investigations, a typical list (see the Appendix) first set up the initial parameters, including random number seed, wavelength, number and size of fields, source characteristics, and phase screen size. The list then initialized the field grid and applied the initial source distribution, propagated the field in steps, generated and applied phase screens between steps, and finally saved the complex values of the propagated field.

The YAPS propagations were run on Sun SparcStation-10's having 128 megabytes of RAM. This memory constraint allowed a maximum grid size of 1024x1024 (choosing N as an integer power of 2) for the current version of YAPS. Each run consisted of 30 propagations, each with 32 phase

screens/steps, and required ~16 hours to complete. These investigations normally utilized nine SparcStation-10's simultaneously doing runs with different parameters. In all, these investigations consumed roughly 6000 hours of computer time. A small Cray mainframe was available with more RAM, but was not utilized extensively because the multiple SparcStations provided more overall computational capacity.

Once the YAPS code had generated and saved the realizations of the E-field propagated through turbulence, separate routines written in Interactive Data Language (IDL) analyzed and displayed the fields. Analysis included displaying two- and three-dimensional plots of the intensity field, calculating the dependence of intensity and normalized irradiance variance on radial distance, calculating the normalized irradiance variance over the central portion of the field, calculating the atmospheric MTF and corresponding coherence length, and calculating Strehl and intensity ratios (defined in **Section E** below).

The wave optics computer simulation required many choices to model the stratospheric propagation scenario and to ensure validity of the simulation. These choices included wavelength, propagation distance, inner scale, grid size N , the physical size of each grid element Δx , the maximum strength of turbulence β_0^2 , the source function of the E-field, the number of phase screens, low spatial frequency corrections, number of realizations, and methods

of calculating average statistical values. The following sections address these and other choices and develop guidelines for validity of the simulations.

B. PHYSICAL PARAMETERS

Wave optics computer simulation of the E-field requires selection of the parameters that describe the physical properties of the propagation. Usually a specific propagation scenario has been selected for modeling, giving the desired wavelength λ , wavenumber $k=2\pi/\lambda$, propagation distance L , and the range of turbulence strengths C_n^2 . The stratospheric propagation scenario chosen here used $\lambda = 500$ nm, $L = 200$ km, and $C_n^2 = [1 \times 10^{-21}, 1 \times 10^{-16}] \text{ m}^{-2/3}$. From these physical parameters, other useful scaling parameters occur, such as the Fresnel wavenumber (Martin and Flatté, 1988)

$$\kappa_f \equiv R_f^{-1} \equiv \left(\frac{k}{L}\right)^{1/2} = \sqrt{\frac{2\pi}{\lambda L}}, \quad (73)$$

the Rytov-Tatarski normalized irradiance variance (Flatté, Wang, and Martin, 1993)

$$\frac{\sigma_I^2}{\bar{I}^2} = \alpha C_n^2 k^{7/6} L^{11/6} \equiv \beta_0^2, \quad (74)$$

where $\alpha=1.23$ for plane waves and $\alpha=0.497$ for spherical waves, and Fried's coherence length for spherical wave propagation (Fried, 1966, p.1380-1384)

$$\begin{aligned}
 r_0 &= \left(\frac{6.88}{2.91 k^2 \int_0^L dz C_n^2(z) \left(\frac{z}{L}\right)^{5/3}} \right)^{3/5} \\
 &= \left(\frac{6.88}{1.09 k^2 C_n^2 L} \right)^{3/5} \quad (\text{for constant } C_n^2).
 \end{aligned}
 \tag{75}$$

The inner scale of the turbulence, ℓ_0 , often is not known exactly, but values can be estimated. For stratospheric propagation, estimates of the inner scale are around 1 - 15 cm (Beland, 1993). Once the inner scale is known, the Hill and Frehlich versions of the viscous-convective enhancement inner scales (Hill and Clifford, 1978) (Frehlich, 1992) were implemented with the parameter $\kappa \ell_0$, where κ represents spatial frequency. The outer scale L_0 for stratospheric propagation lies in the range of tens to hundreds of meters but, again, due to the difficulty in parameterization, was not included in these simulations.

C. COMPUTATION GRID

The E-field was represented as an NxN array of complex numbers in the plane perpendicular to the axis of propagation. Generally, N was chosen as large as possible, consistent with the amount of computer memory available and the time required to run a simulation. Larger grid size N allowed a wider spatial extent of the field and/or sampling of higher spatial frequencies (denser mesh). The physical size that each grid element represented had to be chosen to ensure validity of the computer simulation.

Knepp (1983) discussed the relation of grid element size Δx and physical grid extent $N\Delta x$ to inner and outer scales, to proper sampling of the phase screens, to angular spreading of the field, and to proper sampling of the spatial frequency quadratic phase factor in the Fourier transform formulation of the Huygens-Fresnel propagation. For the latter, the quadratic phase factor in Eq. (20) takes the form

$$\phi = \frac{\kappa^2 L}{2 k}, \quad (76)$$

where κ is a spatial wavenumber in rad/m. Applying the Nyquist criterion, which requires that this quadratic phase change by less than π across one grid element Δx , Knepp derives

$$L < \frac{2 N (\Delta x)^2}{\lambda}. \quad (77)$$

Roberts (1986) applied similar techniques and derived Eq. (77) without the factor of 2. Again applying the Nyquist criterion to the quadratic phase factor in the Fourier transform propagator Eq. (20) but utilizing more succinct differential notation,

$$\frac{d\phi}{df} = \frac{d}{df} (\pi \lambda L f^2) = \frac{\Delta\phi}{\Delta f}, \quad (78)$$

and,

$$\Delta\phi = \Delta f 2 \pi \lambda L f_{\max} < \pi, \quad (79)$$

where f_{\max} represents the spatial frequency with the maximum rate of change of phase. At the edge of the grid, f_{\max} is

$$f_{\max} = \frac{N}{2} \Delta f = \frac{N}{2} \frac{1}{N \Delta x} = \frac{1}{2 \Delta x}. \quad (80)$$

After substituting and rearranging,

$$L < \frac{N (\Delta x)^2}{\lambda}. \quad (81)$$

When the propagation distance L is known, as for a specific propagation scenario, and when the grid dimension, N , is known, then the grid element size is

$$\Delta x > \sqrt{\frac{\lambda L}{N}}. \quad (82)$$

Sampling of the phase factor in the spatial frequency domain must meet the Nyquist criterion as a minimum. Some circumstances may warrant applying even stricter sampling criteria such as restricting the phase to change by less than $\alpha\pi$ across one grid element, $0 < \alpha < 1$. Furthermore, suppose the propagation involves spatial frequencies out to βf_{\max} , where $0 < \beta < 1$. Then

$\Delta\phi < \alpha\pi$, and the maximum spatial frequency is βf_{\max} . Substituting these constraints into the analysis gives

$$\Delta x > \sqrt{\frac{\lambda L \beta}{N \alpha}}. \quad (83)$$

Whichever is used, Eq. (82) and (83) provide simple formulas for choosing the minimum grid element size for the propagation.

Spherical wave propagation places an additional constraint on the choice of grid element size. In the parabolic approximation, a spherical wave has a quadratic phase curvature which represents divergence from a point source a distance S (focal distance) away

$$\phi = \frac{\pi \rho^2}{\lambda S}, \quad (84)$$

where ρ measures the radial distance from the propagation axis. Roberts (1986) analyzed the sampling criteria for this phase just as for the spatial frequency phase (though applied to the case of a two-step Fourier transform Huygens-Fresnel propagator and not applied specifically to spherical waves). Proceeding as above and applying the Nyquist criterion to this phase factor

$$\frac{d\phi}{d\rho} = \frac{d}{d\rho} \left(\frac{\pi \rho^2}{\lambda S} \right) = \frac{\Delta\phi}{\Delta\rho}. \quad (85)$$

$$\Delta\phi = \frac{\Delta\rho}{\lambda} \frac{2\pi}{S} \rho_{\max} < \pi. \quad (86)$$

where ρ_{\max} represents the maximum radial distance. Using ρ_{\max} corresponding to the edge of the grid and $\Delta\rho = \Delta x$,

$$\rho_{\max} = \frac{N}{2} \Delta\rho = \frac{N \Delta x}{2}. \quad (87)$$

Substituting Eq. (87) into Eq. (86) and rearranging,

$$\Delta x < \sqrt{\frac{\lambda S}{N}}. \quad (88)$$

Again generalize the analysis by requiring the maximum phase change across one element to be $\alpha\pi$ ($0 < \alpha < 1$), and requiring the field energy to be confined within a region of radius $\gamma\rho_{\max}$, ($0 < \gamma < 1$). This gives

$$\Delta x < \sqrt{\frac{\lambda S \alpha}{N \gamma}}. \quad (89)$$

Combining Eq. (83) and (89),

$$\sqrt{\frac{\lambda L \beta}{N \alpha}} < \Delta x < \sqrt{\frac{\lambda S \alpha}{N \gamma}}. \quad (90)$$

Spatial frequency sampling considerations for the Huygens-Fresnel propagator have placed a lower limit on Δx , while spatial sampling considerations of the

quadratic approximation for spherical wave phase have placed an upper limit on Δx .

The computer simulations used in these investigations examined high levels of turbulence that introduced energy into the highest spatial frequencies representable on the grid and that scattered energy to the edges of the spatial grid. The simulations also assumed that the Nyquist sampling criterion was sufficient. These considerations specified the parameters $\alpha = \beta = \gamma = 1$, and lead to

$$\sqrt{\frac{\lambda L}{N}} < \Delta x < \sqrt{\frac{\lambda S}{N}}. \quad (91)$$

Additionally, these simulations propagated a spherical wave from the point source at the origin (focus) out to a distance S , i.e. $S = L$, making the inequalities in Eq. (91) become the equality

$$\Delta x = \sqrt{\frac{\lambda L}{N}}. \quad (92)$$

These choices unambiguously determine the guideline for grid element size for spherical wave propagation based upon sampling considerations in the spatial and spatial frequency domains. Equation (92) also determines the grid element size for plane wave propagation since minimizing the grid element size of

Eq. (82) optimizes the sampling of high spatial frequency distortions caused by turbulence.

Some simplifications were made in the above analysis. First, the maximum spatial distance and maximum spatial frequency used in the quadratic phase factors were chosen for the nearest edge of the grid and correspond to the radius of the largest circle that will fit inside the grid. These choices disregarded the corners of the grid, but this omission should not have affected the simulations greatly because the majority of the energy in both the spatial and spatial frequency domains was confined within the radius of the circle to minimize aliasing. Second, the Nyquist criterion was applied to the phase change across the x or y dimension of the element. Analyzing the phase change between opposite corners of a grid element increases Δf or Δp by $\sqrt{2}$. Finally, an NxN grid with N even requires placing the $(x,y) = (0,0)$ point at a grid point, such as $(N/2 + 1, N/2 + 1)$ that is not the exact geometric center of the grid. The distance to the nearest side is $(N-2)/2$ elements instead of $N/2$, which is a minor change for large N. Incorporating these three considerations into the analysis for a spherical wave gives

$$\sqrt{\frac{2 \lambda L (N-2)}{N^2}} < \Delta x < \sqrt{\frac{\lambda S}{2 (N-2)}} \quad (93)$$

However, squaring Eq. (93) and rearranging leads to

$$L < \frac{1}{4} \frac{N^2}{(N-2)^2} S, \quad (94)$$

so that a spherical wave propagation with these additional constraints should only be carried out over a maximum distance less than $S/4$. Since these investigations needed to propagate a spherical wave over the full focus distance S starting at the source, the simpler expression Eq. (92) was used to determine the grid element size for these investigations. As a comparison, Flatté, Wang, and Martin (1993) used a grid element size of 0.7mm for a 1024x1024 grid and 0.5mm for a 2048x2048 grid with $\lambda L = 0.000638 \text{ m}^2$. Equation (92) with these parameters prescribes grid element sizes of 0.78 mm and 0.55 mm, respectively, which are ~10% larger to meet sampling considerations for the Huygens-Fresnel propagator.

The split-step method in the computer simulation divides the optical path into multiple steps. However, the distance L used to determine the grid element size must correspond to the total propagation path length and not the step size. To justify this, consider the vacuum propagation of a field across the distance $L = \Delta z$. If propagation occurs in a single step, then the Fourier transform Huygens-Fresnel propagator, Eq. (20), becomes

$$E(\Delta z) = \text{IFT} \left[e^{-i\pi \lambda \Delta z / f^2} \text{FT}[E(0)] \right]. \quad (95)$$

If the path has two steps, then

$$E(\Delta z) = IFT \left[e^{-i\pi\lambda \frac{\Delta z}{2} f^2} FT[E(\Delta z/2)] \right], \quad (96)$$

and

$$E(\Delta z/2) = IFT \left[e^{-i\pi\lambda \frac{\Delta z}{2} f^2} FT[E(0)] \right]. \quad (97)$$

Substituting Eq. (97) into Eq. (96),

$$E(\Delta z) = IFT \left[e^{-i\pi\lambda \frac{\Delta z}{2} f^2} FT \left[IFT \left[e^{-i\pi\lambda \frac{\Delta z}{2} f^2} FT[E(0)] \right] \right] \right]. \quad (98)$$

But the middle Fourier transform/ inverse Fourier transform pair cancel each other, and this two step vacuum propagation becomes the one step propagation of Eq. (95). Thus, the grid element size must be chosen to correspond to the total distance $\Delta z = L$ since multi-step vacuum propagations mathematically reduce to a single step of L .

D. SOURCES

The choice of a given propagation scenario significantly affects the irradiance and coherence statistics. Plane wave propagation differs from spherical wave propagation, as seen in the Rytov-Tatarski theory (Tatarski, 1961), while beam wave propagation (Gaussian intensity profile) exhibits an intermediate behavior (Ishimaru, 1978). The source must also be chosen to

keep the lateral extent of the source propagation within the spatial and spatial frequency limits of the computer simulation.

Coherent plane, beam, and spherical waves differ in the shape of the isophase surfaces of the E-field. Beam wave sources possess a quadratic phase (Ishimaru, 1978),

$$\phi(\rho) = \frac{i \pi}{\lambda R_0} \rho^2, \quad (99)$$

where R_0 represents the radius of curvature of the wavefront. Plane wave sources have an infinite radius of curvature so that

$$\phi(\rho) = \text{constant}. \quad (100)$$

Spherical wave sources have a radius of curvature equal to the propagation distance from the origin, or focus, S

$$\phi(\rho) = \frac{\pi \rho^2}{\lambda S}. \quad (101)$$

Turbulence introduces random phase shifts across the wavefront while diffraction and interference further distort the wavefront during propagation causing the light to become partially coherent. The resulting partially coherent E-field no longer possesses a simple isophase surface and the coherent wavefront characterizations no longer apply. The differences between plane, beam, and spherical propagation appear in differences in statistical properties,

such as normalized irradiance variance (Tatarski, 1961)

$$\frac{\sigma_I^2}{\bar{I}^2} = \begin{cases} 1.23 C_n^2 k^{7/6} L^{11/6}, & \text{plane} \\ 0.497 C_n^2 k^{7/6} L^{11/6}, & \text{spherical} \end{cases} \quad (102)$$

(see Ishimaru, 1978 for the more complicated beam wave expression), and the coherence length (Fried, 1966, p. 1380-1384)

$$r_0 = \begin{cases} 3.02 (C_n^2)^{-3/5} k^{-4/5} L^{-3/5}, & \text{spherical} \\ 1.68 (C_n^2)^{-3/5} k^{-4/5} L^{-3/5}, & \text{plane.} \end{cases} \quad (103)$$

When the E-field has propagated through turbulence to the far field of the source, diffraction has caused the E-field to expand laterally so that its statistical properties approach those of a spherical wave. The far field begins at a distance (Saleh and Teich, 1991)

$$z \approx 10 \frac{\rho^2}{\lambda}, \quad (104)$$

where ρ is the radius of the source. Spherical propagation properties result when the maximum radius of the source ρ_{\max} approximately satisfies

$$\rho_{\max} < \sqrt{0.1 \lambda z}. \quad (105)$$

For a stratospheric propagation scenario with $L=200$ km and $\lambda = 500$ nm, the

source radius must be less than 10 cm to obtain enough divergence to produce spherical propagation statistics at $z = L$.

Plane wave propagation statistical properties result when the E-field is evaluated in the near field of the source because the E-field does not have the opportunity to diffract or expand significantly. Starting with Eq. (105) for the far field point, near field propagation satisfies

$$z \approx \frac{1}{10} \frac{\rho^2}{\lambda} \ll 10 \frac{\rho^2}{\lambda}, \quad (106)$$

or,

$$\rho_{\max} > \sqrt{10 \lambda z}. \quad (107)$$

For the stratospheric propagation scenario, source radius $\rho_{\max} > 1$ m for near field propagation. However, validity of the Fresnel approximation to the Huygens-Fresnel equation places an upper bound on ρ_{\max} (Saleh and Teich, 1991)

$$(\rho_{\max}^2)^2 \ll 4 z^3 \lambda, \quad (108)$$

(derived from considering the Taylor series expansion of the Cartesian expression for r). For the $L = 200$ km, $\lambda = 500$ nm stratospheric propagation scenario, the upper bound on source lateral extent becomes $\rho_{\max} < 350$ m. A 1024×1024 grid with the grid element size $\Delta x = 0.99$ cm from Eq. (92) gives a

maximum grid radius of only 5 m, so that the Fresnel approximation is satisfied for any source represented on this grid.

Ishimaru (1978) evaluated the irradiance statistics for the intermediate Gaussian beam wave case. The normalized irradiance variance along the beam axis depends upon the beam waist size, W_0 , and the radius of curvature, R_0 . Numerical integration of the log amplitude variance formula (Walters, 1994) provides a smooth transition from spherical wave variance statistics to plane wave statistics, with a dip in between, as shown in Fig. (10). Numerical simulation results with Gaussian and Airy-type sources of varying widths have a corresponding behavior, as shown in Fig. (11).

The finite grid in a computer simulation places limitations on the source E-field. The physical grid element size sets a lower bound on the width of a narrow source approximating a point source. A source of width close to a single grid element may still be undersampled, causing the resulting propagated field to exhibit sidelobes from absence of the proper high spatial frequencies in the representation. Correspondingly, a spherical wave from a very narrow source will propagate with large angular divergence that may exceed the physical dimensions of the grid and cause energy to leak off the grid and be aliased back into the field. Thus, the source must be wide enough to constrain the propagated field so that most (>90%) of the energy remains within the grid.

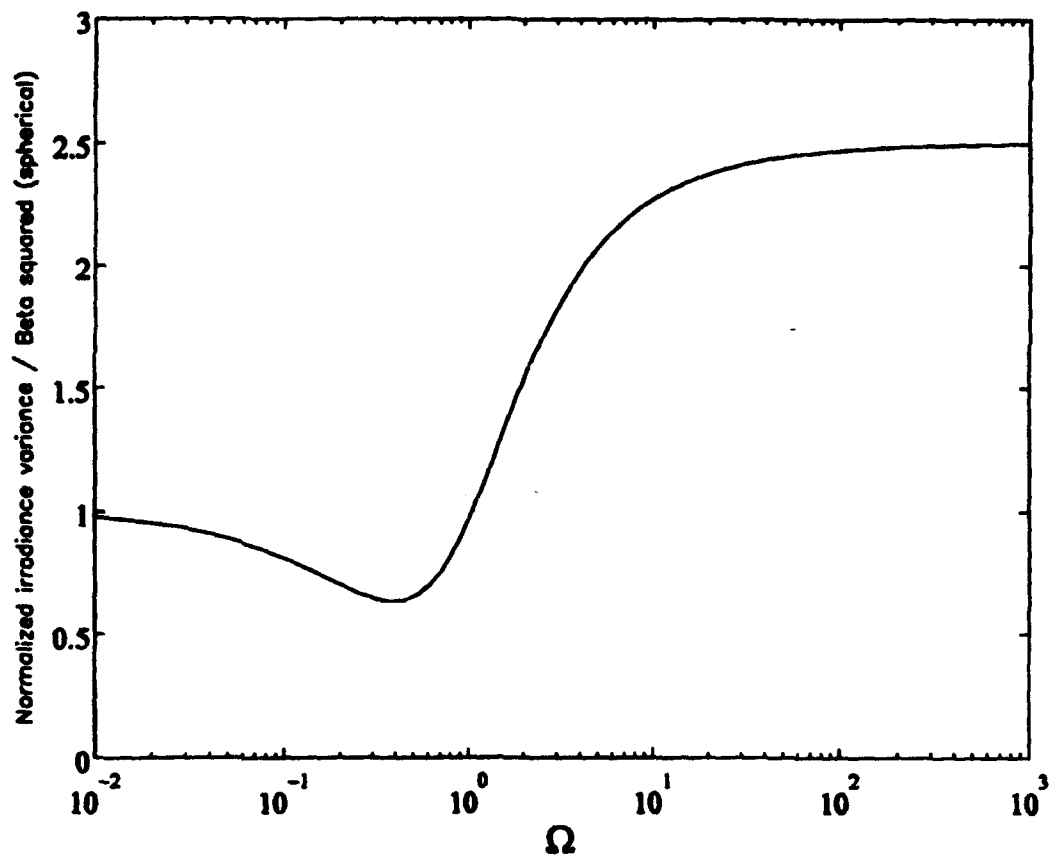


Figure 10 Normalized irradiance variance versus beam waist size W_0 , where $\Omega = \pi W_0^2 / \lambda L$, from numerical integration of Ishimaru's predictions for beam waves.

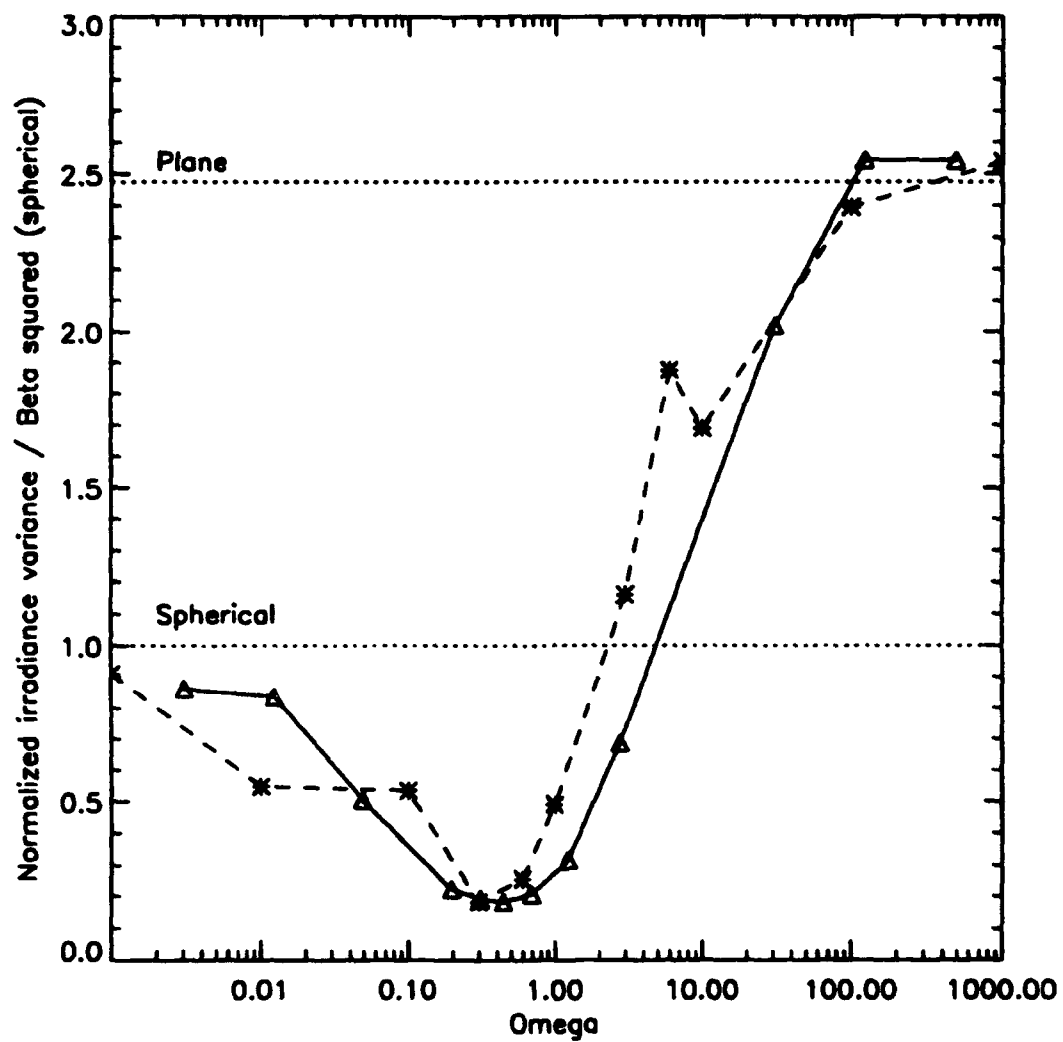


Figure 11 Normalized irradiance variance versus beam waist size W_0 , where $\Omega = \pi W_0^2 / \lambda L$. Solid line = Airy-type source; dashed line = Gaussian source.

Similarly, a plane wave source cannot extend too near the grid edge because turbulence can scatter energy off the grid only to be aliased back in.

Statistical calculations on the final beam pattern require a reasonably uniform central patch to perform computations. If the region over which statistical calculations are made has variations, such as sidelobes arising simply from vacuum propagation, these variations become a part of the statistics, such as the normalized irradiance variance. Often, Gaussian type profiles present a minimum of such variations because they do not have as much energy in high spatial frequencies. However, because they are not flat over the calculation region, different regions of the beam must often be weighted with respect to their mean intensity in doing statistical calculations such as the normalized irradiance variance.

To meet these constraints, Martin and Flatté (1990) applied a quadratic phase curvature to a Gaussian source, thereby increasing the divergence and flattening the final irradiance pattern. Spherical wave sources were simply chosen narrower than the plane wave sources to make them diverge more. Flatté, Wang, and Martin (1993) also used a super-Gaussian to model an extended beam source.

The simulations presented here used an alternate method suggested by Ellerbroek (1993). The final field at $z = L$ was specified as an aperture of radius equal to one half the grid radius and given a quadratic phase

corresponding to a spherical wave originating at the origin $z = 0$ (Fig. (12)). This aperture field was then backward propagated without turbulence from $z = L$ to the focus $z = 0$, effectively Fourier transforming the field and yielding the numerical equivalent of the Airy pattern (Fig. (13)). This source was then used as the approximation to a point source for all spherical wave propagations. The advantages of this method were that the source was quite narrow, having appreciable amplitude over only a few grid elements, and that the zero turbulence propagated field at $z = L$ was necessarily constrained within the grid and possessed a central region with uniform illumination.

The significant energy at high spatial frequencies required to represent the sharp edges of the initial aperture at $z = L$ created one drawback since it caused strong Fresnel fluctuations at intermediate distances between 0 and L . To investigate the significance of these Fresnel fluctuations, the energy at these high spatial frequencies were reduced by windowing the aperture before the backward propagation by applying a Gaussian rolloff to the cylinder edges,

$$|E| = \begin{cases} 1 & , \quad r < 0.7 r' \\ \exp \left(- \left[\frac{r - 0.7 r'}{0.3 r'} \right]^2 \right) & , \quad r \geq 0.7 r', \quad n=2, \end{cases} \quad (109)$$

where r' represented the corresponding aperture radius. Because this rolloff reduced the energy in high spatial frequencies for the source representation, this slightly increased the size of the final central region of the E-field where

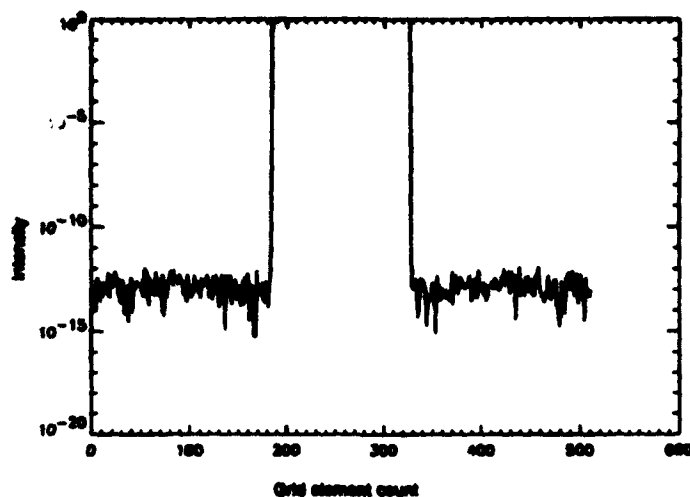


Figure 12 Cross section of intensity profile for final propagated beam showing confinement of energy and uniform central illumination (beam radius = 70 grid elements here).

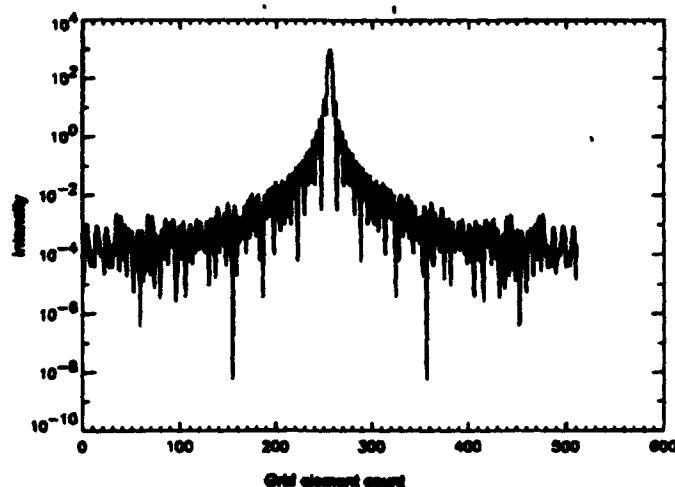


Figure 13 Cross section of intensity profile of numerical equivalent to Airy source.

statistical calculations could be performed. Other values for the power n on the exponent were tried ($n = 1$, $n = 5$, $n = 10$) but the simple Gaussian ($n = 2$) worked best. While this rolloff appeared useful, identical runs, one with the sharply defined aperture edge and one with a rolled-off Gaussian edge, showed less than 0.5% difference in the normalized irradiance variance values. This difference was negligible compared to statistical fluctuations in normalized irradiance variance of up to ~10% between runs with different random phase screens. Empirical observation of simulations revealed that once even modest amounts of turbulence existed (typically $\beta_0^2 > 0.05$ and well within the Rytov regime), the high spatial frequency energy introduced by the turbulence dominated the details of the source.

Another deficiency was the representation of the initial cylindrical aperture on a rectangular grid. Due to the Cartesian nature of the grid, the curved beam edge was actually jagged instead of circular. However, for large enough grid (e.g. 1024x1024) this departure from a cylinder introduced negligible effect. The only case where a difference was noted was with a 256x256 grid, and increasing the beam radius a small fraction of a grid element size eliminated that difference.

Another limitation of this method was that the final E-field could not approach the grid radius. If this happened, then high turbulence strengths would scatter energy off the grid, producing aliasing. Due to the periodic

Fourier transform method of propagation, this energy would not be lost, but aliased back in at lower spatial frequencies. Martin and Flatté (1990) implemented an attenuating region just inside the grid radius to absorb this energy and to prevent its being aliased back in. This obviously introduced a type of windowing function in the spatial domain and did not conserve energy in the field, possibly complicating final field comparisons. Rather than include those effects, these simulations simply chose the aperture radius sufficiently small (at one half the grid radius) to prevent significant energy scattering off the grid in the spatial domain while still providing a relatively uniformly illuminated central region for statistical calculations.

Obviously, other choices for a source existed. For example, the initial field could have been expressed according to an analytic expression for the Airy pattern (Fig. (14)). This source gave a vacuum propagated final field that was very close to a broad cylinder, but which exhibited noticeable sidelobes at the edges (Fig. (15)). These sidelobes came from spatial truncation of the Airy pattern. The back propagated numerical Airy pattern of Fig. (13) differs from an analytic Airy pattern in a way that eliminates the sidelobes in the final irradiance field.

A point source could be modeled by a single, nonzero pixel at the center of the grid being nonzero, as shown in Fig. (16). Figure (17) shows that the vacuum propagated field exhibited noticeable sidelobes at the edges and

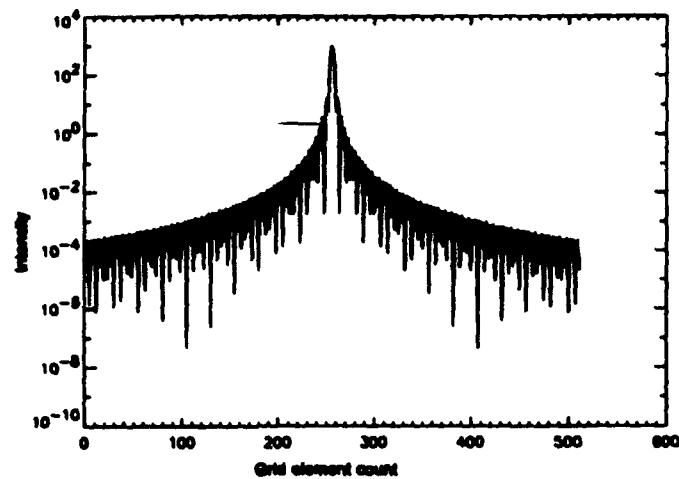


Figure 14 Cross section of intensity profile of analytic Airy source.

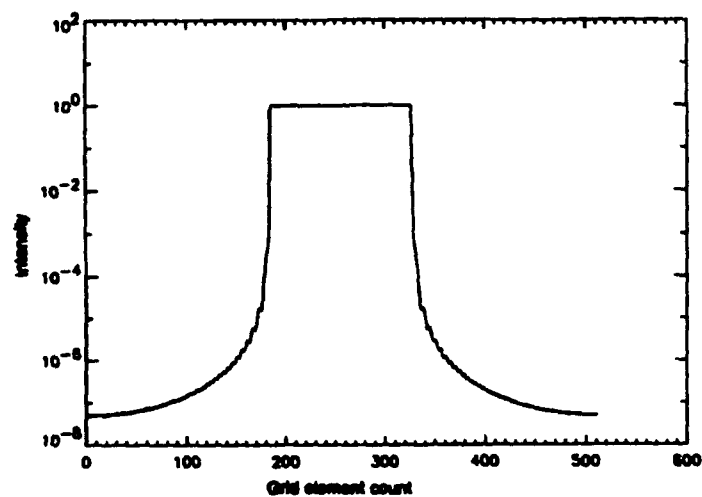


Figure 15 Cross section of intensity profile from analytic Airy source after vacuum propagation.

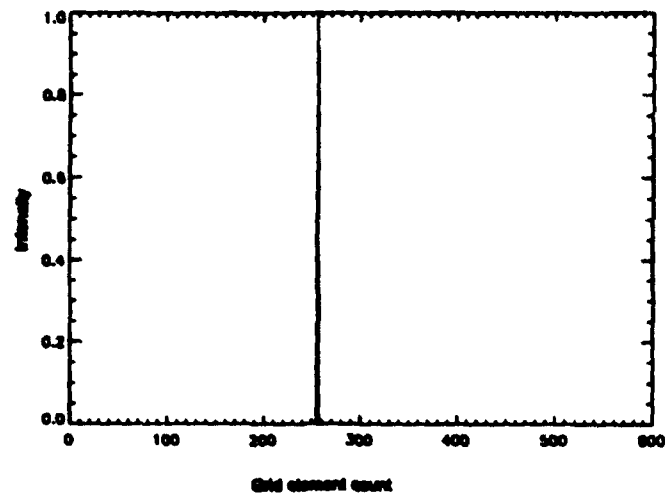


Figure 16 Cross section of intensity profile for the single-grid-element point source.

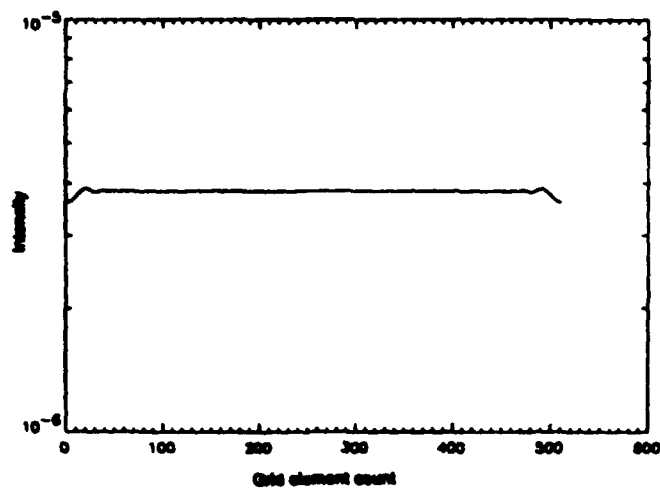


Figure 17 Cross section of intensity profile for single-grid-element point source after vacuum propagation.

covered the entire aperture, meaning that turbulence would immediately scatter energy out of the grid only to be aliased back in and distort the field. A similar source was a uniformly illuminated grid at $z = L$ with quadratic phase, backward propagated to $z = 0$. While this eliminated the vacuum propagation ringing problem by definition, it immediately suffered from aliasing when turbulence was nonzero and scattered energy off the grid.

E. MAXIMUM TURBULENCE STRENGTH

One of the more difficult choices in a computer simulation of propagation is determining the range of turbulence strengths over which a simulation is valid. In general, the processes of optical propagation through a turbulent medium are not band limited in spatial frequency. But when a computer simulation uses a finite grid to implement a source function, to propagate via the Huygens-Fresnel principle, and to model the turbulence by phase screens, aliasing inevitably occurs due to the finite sampling interval. This problem only becomes more severe as turbulence strength increases. The coherence length measures the physical distance over which the mutual coherence of the E-field, $\langle E^* E \rangle$, declines to e^{-1} of its peak value. As turbulence increases, the E-field fluctuates significantly over smaller and smaller distances and the coherence length decreases. An $N \times N$ discrete grid representation of the E-field samples at a specific minimum distance, and hence at a maximum spatial frequency. If the

E-field fluctuates in less than this minimum distance, the grid samples will not represent the E-field accurately, causing aliasing. The question is not whether aliasing occurs, but how much aliasing occurs for a given set of simulation parameters, and at what point does aliasing invalidate the results of the simulation.

These investigations identified three telltale signs of aliasing. First, as aliasing became significant, irradiance plots of the turbulent E-field lost structure and exhibited an isotropic fine-grained appearance, as Fig. (18) shows. Second, the irradiance that should have been roughly radially symmetric

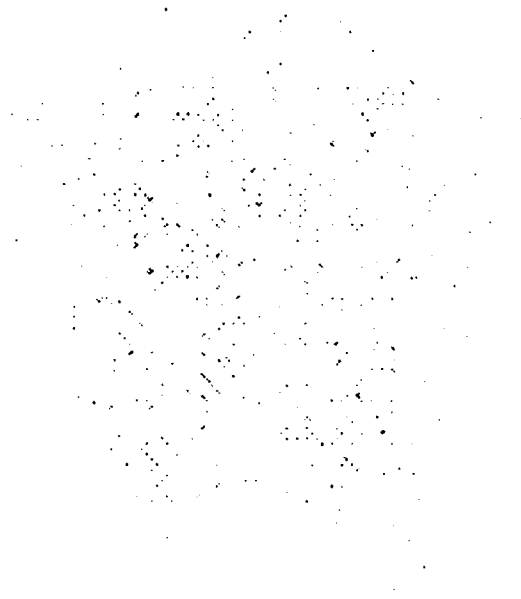


Figure 18 Intensity plot showing fine-grained pattern due to significant aliasing.

became bounded within a fuzzy rectangular region, as Fig. (19) illustrates. The irradiance at the center of the image increased, or started peaking, while the irradiance at the edges decreased, as shown in Fig. (20).

Figure (21) also illustrates this peaking behavior by plotting average irradiance versus radius, in units of grid element size. The E-field propagated with zero turbulence had the radially symmetric aperture profile in this simulation. As the turbulence became stronger, the sharp edges of the initial cylindrical irradiance pattern became rounded and energy spread outward. However, when significant aliasing started occurring around $\beta_0^2 \sim 5$ for this 64x64 grid representation, the energy began creeping inward and the center of the field started increasing in irradiance.

The irradiance at the edge of the grid was $\sim 1/40$ that of the center when significant aliasing began. This indicates that very little energy leaked off the spatial grid due to beam divergence. Actually, the use of Fourier transforms in the propagation preserved the energy so that any energy that leaked off the grid was aliased back into the field on the grid. Energy that leaks off in the spatial domain results from undersampling in the spatial frequency domain, and vice versa.

Aliasing most often occurs from undersampling in the spatial domain, which corresponds to energy leaking off the grid in the spatial frequency domain. Prudent choice of source and the final irradiance patterns across the

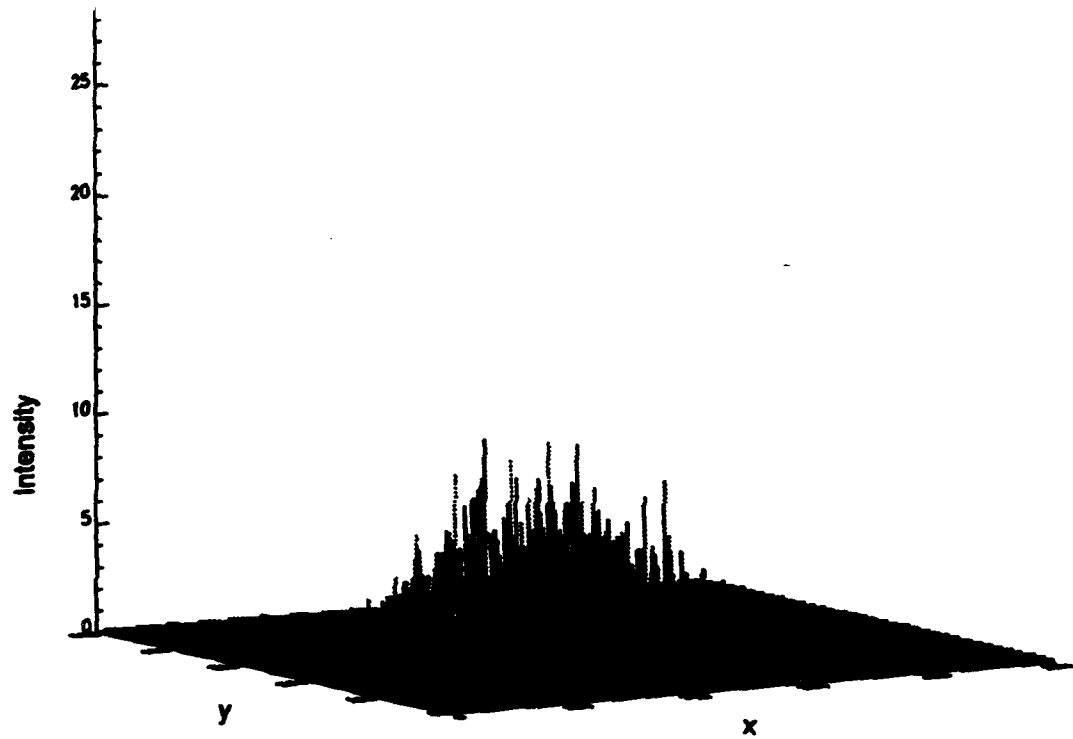


Figure 19 Intensity plot showing boxed perimeter due to significant aliasing.

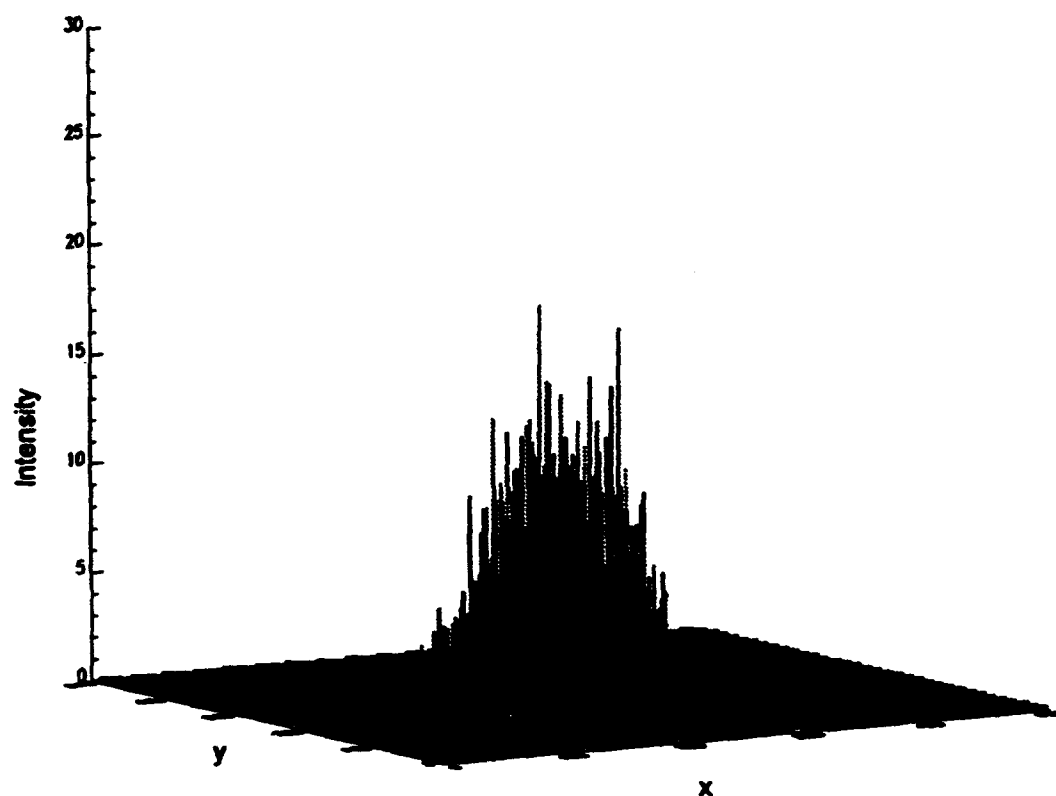


Figure 20 Intensity plot showing peaking of energy toward center due to significant aliasing.

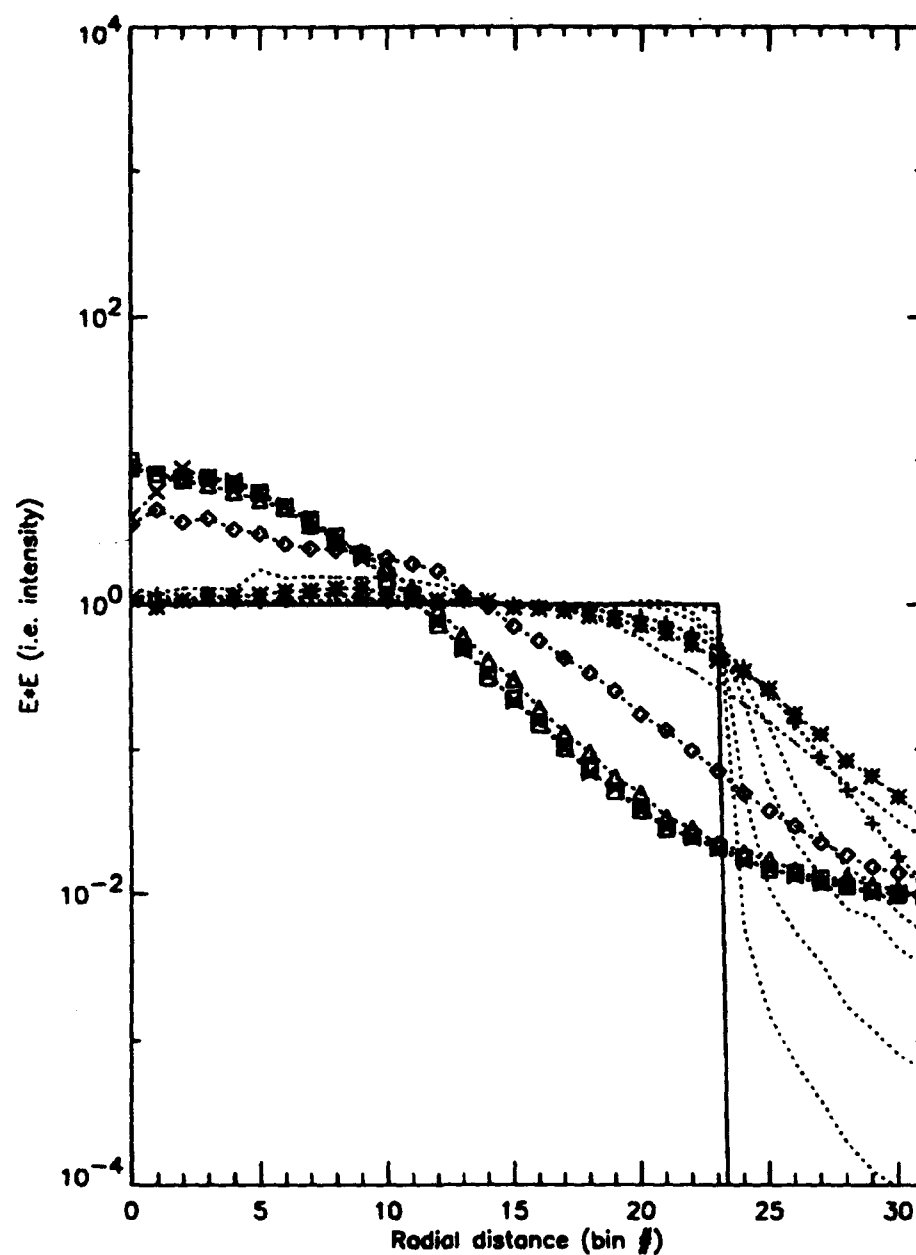


Figure 21 Radial intensity profiles showing peaking behavior: $\beta_0^2 = 0$ (solid line), 0.5 (pluses), 1.5 (asterisks), 5 (dots), 15 (diamonds), 50 (triangles), 150 (squares), 500 (X's).

grid can minimize the amount of energy that leaks off the grid to be aliased back in for the spatial domain. However, as turbulence strength increases, the coherence length decreases and more energy occurs at higher and higher spatial frequencies. Eventually spatial undersampling occurs and this high spatial frequency energy leaks off the spatial frequency grid and is aliased back in. Figure (22) gives the radial power spectral density corresponding to Fig. (21) and shows the spread of energy to higher spatial wavenumbers as turbulence strength increases. The low turbulence spectra possess a strong central peak that becomes more rounded and flatter as turbulence strength increases, causing more energy to leak off the grid. Eventually, enough energy has leaked off the grid and aliased back in to make the spectrum approximately uniform at all spatial frequencies.

Figure (23) actually shows this energy being reflected back in after it spills off. To reveal this phenomenon, the radial power spectrum for a 512x512 grid has been divided by the corresponding part of the power spectrum on a 1024x1024 grid. Since the larger grid has been chosen with a finer mesh than the 512x512 grid, the larger grid will not experience significant aliasing as soon. As turbulence strength increases, the ratio shows the enhancement of energy at the edge of the 512x512 grid (bins 200-256) as the energy leaks off / reflects back in. At very high levels of turbulence, the aliased energy has spread inward over all spatial frequencies.

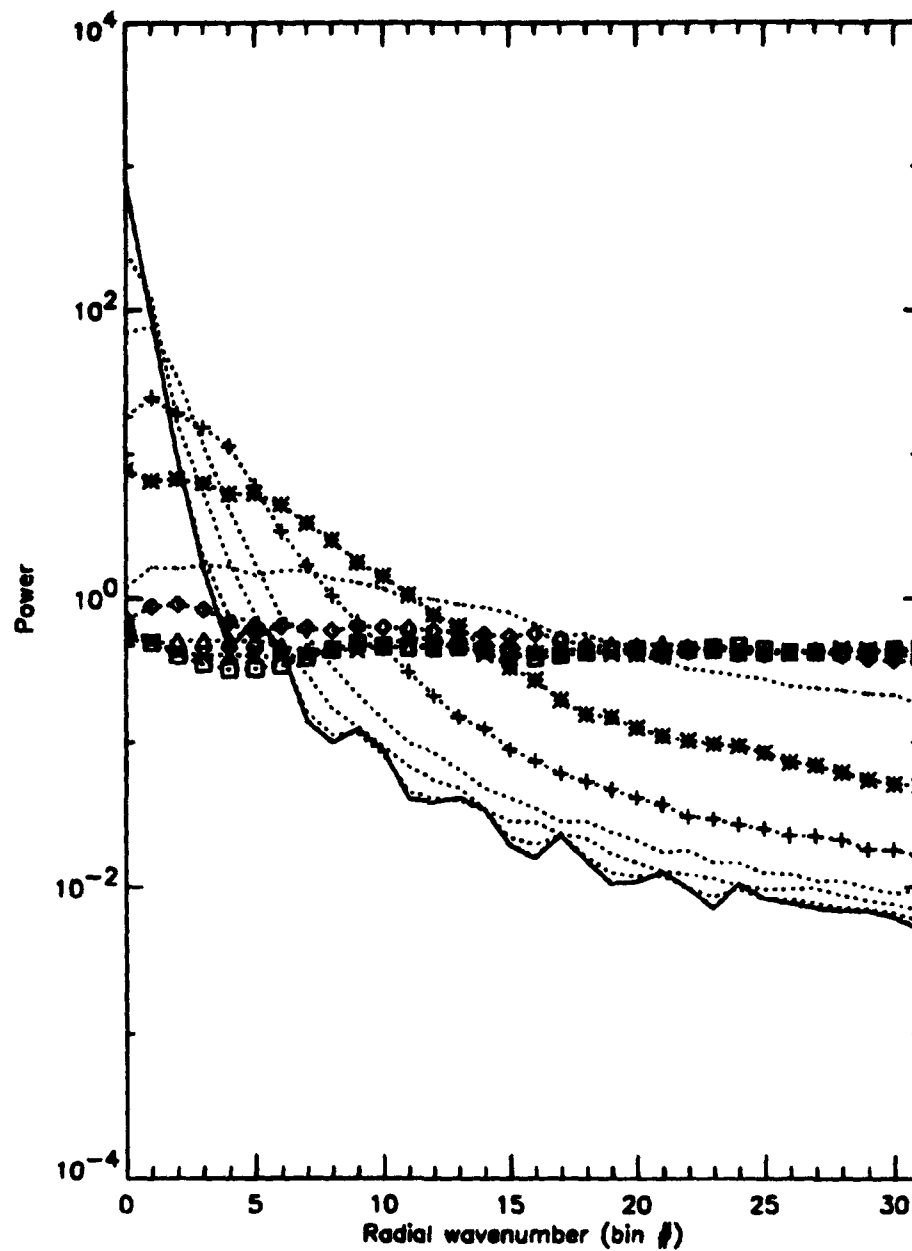


Figure 22 Power spectrum radial profile as turbulence strength increases: $\beta_0^2 = 0$ (solid line), 0.5 (pluses), 1.5 (asterisks), 5 (dots), 15 (diamonds), 50 (triangles), 150 (squares), 500 (X's).

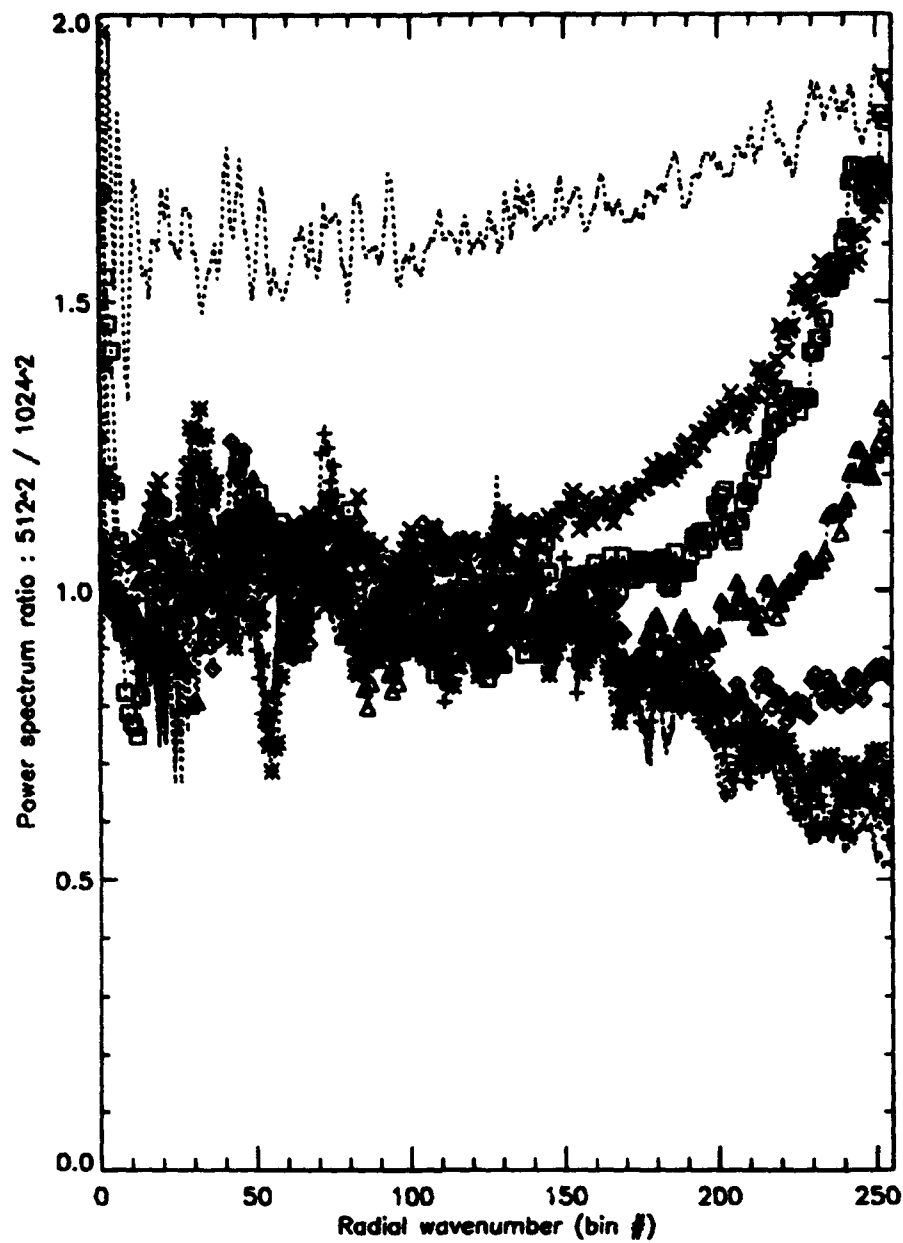


Figure 23 Power spectrum radial profile for 512x512 grid, divided by 1024x1024 profile, showing energy aliasing back in. $\beta_0^2 = 0.15$ (plus), 0.5(asterisk), 1.5(diamond), 5(triangle), 15(square), 50(X), 150(dot).

Aliasing appears to cause the intensity peaking behavior of the central field. These investigations parameterized this onset of peaking with five methods, which provided guidelines for maximum turbulence strength $\beta_0^2_{\max}$ valid for a given grid size. An irradiance ratio and a Strehl ratio were first used to identify the onset of the peaking. A Gaussian source was propagated at turbulence strengths $\beta_0^2 = [5 \times 10^{-4}, 5 \times 10^{-3}, 5 \times 10^{-2}, 0.15, 0.5, 1.5, 5, 15, 50, 150, 500]$ using 64×64 , 128×128 , 256×256 , 512×512 , and 1024×1024 grids. Ten runs for each case were used to calculate the average irradiance as a function of radius. These irradiance profiles were used to calculate an irradiance ratio, defined as the irradiance at the grid center divided by the irradiance at the maximum grid radius, and also the Strehl ratio, defined as the irradiance at the grid center for the E-field propagated through turbulence divided by the center irradiance for an E-field propagated through zero turbulence. Figure (24) plots the irradiance ratio versus turbulence strength for different grid sizes, and Fig. (25) shows the Strehl ratio versus turbulence strength for different grid sizes.

As turbulence strength increased, diffraction and scattering spread the energy outward and caused the irradiance and Strehl ratios to decrease. Eventually, both ratios reached a minimum and then started increasing because of the alias-induced intensity peaking. This minimum occurred at higher turbulence strengths for larger grid size because the larger grid sizes sampled with a finer mesh and did not significantly alias as soon. Using estimates of

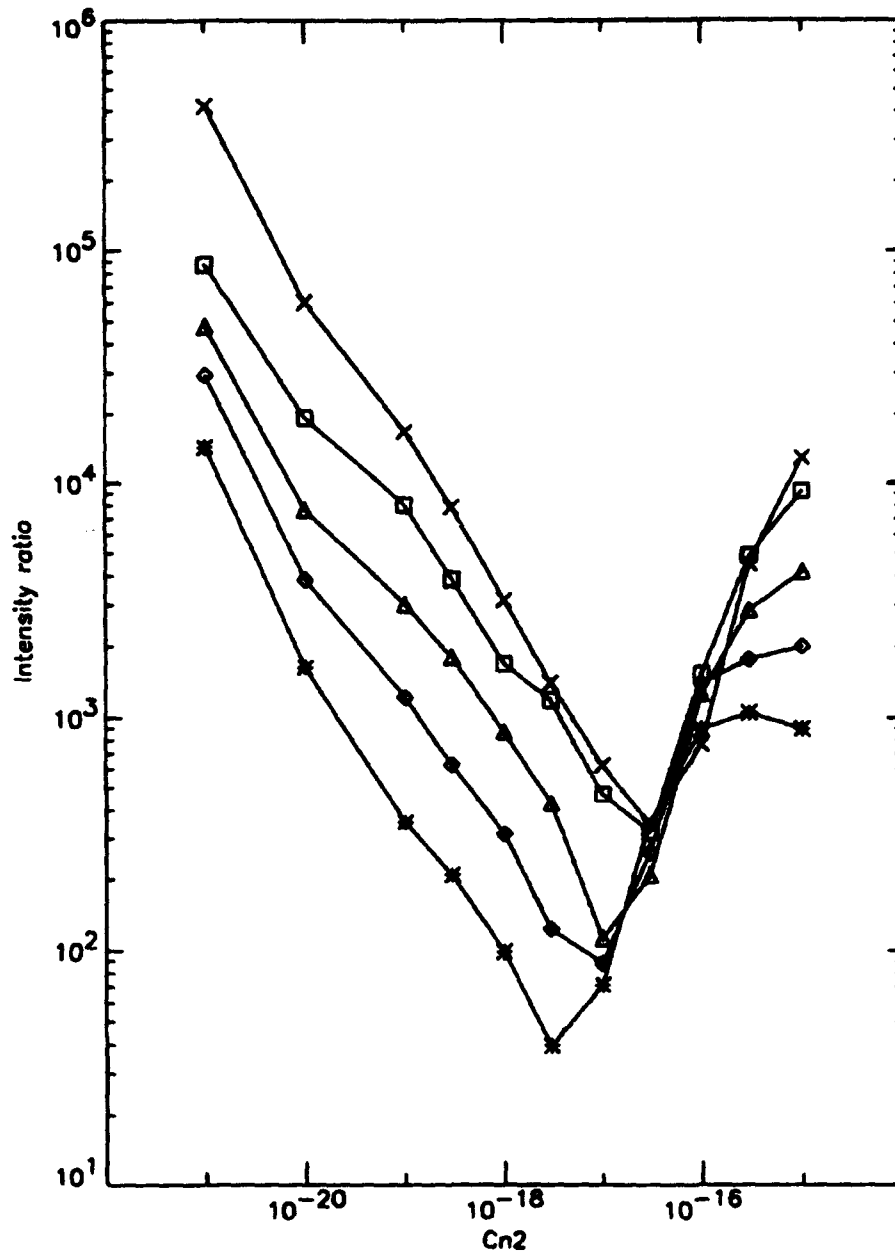


Figure 24 Irradiance ratio versus turbulence strength ($\beta_0^2 = [5 \times 10^{-4}, 5 \times 10^2]$) for grid sizes: 64x64 (asterisks), 128x128 (diamonds), 256x256 (triangles), 512x512 (squares), 1024x1024 (X's).

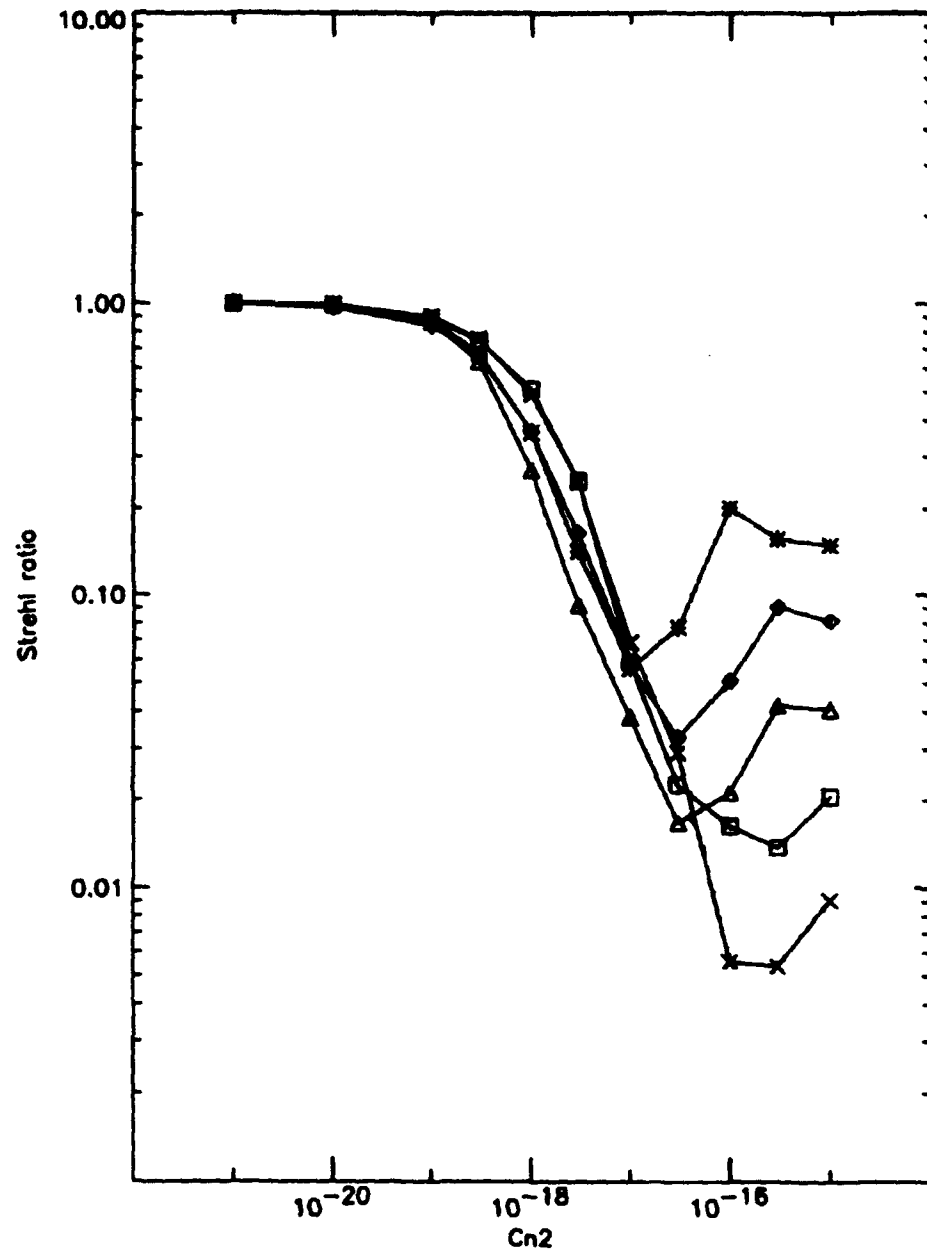


Figure 25 Strehl ratio versus turbulence strength ($\beta_0^2 = [5 \times 10^{-4}, 5 \times 10^2]$) for grid sizes: 64x64 (asterisks), 128x128 (diamonds), 256x256 (triangles), 512x512 (squares), 1024x1024 (X's).

these minima as a guide to the onset of significant aliasing. Fig. (26) plots these β_0^2 values versus grid size from the irradiance and Strehl ratios, along with least squares fits and extrapolations to larger grid sizes.

Martin and Flatté (1988) and others have validated computer simulations for predicting statistical properties such as normalized irradiance variance from the E-field propagated through turbulence. The departure of the computer simulation E-fields and intensities from their known or expected smooth behavior as turbulence increases represents another telltale sign of significant aliasing. Figure (27) shows the normalized irradiance variance calculated from computer simulated E-fields versus β_0^2 using grids of sizes 64x64, 128x128, 256x256, 512x512, and 1024x1024. The irradiance value used for normalization was taken as the average irradiance over the central calculation region. Though this single value normalization is not optimal (see the following section, **F. Additional Simulation Parameters**), it does make the normalized irradiance variance calculation sensitive to the peaking behavior because peaking adds large amounts of unphysical variance. In the Rytov regime ($\beta_0^2 \leq 1.0$), all grids successfully simulated the E-field as indicated by their normalized irradiance variances agreeing with the Rytov-Tatarski theory. In the saturation regime ($\beta_0^2 \geq 1.0$) the normalized irradiance variance saturates and turns downward, eventually approaching unity according to asymptotic theory. Assuming that the 1024x1024 grid provides the most accurate propagation

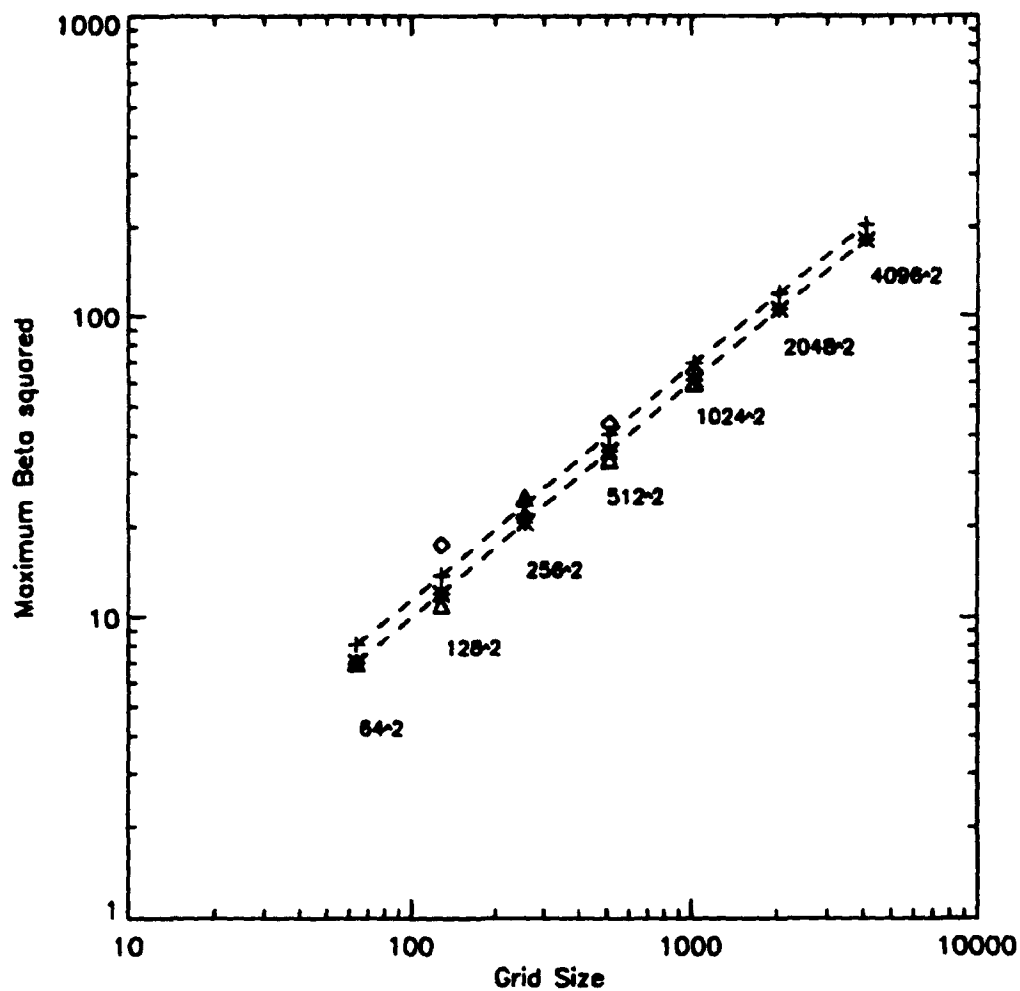


Figure 26 Irradiance ratio (diamonds / pluses) and Strehl ratio (triangles / asterisks) estimates and least squares fits showing maximum turbulence strength versus grid size for valid simulations.

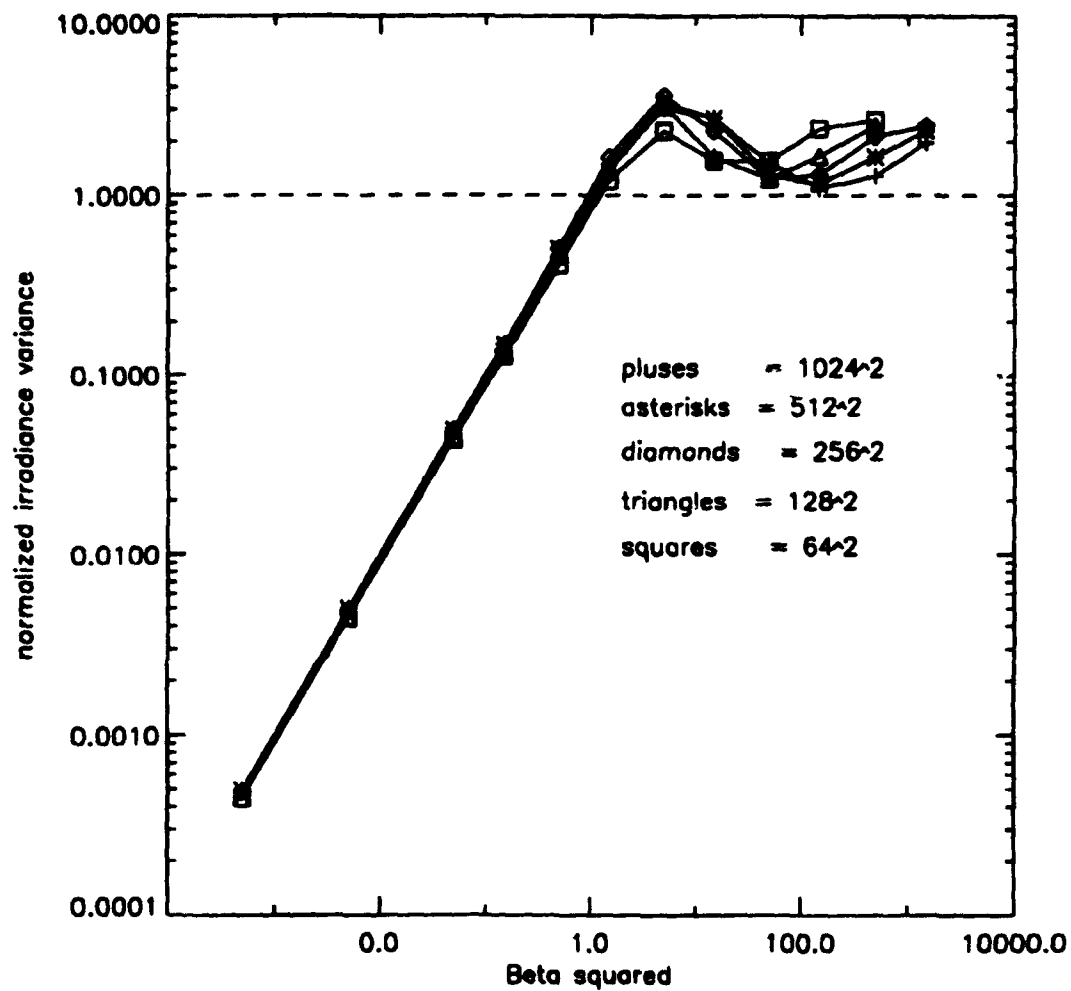


Figure 27 Normalized irradiance variance versus turbulence strength from simulations with different grid sizes.

simulation, the 64x64 grid normalized irradiance variance departs from the 1024x1024 values before the peak was reached, and 128x128 grid normalized irradiance variance departed just beyond the peak. Their meshes were not small enough to adequately sample the E-field, and the resulting aliasing caused peaking that drove up the normalized irradiance variance calculation. The 256x256 grid produced the saturation peak, but soon suffered from significant aliasing. The 512x512 calculations successfully produced the peak but departed from the 1024x1024 predictions before $\beta_0^2 \sim 50$. Judging from these behaviors, the 1024x1024 grid probably remains valid through $\beta_0^2 \sim 50$. All grids eventually showed the normalized irradiance variance anomalously rising for high enough turbulence strength because aliasing produced peaking. Estimates of the maximum β_0^2 values at which the five grid sizes remained valid are plotted, along with a least squares fit extrapolated to larger grid sizes, in Fig. (28).

In a similar manner, the coherence length and the half width at half maximum (HWHM) of the atmospheric MTF predicted using simulations with different grid sizes also show unphysical behavior as aliasing became significant. Figure (29) plots the simulation derived coherence length, normalized by the Kolmogorov turbulence theoretical values, versus turbulence strength measured by β_0^2 . Figure (30) shows the corresponding plot for HWHM. Both show the eventual strong rise in coherence length and HWHM

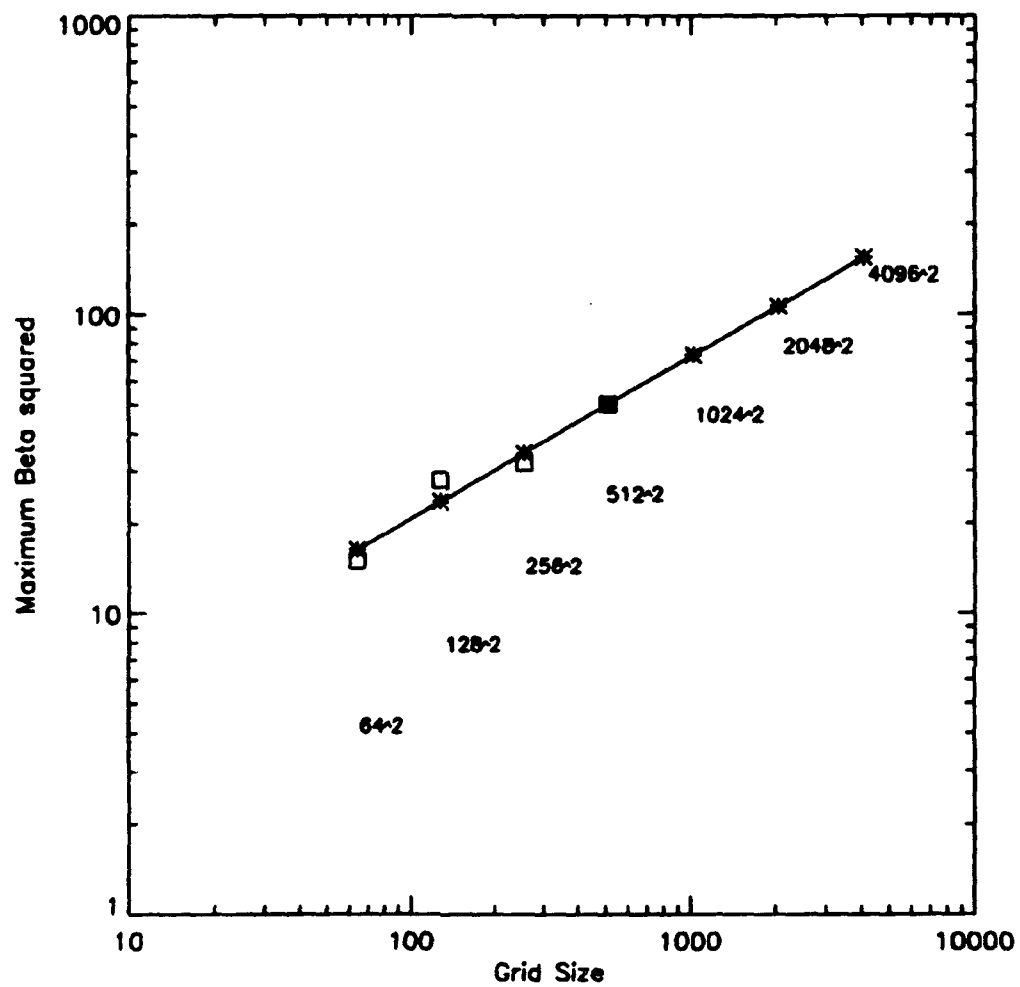


Figure 28 Estimates from normalized irradiance variance of maximum turbulence strength versus grid size for valid simulations.

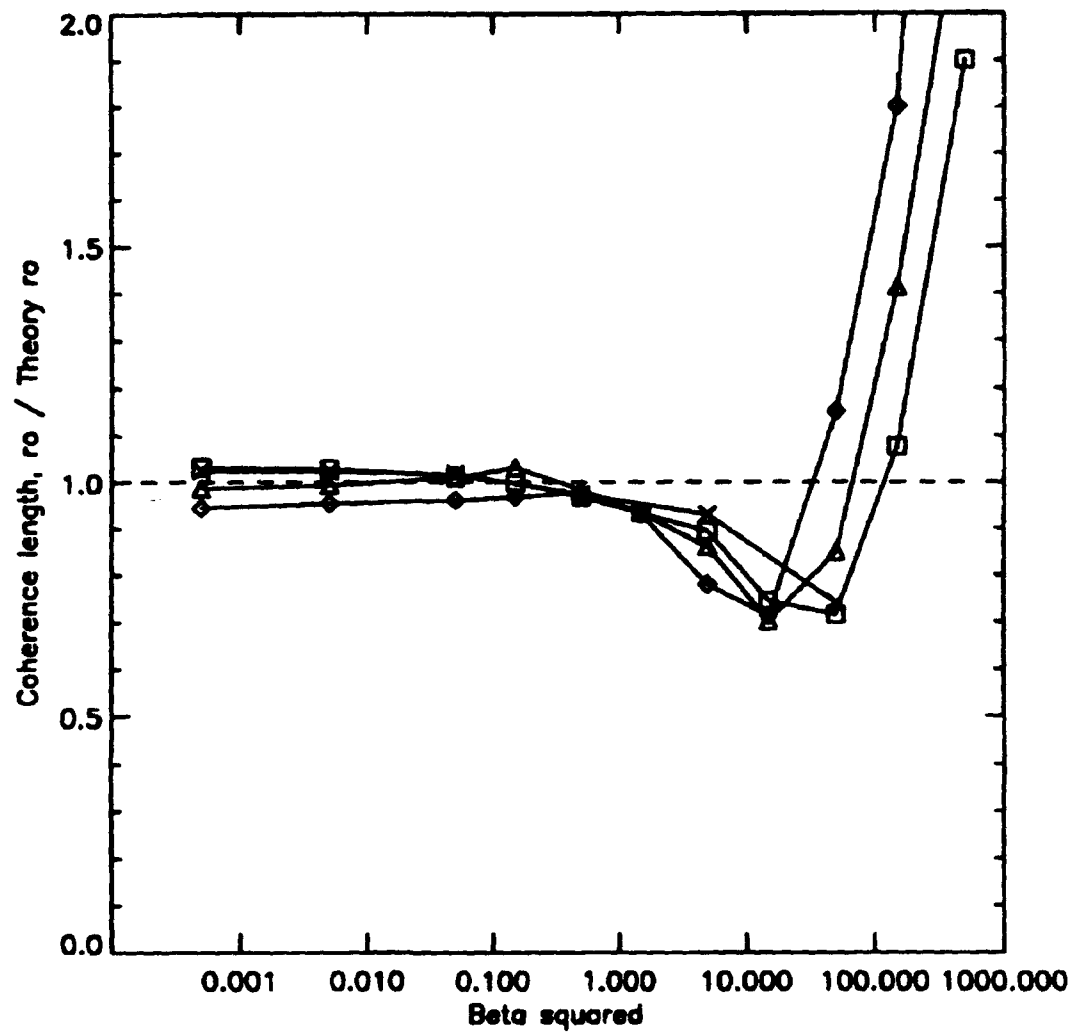


Figure 29 Spherical wave coherence length from simulations versus turbulence strength for grid sizes 128x128 (diamonds), 256x256 (triangles), 512x512 (squares), and 1024x1024 (X's).

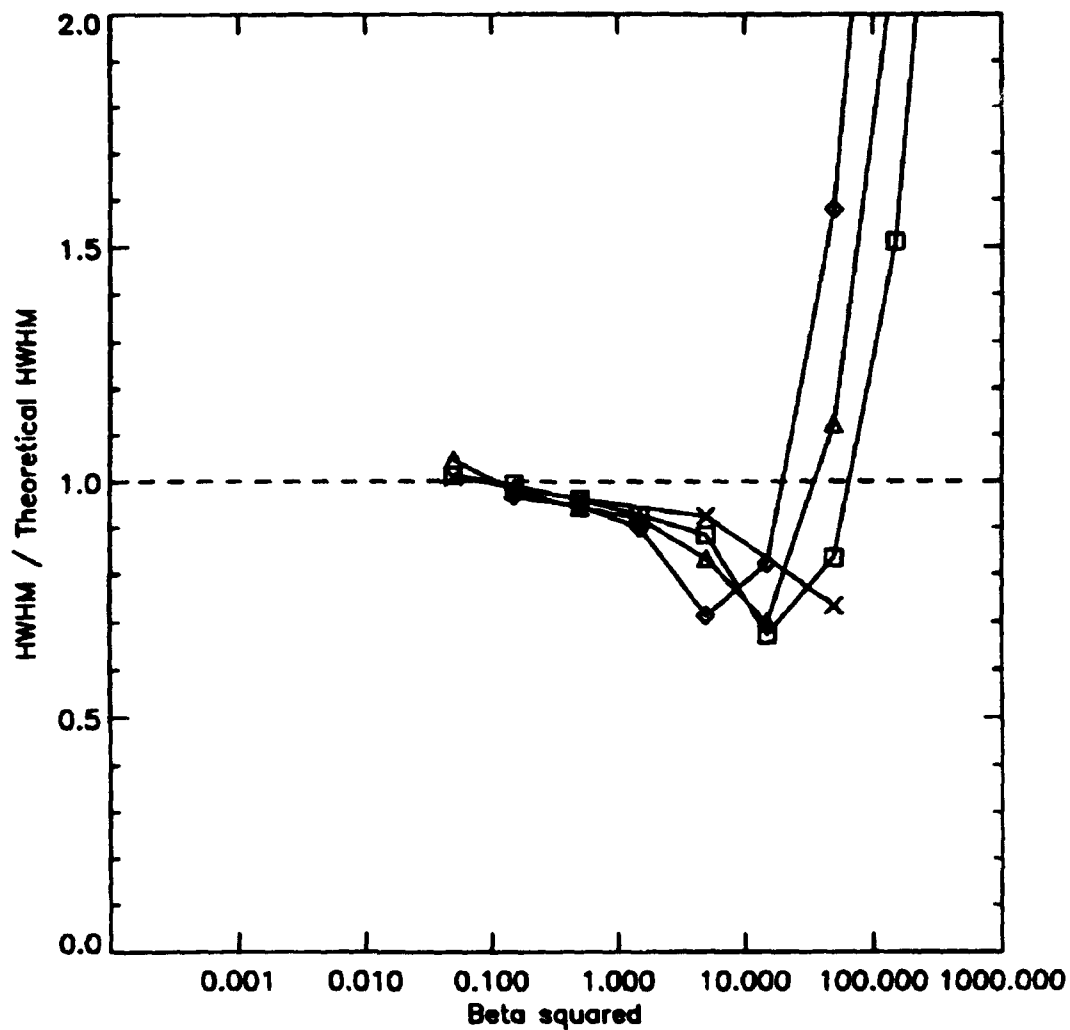


Figure 30 Spherical wave HWHM from simulations versus turbulence strength for grid sizes 128x128 (diamonds), 256x256 (triangles), 512x512 (squares), and 1024x1024 (X's).

compared to theory for strong turbulence when aliasing produces peaking. Estimates of the minima of the plots can be used as another indicator of the turbulence strength at which significant aliasing occurs. Figure (31) plots these points versus grid size, along with a least squares estimate extended to larger grid sizes.

The onset of peaking and departure from expected physical behavior provide symptoms of aliasing but do not indicate the amount of aliasing required to cause them. Determination of the fraction of total field energy that is aliased serves as one parameterization of the amount of aliasing and accomplishes two goals: (1) relate the amount of aliasing occurring to an easily measurable characteristic of the simulation, and (2) determine how much aliasing must occur to invalidate the computer simulation.

First, to parameterize the amount of energy aliased, the same size Gaussian source was applied to 64x64, 128x128, 256x256, and 1024x1024 grids and then propagated through turbulence. The width of the source was chosen so that the Fourier transform had approximately the same width on the final grid and the Gaussian sources on the different grids were normalized to the same energies. Since identical sources were applied in the spatial domain according to the analytical Gaussian formula, the spatial frequency representation of these sources improved as the grid size increased and the mesh became finer. The 1024x1024 grid served as an approximation to infinite

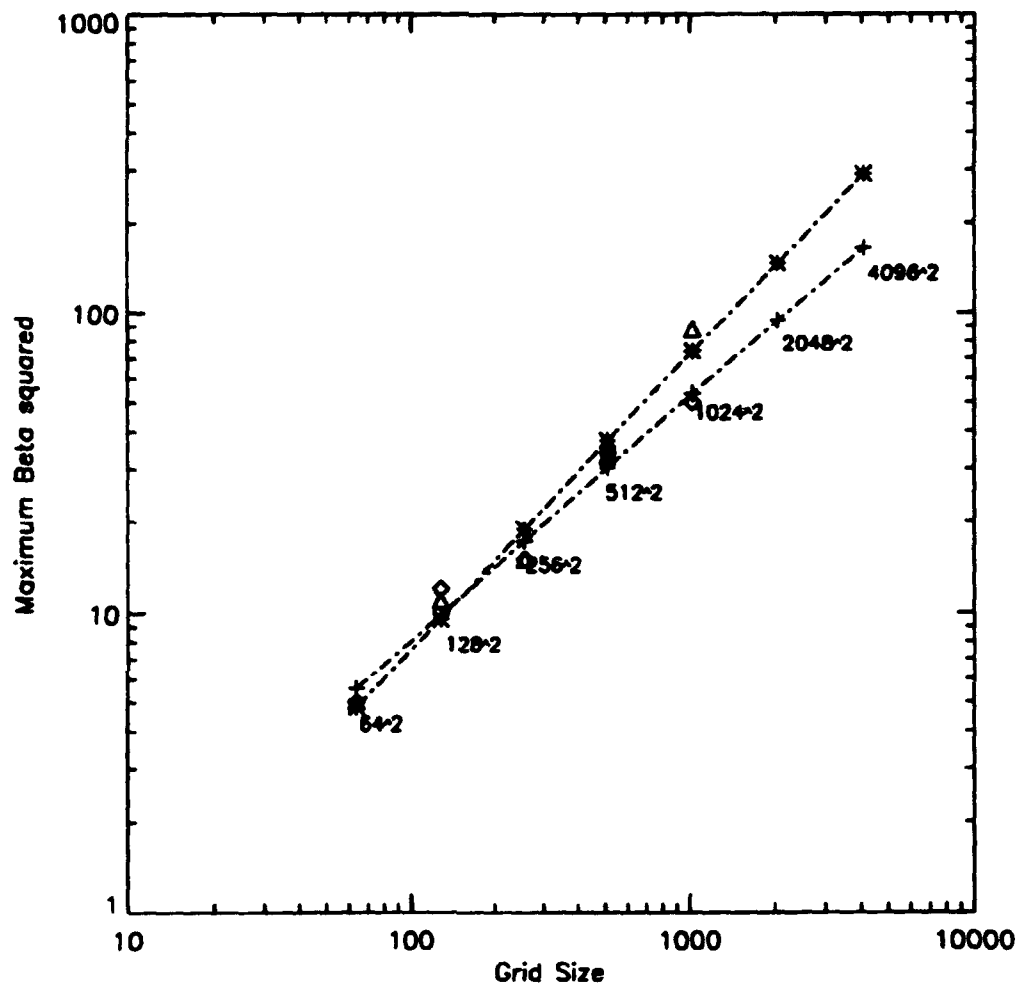


Figure 31 Estimates and least squares fits from spherical wave coherence length (triangles / asterisks) and HWHM (diamonds / pluses) of the maximum turbulence strength versus grid size for valid simulations.

grid size. Due to its larger extent and finer mesh, the 1024x1024 spatial frequency representation of the Gaussians contained spectral energy in the region outside the spectral footprints of the smaller grids, as Fig. (32) illustrates. Since each grid started with the same total energy, the fraction of spectral energy in the 1024x1024 grid lying outside the spectral footprints of the smaller grids approximated the amount of energy aliased in the smaller grids. This process was then applied to propagations of the Gaussian beams through increasing strengths of turbulence, well into the significant aliasing regions for

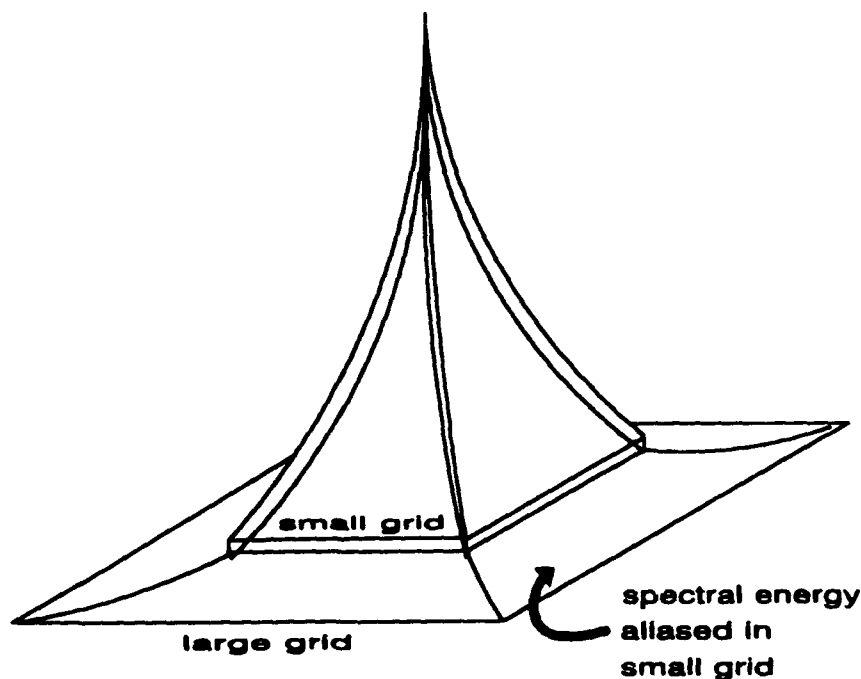


Figure 32 Illustration of the spectral representations of the Gaussian beam with different grid sizes.

the smaller grids. This method provided estimates of the fraction of energy aliased versus turbulence strength for the three smaller grids.

To achieve the first goal of relating the amount of aliasing to a measurable simulation parameter, the average radial power spectral density of the propagated E-field was calculated for each turbulence strength with the smaller grids. Using these profiles, a spectral ratio was calculated, defined as the ratio of the power spectral density at the grid center to the power spectral density at the maximum grid radius. Figure (33) plots these results, and also includes spectral ratios for 512x512 and 1024x1024 grids. Using the information on fraction of energy aliased versus β_0^2 and spectral ratio versus β_0^2 , the turbulence strength β_0^2 served as the connection between fraction of energy aliased and the measurable simulation parameter of spectral ratio. Figure (34) shows plots of these spectral ratios versus corresponding fraction of energy aliased. The log-log plot behavior proved approximately linear over the range 0.001 to 0.1 , which appears very useful because 0.1% of energy aliased probably does not affect the simulation results significantly while more than 10% of energy aliased probably does.

Using the data points of Fig. (34) and performing a linear least squares fit to the logarithms

$$\log_{10}(R) = B \log_{10}(FR) + \log_{10}A, \quad (110)$$

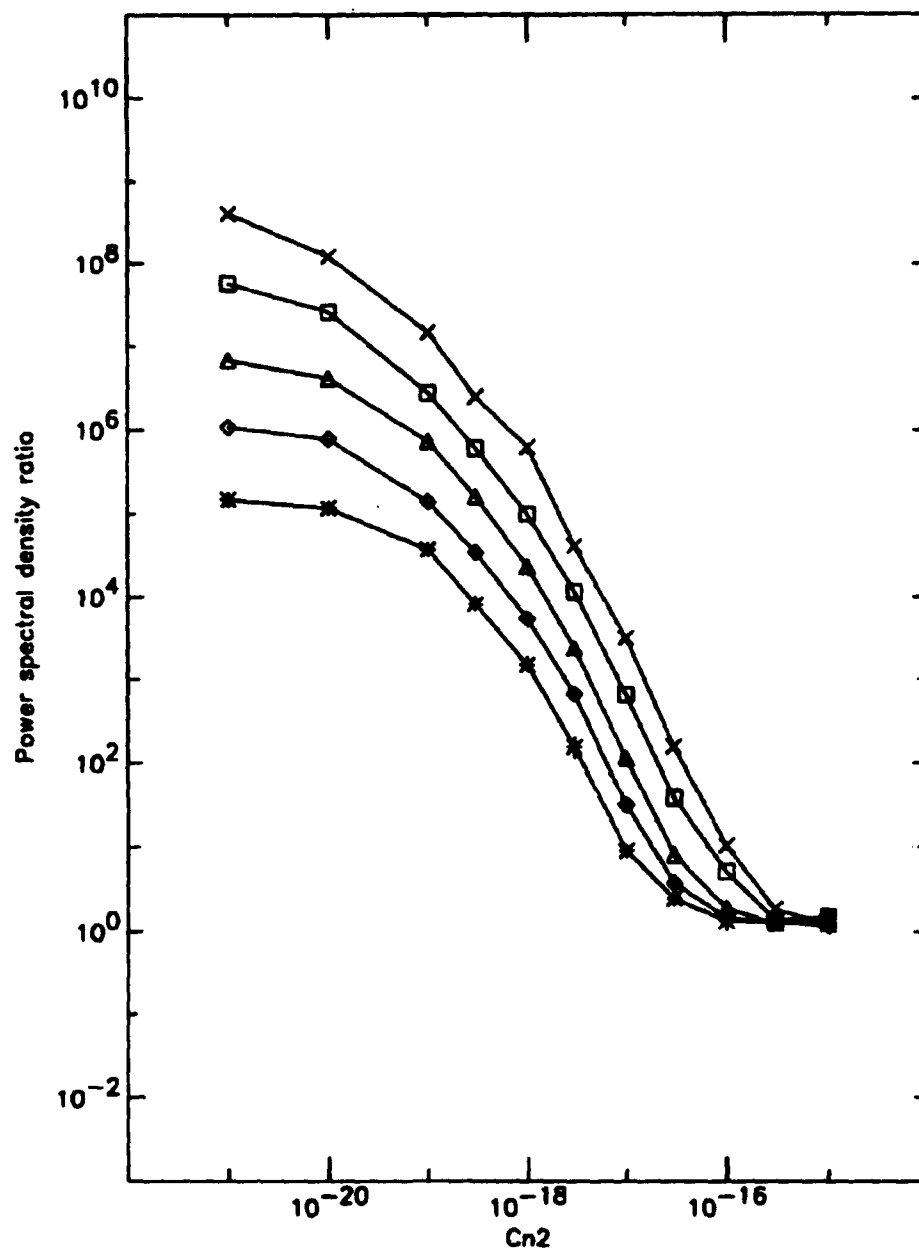


Figure 33 Spectral ratio versus turbulence strength for grid sizes 64x64 (asterisks), 128x128 (diamonds), 256x256 (triangles), 512x512 (squares), 1024x1024 (X's).

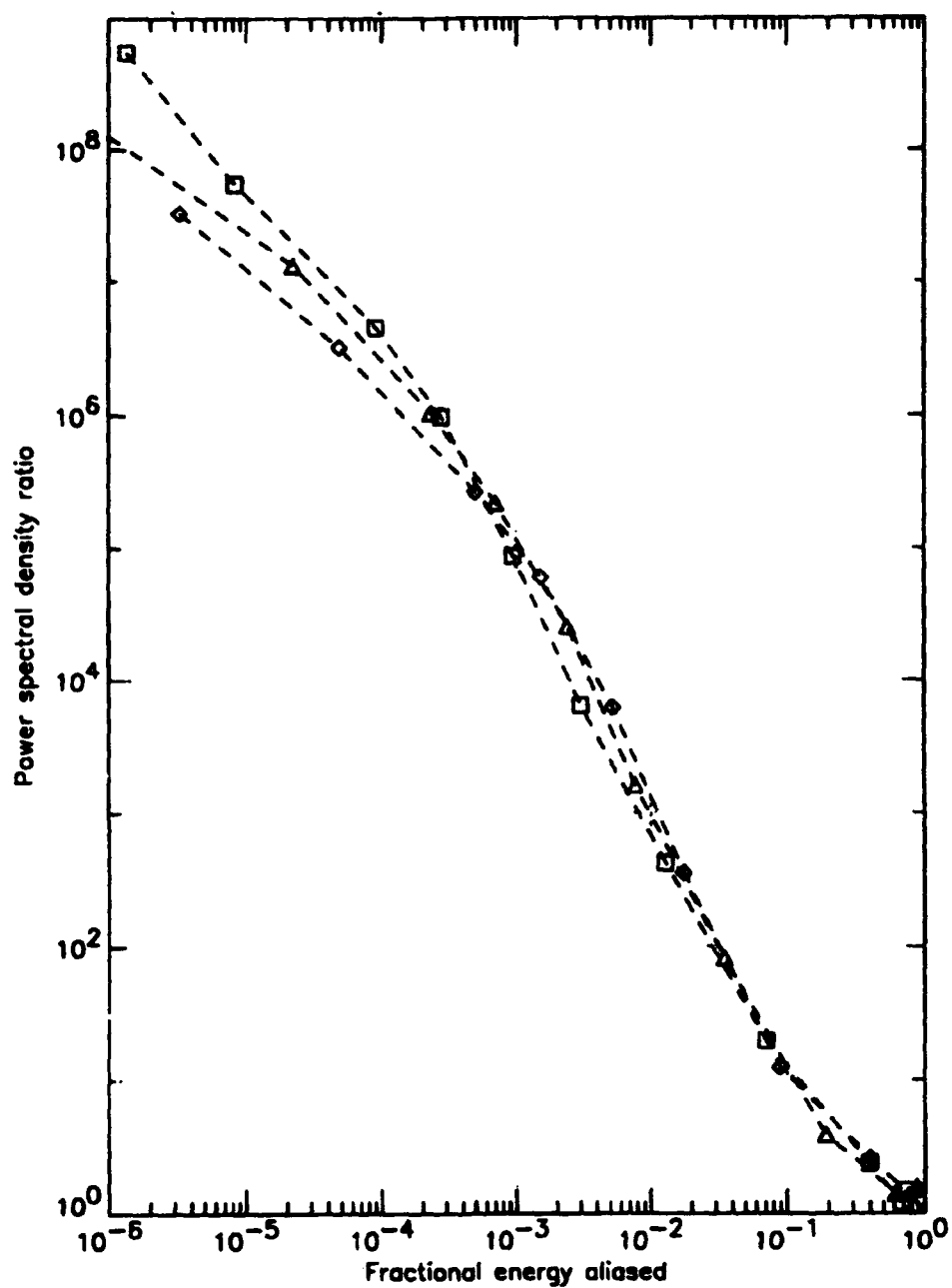


Figure 34 Power spectral density ratio versus fraction of energy aliased for Gaussian source; grid sizes: 64x64 (diamonds), 128x128 (triangles), 256x256 (squares).

or equivalently,

$$R = 10^A (FR)^B, \quad (111)$$

where R refers to spectral ratio and FR refers to fraction of energy aliased, gives $A = -1.1 \pm 0.1$, $B = -2.1 \pm 0.1$. Substituting the A and B values into Eq. (111) and rearranging,

$$FR = \frac{1}{\sqrt{10 \cdot R}}. \quad (112)$$

This equation achieves the first goal of relating the fraction of energy aliased to a measurable quantity from the simulation.

However, Eq. (112) should be used with caution because it appears to be specific to the narrow Gaussian source used to derive it. Figure (35) shows the same calculations carried out for a source that was the Fourier transform of an aperture of radius equal to 3/4 of the 64x64 grid radius (i.e. Airy-type source). The linear region did not appear, though the plot matched the Gaussian source plot when the fraction of energy aliased was greater than 0.1. The differences arise from the different spectral representations of the propagated E-fields. The abrupt, cylinder-shaped irradiance patterns start with more energy at higher spatial frequencies in the spectral domain than the Gaussian patterns and thus never get below 0.001 fraction of energy aliased even at very low turbulence strengths and high power spectral ratios.

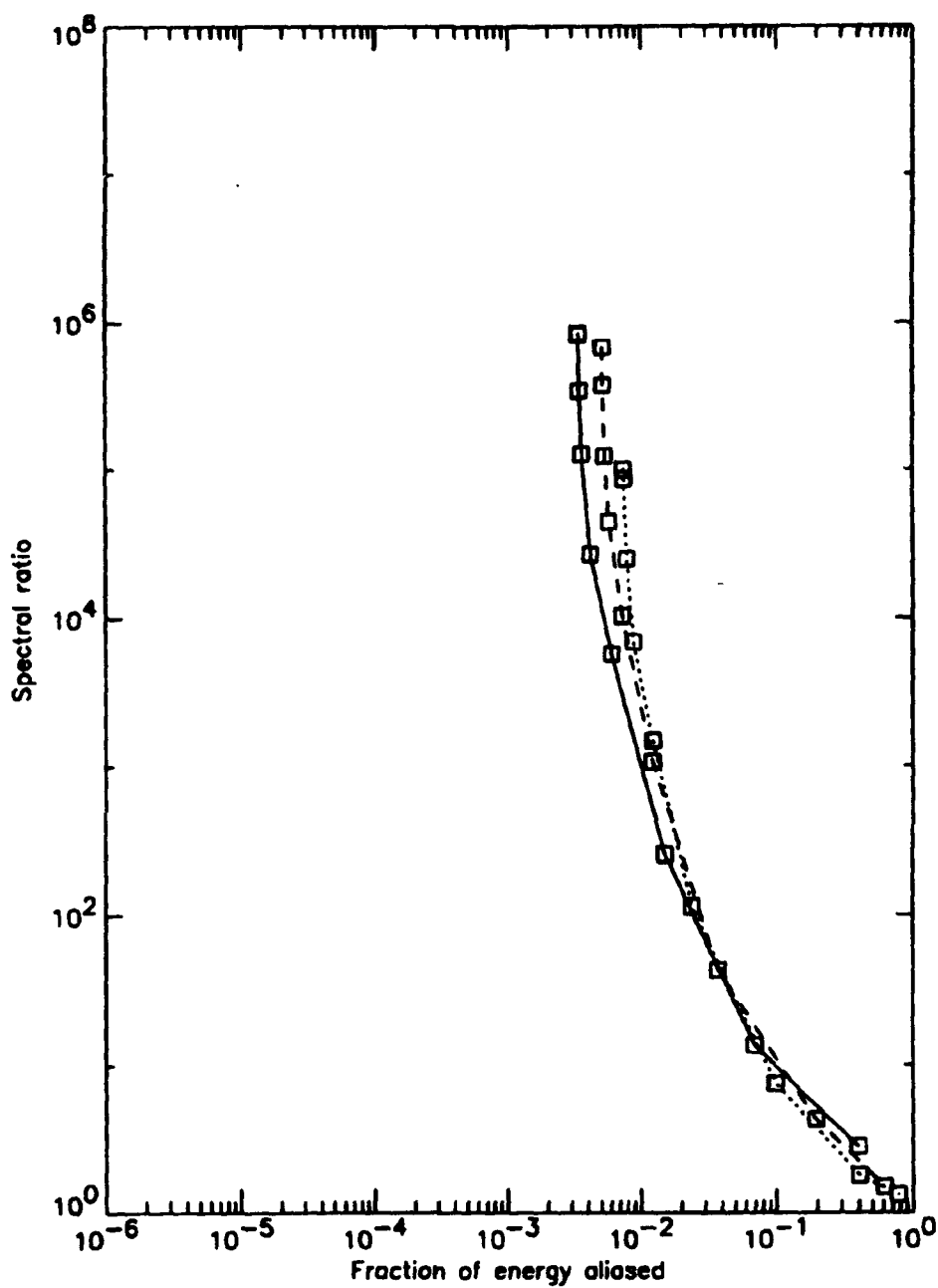


Figure 35 Power spectral density ratio versus fraction of energy aliased for Airy-type source; grid sizes: 64x64 (dotted line), 128x128 (dashed line), 256x256 (solid line).

The second goal of determining the amount of aliasing that invalidates the simulation used the fraction of spectral energy aliased to generate another guideline for maximum strength of turbulence for a given grid size where the maximum fraction of energy allowed to be aliased in a simulation was 10%. Equation (112) predicts a spectral ratio of approximately 10 for 10% of energy aliased. Linearly interpolation between the data points of Fig. (33) provided estimates of the turbulence strengths C_n^2 (thus β_0^2) that gave a spectral ratio = 10, for 10% energy aliased, for the five grid sizes. Figure (36) plots these values and a least squares fit extended to larger grid sizes. The least squares fit as a function of grid size N was

$$\log_{10}\beta_0^2 = 0.9 \log_{10}(N) - 0.9, \quad (113)$$

or,

$$\beta_0^2 = 0.1 \ N^{0.9}. \quad (114)$$

The fraction of energy aliased also provided estimates of maximum β_0^2 for the Airy-type source. Figure (37) plots the fraction of energy aliased versus turbulence strength for the 64x64, 128x128, and 256x256 grids. Again choosing 10% energy aliased and using linear interpolation yields data points for the solid line in Fig. (36) that shows the maximum turbulence strengths obtained from Fig. (37). For 10% energy aliased, the predictions for maximum

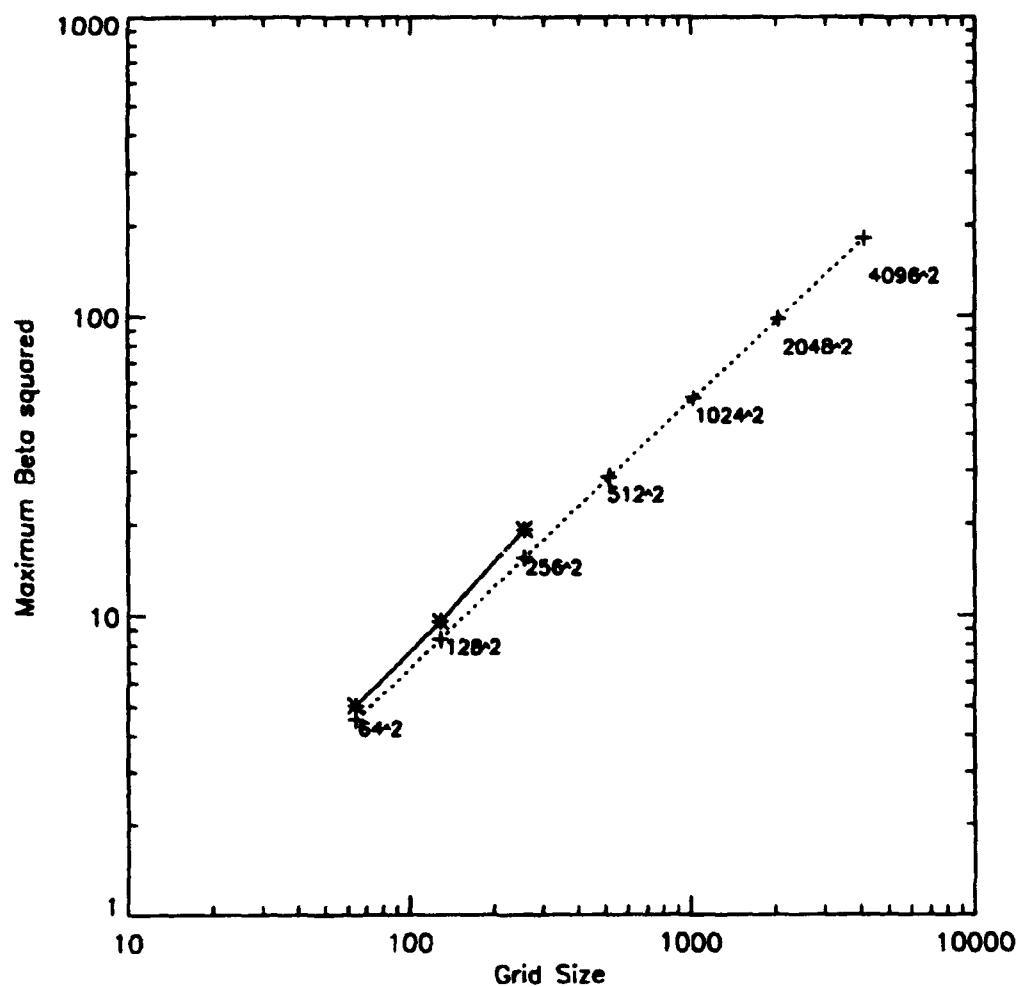


Figure 36 Least squares fit (pluses, dotted line) of maximum beta squared versus grid size for a Gaussian source that had 10% energy aliased and for an Airy-type source (asterisks, solid line).

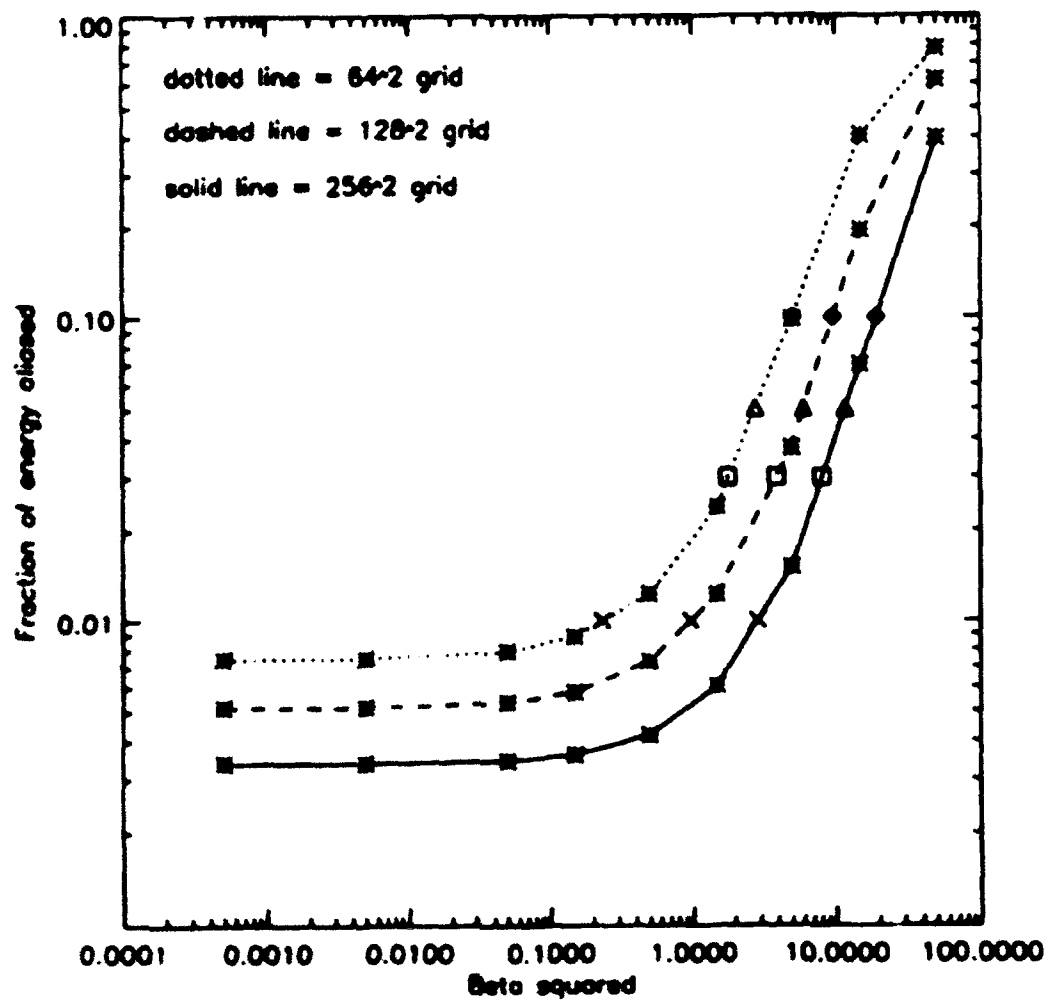


Figure 37 Fraction of energy aliased versus turbulence strength with an Airy-type source for grid sizes 64x64, 128x128, and 256x256.

β_0^2 for the three smaller grids using the Airy-type source agree within ~20% with the predictions from the Gaussian source. Lower values of fractional energy aliased do not provide such agreement.

Another measure of maximum turbulence strength involved the coherence length and grid size. Aliasing occurs because the E-field fluctuates significantly over scale sizes smaller than the grid element size. Intuitively, some connection should exist between coherence length of the E-field and the onset of significant aliasing. Fried's coherence length r_0 represents the distance over which the atmospheric MTF falls to $\exp(-3.44) = 0.032$ (Fried, 1966, p. 1380-1383). Equation (38), which relates β_0^2 to C_n^2 , and Eq. (66), which relates r_0 to C_n^2 , and Eq. (92), which relates the grid element size Δx to N , when combined, yield the turbulence strength corresponding to a given grid size for a specific number (γ) of Δx 's per r_0 .

$$\beta_0^2 = \begin{cases} 0.677 \gamma^{-4/3} N^{4/3} & \text{, spherical wave} \\ 0.629 \gamma^{-4/3} N^{4/3} & \text{, plane wave} \end{cases} \quad (115)$$

Figure (38) plots these β_0^2 for $\gamma = 2, 2.5$, and 3 for the spherical wave case. The 10% aliased energy line, indicated by plus symbols, lies nearest the 2.5 Δx per r_0 line. The E-field must be spatially sampled with 2.5 Δx per r_0 to limit the fraction of energy aliased to 10%, analogous to the Nyquist criterion of two samples per cycle.

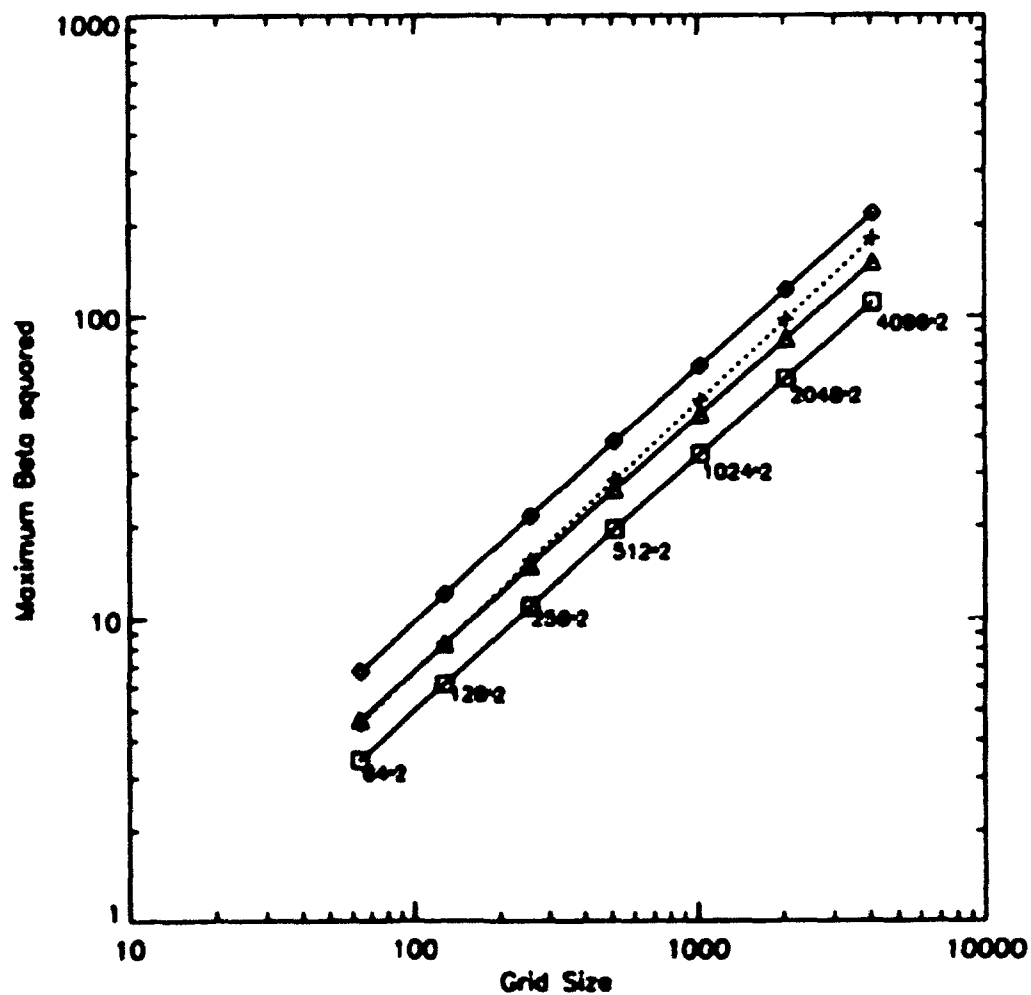


Figure 38 Theoretical spherical wave coherence length versus grid size requiring 2 (diamonds), 2.5 (triangles), or 3 (squares) grid elements per coherence length. 10% aliased energy line (pluses) also plotted for reference.

Figure (39) provides a combined plot of the maximum turbulence strength β_0^2 that produced valid E-fields for a given grid size from all of the foregoing measures: density ratio, Strehl ratio, normalized irradiance variance, coherence length, HWHM, fraction of energy aliased, and coherence length ($\gamma = 2.5$). Most estimates lie within a factor of 2 of each other, and the 10% energy aliased line (dotted/pluses) given by Eq. (114) represents an approximate lower bound to those estimates based upon onset of significant aliasing.

Figure (39) provided three significant conclusions: (1) the computer simulations remained valid until approximately 10% of the energy became aliased (achieving the first goal), (2) using the 10% energy aliased line, the maximum turbulence strength β_0^2 for valid E-fields for a grid size N was

$$\beta_{0_{\max}}^2 = 0.1 N^{0.9}, \quad (116)$$

and (3) maximum valid turbulence strength corresponded to approximately 2.5 grid elements per r_0 (based on proximity of the $\gamma = 2.5$ line to the 10% energy aliased line). Conclusion (2) implies that doubling the grid size N (with grid element size Δx given by Eq. (92)) slightly less than doubles the maximum β_0^2 that the grid can simulate, and that these investigations, which use a 1024x1024 grid, should be valid up to $\beta_{0_{\max}}^2 \sim 50$.

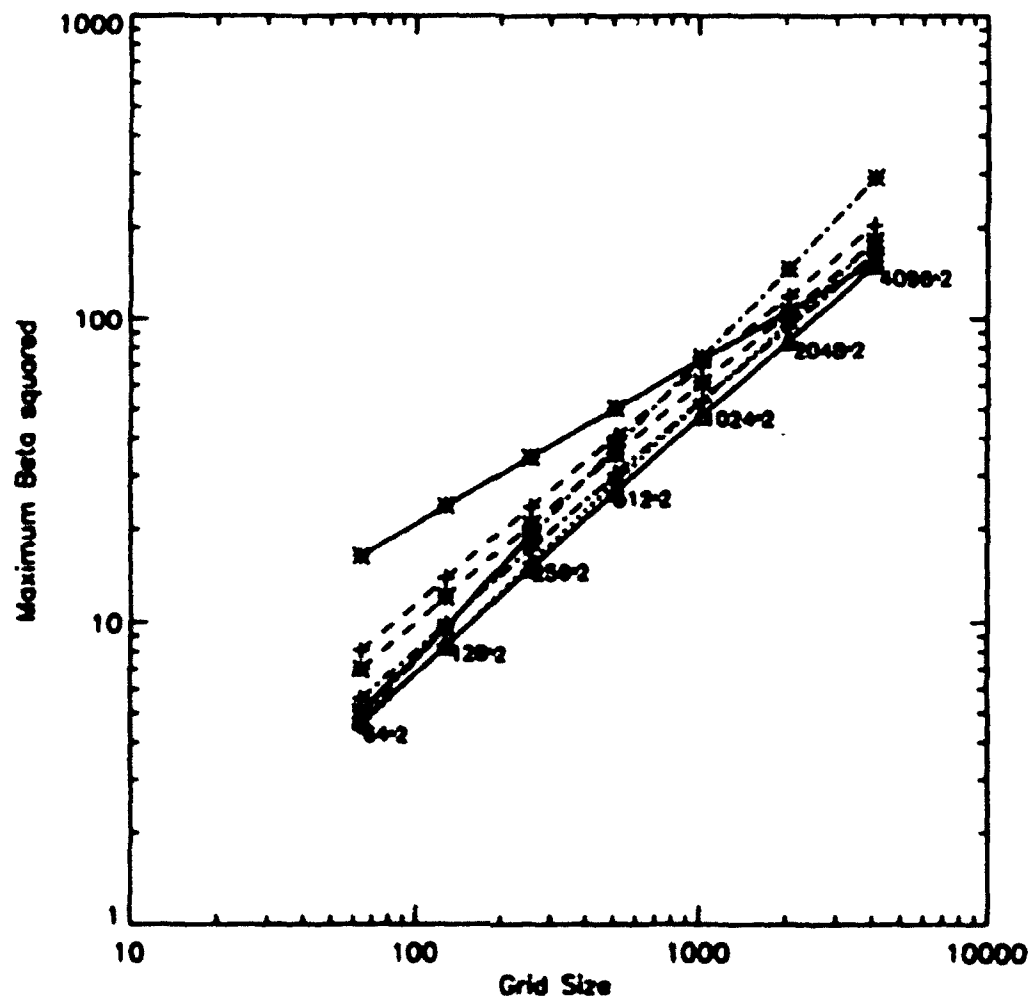


Figure 39 Combined plot of estimates of maximum turbulence strength valid for various grid sizes.

F. ADDITIONAL SIMULATION PARAMETERS

Additional aspects of a computer simulation were addressed to ensure validity, including the number of phase screens, the method of normalizing the irradiance variance, the number of realizations (propagations through turbulence) required for representative statistics, and the width of the final irradiance field on the grid.

The number of phase screens must be large enough to represent the turbulence accurately along the path and produce proper irradiance and coherence statistics. Martin and Flatté (1988) determined the number of phase screens by requiring that the variance due to propagation over the distance Δz between phase screens be less than 1/10 the variance from the total propagation over the distance L

$$\sigma_I^2(\Delta z) < 0.1 \sigma_I^2(L), \quad (117)$$

and additionally that the value of the variance from one step be less than 0.1

$$\sigma_I^2(\Delta z) < 0.1 \quad . \quad (118)$$

With these considerations, they generally used 20 phase screens for their simulations.

These investigations examined the irradiance and coherence statistics directly and concluded that approximately 30 phase screens were required to

ensure simulation validity. Figure (40) shows a set of spherical wave normalized irradiance variance simulations for a 512x512 grid, $\beta_0^2 = 1.5$, and the number of phase screens varying between 2, 4, 8, 16, 32, and 64. Assuming the 64 phase screen case most closely approximated physical reality, as few as 8 phase screens gave a normalized irradiance variance within ~10% of this value. By 32 phase screens, the normalized irradiance variance had stabilized to within 2% of the 64 phase screen value. For this level of turbulence that lies at the beginning of the saturation regime, the addition of phase screens beyond 32 did not affect the normalized irradiance variance significantly.

Figure (41) shows the normalized irradiance variance from propagations with 2, 4, 8, 16, 32, and 64 phase screens at $\beta_0^2 = 50$ with a 1024x1024 grid and 30 realizations for each number of phase screens. This strength of turbulence represents the limit of simulation validity with the 1024x1024 grid and lies in the strong saturation regime beyond the normalized irradiance variance peak. In this case, 32 phase screens provided a normalized irradiance variance within 3% of the 64 phase screen case, and the 16 phase screen value was within approximately 10%. Because 32 phase screens appears to increase the accuracy of the simulation by ~5% compared to 16 phase screens, the larger number of phase screens was chosen for these investigations.

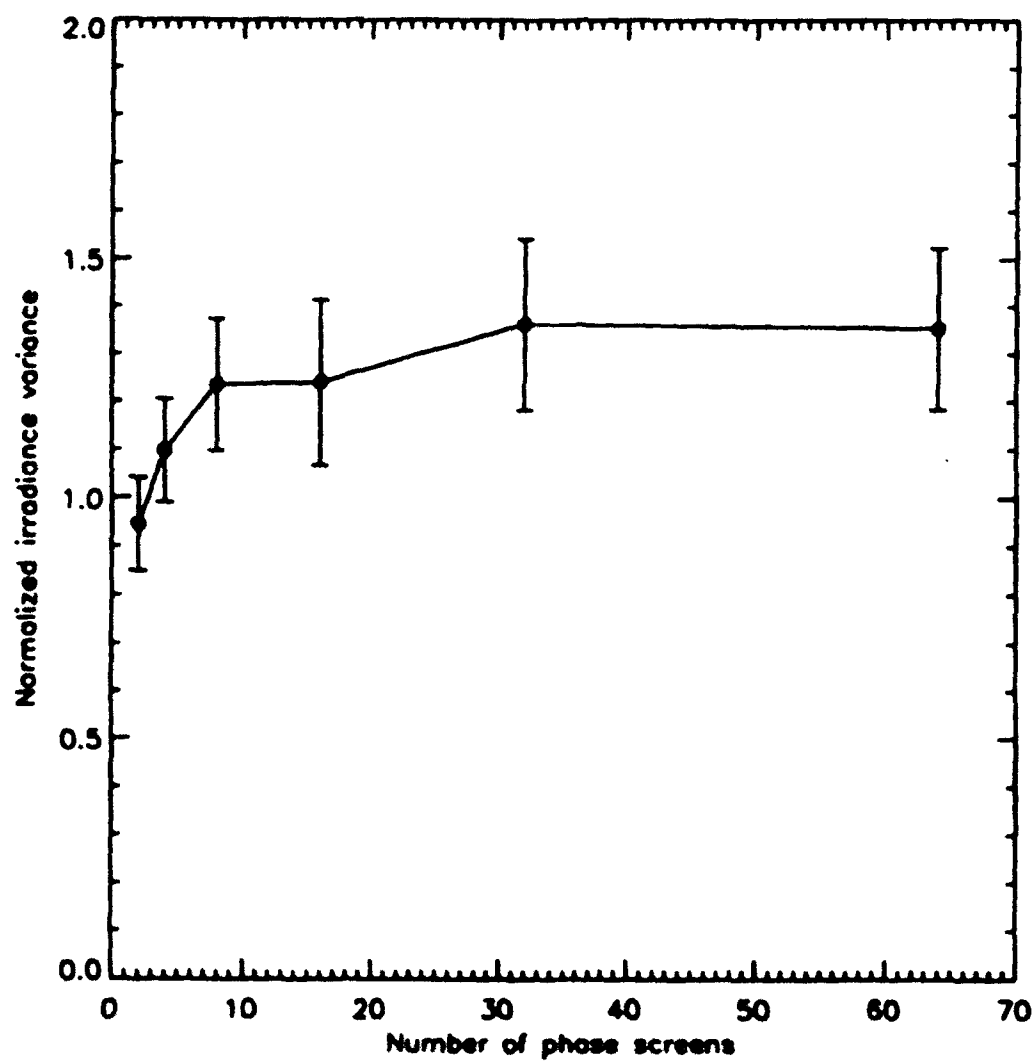


Figure 40 Normalized irradiance variance as a function of number of phase screens for turbulence strength $\beta_0^2 = 1.5$.

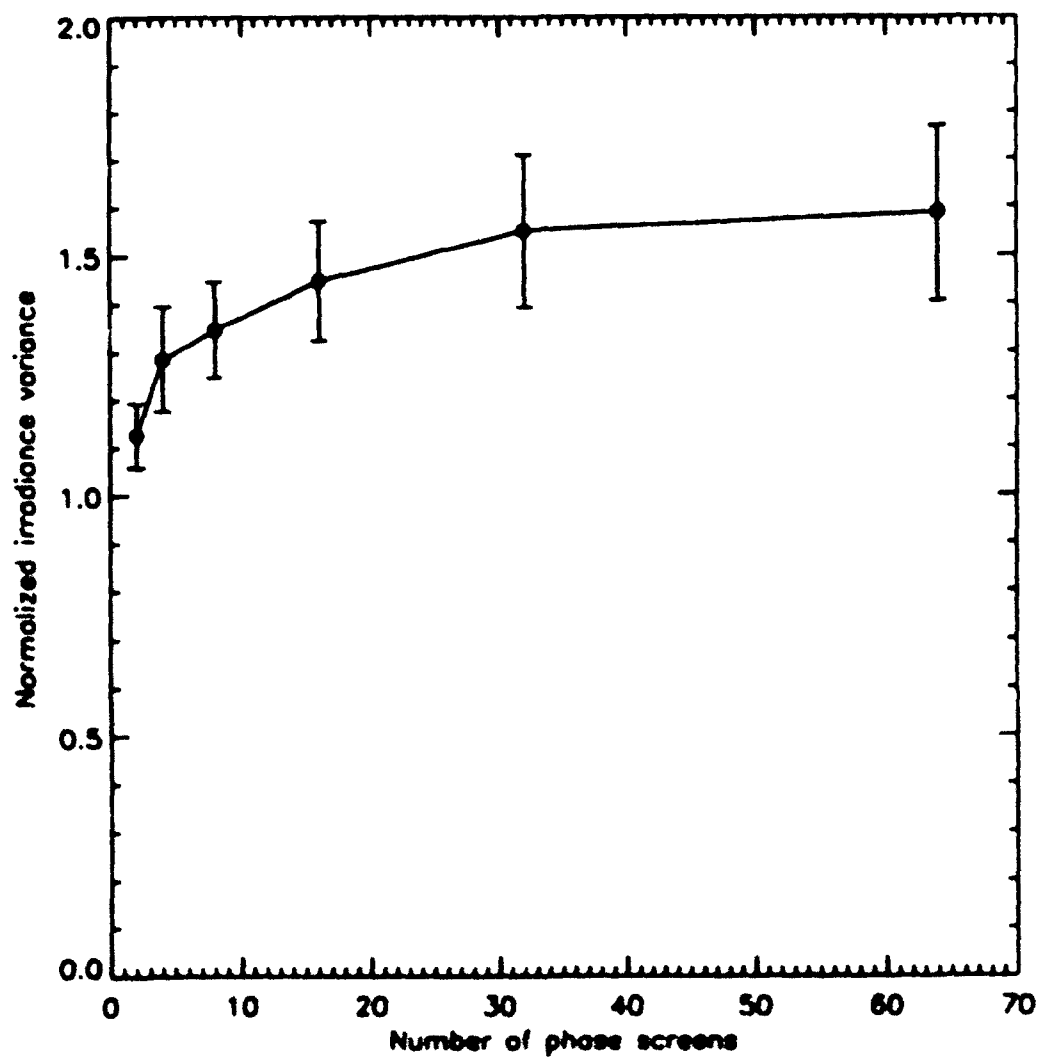


Figure 41 Normalized irradiance variance as a function of number of phase screens for turbulence strength $\beta_0^2 = 50$.

Using the same 1024x1024 realizations, the coherence length r_0 and HWHM of the atmospheric MTF were calculated for the 2, 4, 8, 16, 32, and 64 phase screen cases. Figure (42) plots the results. For coherence length, the 32 phase screen value was within approximately 1% of the 64 phase screen value, and the 16 phase screen value was within approximately 3%. The HWHM plot indicates 2% and 3% agreements for 32 and 16 phase screens, respectively. The 32 phase screens used for these investigations thus proved sufficient for coherence length and HWHM calculations.

The method of normalizing the irradiance variance and the number of realizations to use for statistical accuracy proved to be interrelated considerations. Turbulence diffracts and scatters energy outward from an initially well-defined beam. For the Airy-type source used in these investigations, the average irradiance over the central portion of the final propagated field was uniform for zero turbulence but became a function of radial distance from the propagation axis when turbulence was present. This was an artifact of the computer simulation that had to use a beam spatially confined to the grid rather than a true spherical (or plane) wave. Figure (43) shows irradiance versus radial distance r for the central 256x256 portion of 1024x1024 grid simulations, averaged over 30 realizations, and using a turbulence strength $\beta_0^2 = 50$. The average radial irradiance varies by approximately 15% over the width of this calculation region. This radial

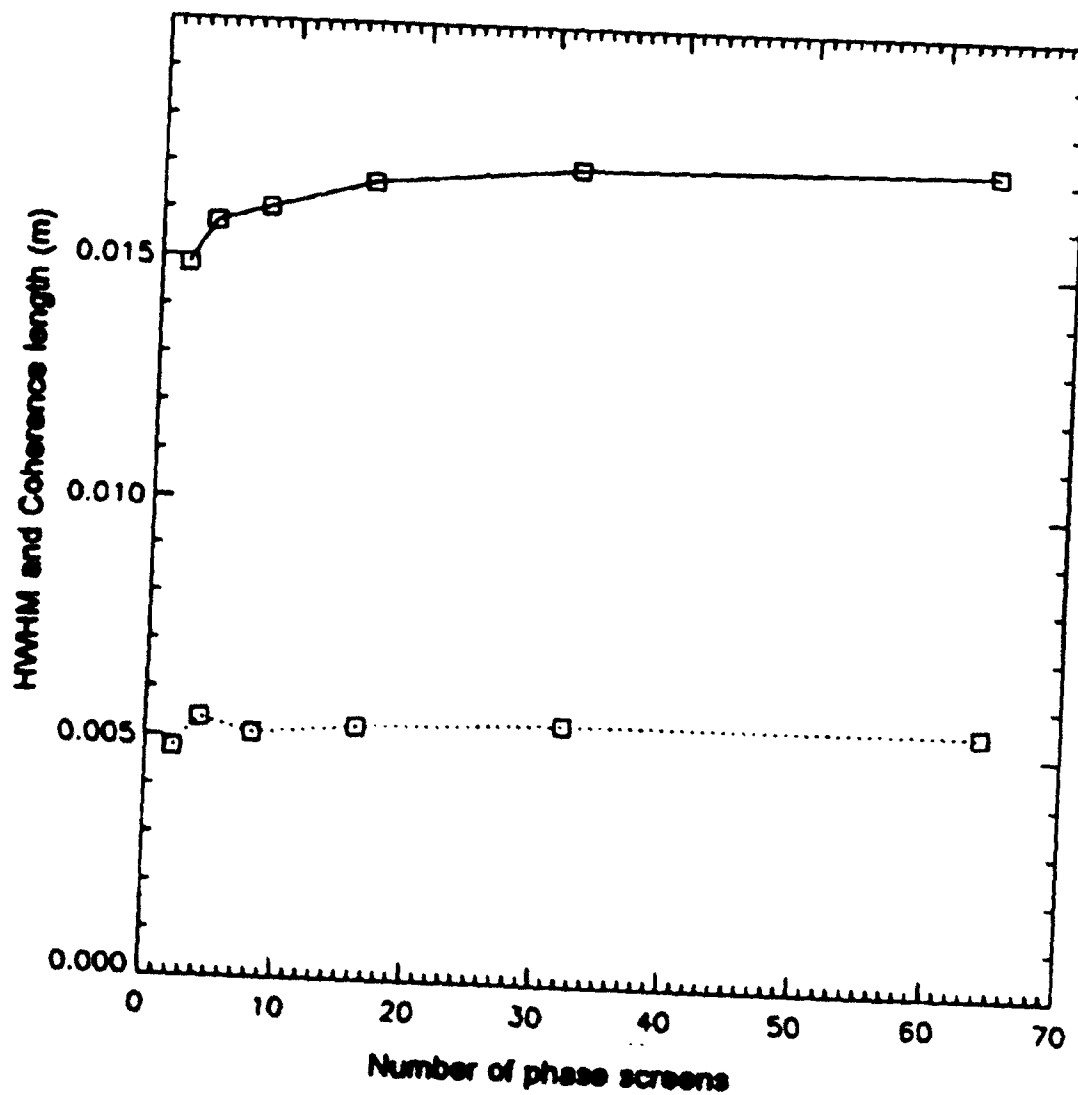


Figure 42 Coherence length (top) and HWHM (bottom) as a function of different numbers of phase screens at turbulence strength $\beta_0^2 = 50$.

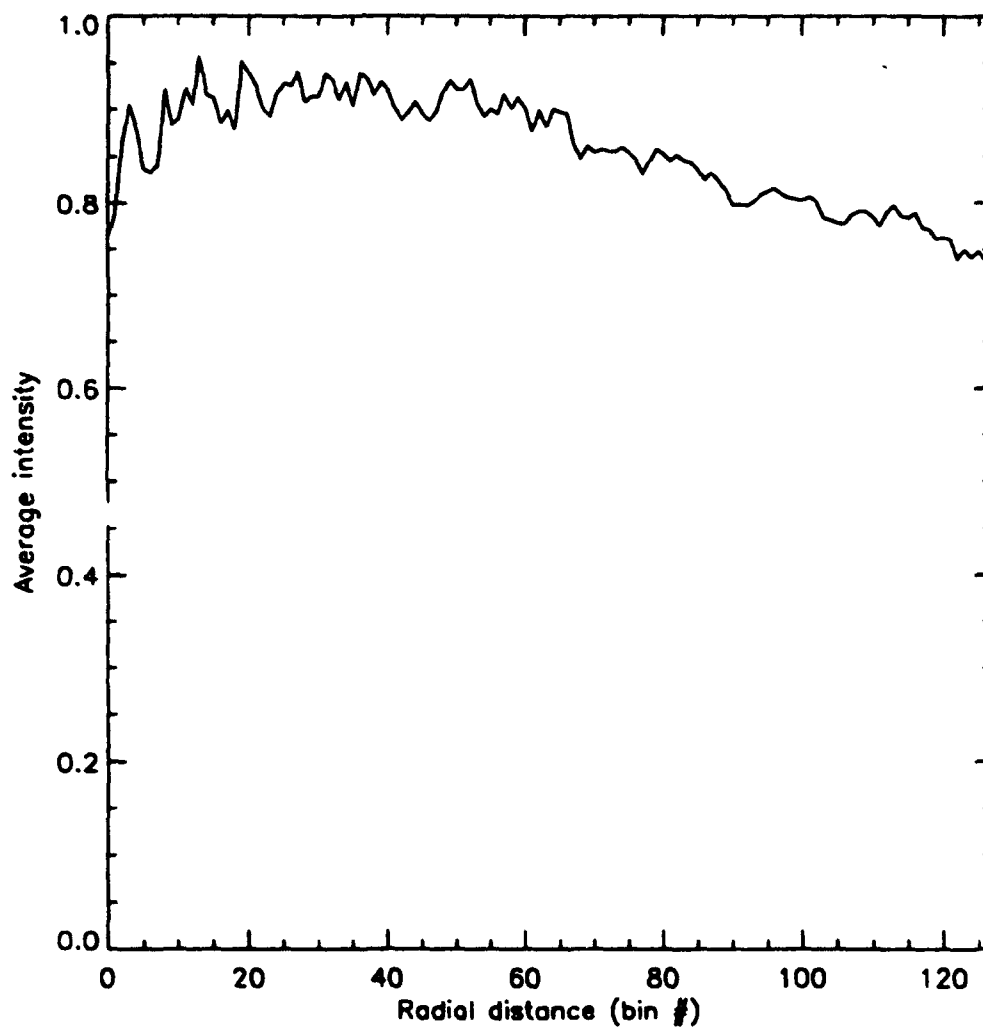


Figure 43 Average irradiance as a function of radius for central 256x256 portion of 1024x1024 grid simulation.

variation of the average irradiance was removed from the normalized irradiance variance calculations with a method similar to that of Flatté, Wang, and Martin (1993). The calculation region was restricted to half the radius of the zero turbulence irradiance pattern, which was previously chosen as one half the grid radius. With the 1024x1024 grid, this calculation region equaled the largest radius circle inside the central 256x256 portion of the grid. This disk was further divided into concentric rings and the irradiance in each ring averaged over all 30 realizations. These average ring irradiances were used to normalize the irradiance variance calculated from each field. Smaller ring size (thus more rings) reduced the number of points in the irradiance average for each ring and required more realizations to ensure a sufficient number of points to yield a stable average irradiance.

The ring width had to be small enough to compensate for the radial variation in average irradiance and the number of realizations large enough to provide enough points to yield representative average values. To determine suitable ring width and number of realizations, 50 1024x1024 realizations with the Airy-type source at $\beta_0^2 = 1.5, 3, 10, \text{ and } 20$ were run and the normalized irradiance variances calculated using ring widths of 128, 32, 8, 4, 2, and 1 grid elements, Δx , and with number of realizations in the average equal to 1, 5, 10, 15, ..., 50. Figure (44) plots the results for the $\beta_0^2 = 10$ set. The pluses line corresponds to 1 ring of width 128 Δx (i.e. the whole calculation region) and a

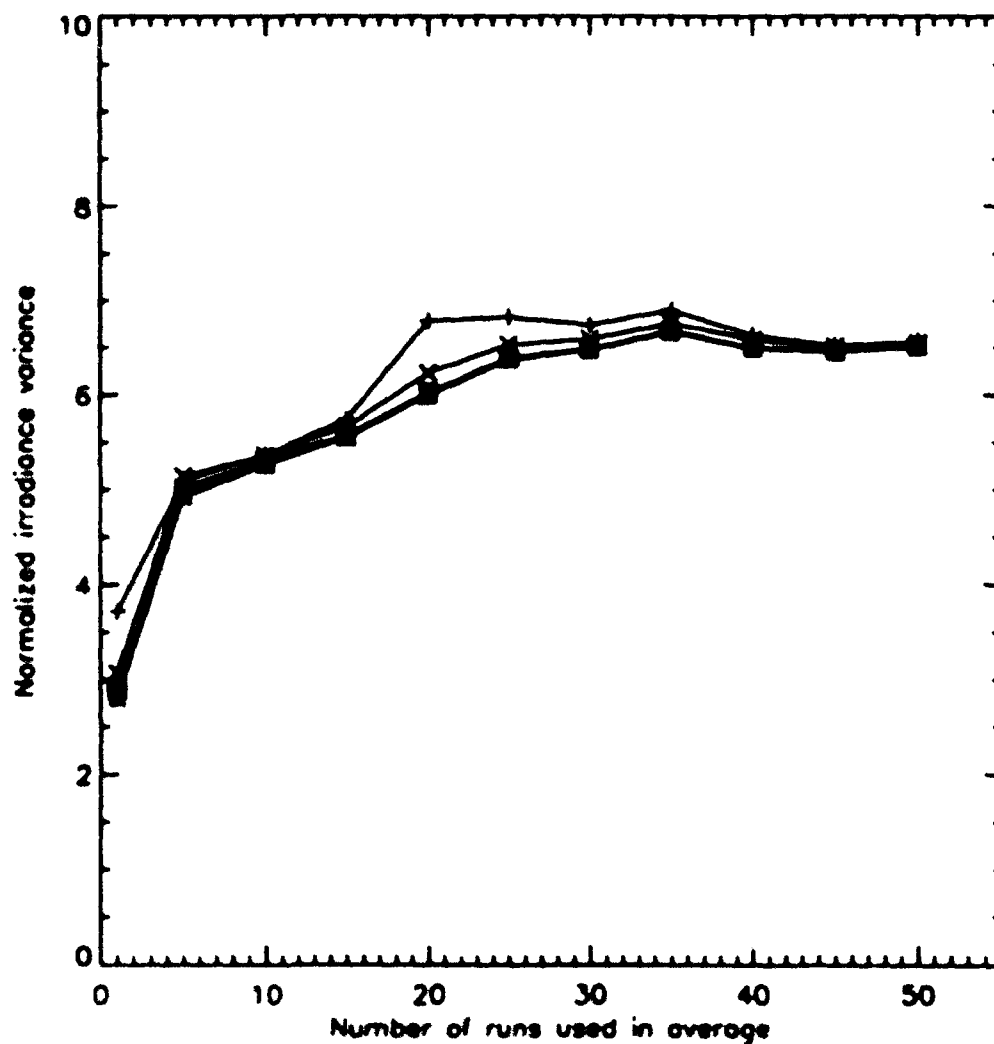


Figure 44 Normalized irradiance variance versus number of realizations used in average; ring widths = 128 (pluses), 32 (X's), 8 (squares), 4 (diamonds), 2 (triangles), 1 (asterisks) Δ 's.

stable normalized irradiance value was achieved using about 20 realizations. However, a single ring does not compensate for the radial variation in average irradiance and can thus give erroneous normalized irradiance values (for the same reason, it becomes sensitive to the peaking behavior from significant aliasing). The X line represents the division of the disk into 4 rings of width $32 \Delta x$ and required ~25 realizations in the average to give a stable normalized irradiance variance. Smaller ring widths (lines with squares, diamonds, triangles, and asterisks lines) all showed similar behavior and required ~ 30 runs to reach a stable average normalized irradiance variance. The $\beta_0^2 = 1.5, 3,$ and 20 runs all provided similar results. A similar $\beta_0^2 = 10$ series with a Gaussian source required a minimum of 8 rings ($16 \Delta x$ each) and 30 realizations to achieve stable average normalized irradiance variances. Consequently, these investigations used 30 realizations as a guideline for valid simulation, and chose a ring width of four grid elements to allow the greatest adjustment to real variations in average radial intensity and yet remain computationally efficient. As Fig. (44) shows, insufficient averaging over enough realizations to yield truly representative average values can reduce the normalized irradiance variance by 15 - 30%.

Similarly, stable coherence length values (discussed in section, H. Coherence Length) required averaging over multiple realizations. To determine the number of realizations required in the average, 50 realizations using a

1024x1024 grid were generated for $\beta_0^2 = 3$ and 20 and the central 256x256 portion of the fields again used to calculate the atmospheric MTFs. These individual MTFs were then averaged in groups of 1, 5, 10, 15, ... , 50 before calculating the coherence lengths. Figure (45) shows the resulting coherence lengths, r_0 . (These particular runs used $L = 150$ m and $\lambda = 420$ nm, giving a Fresnel length $= \sqrt{\lambda L / 2 \pi} = 10$ mm and resulting in millimeter-sized coherence lengths.) As few as 5 realizations in the average yielded coherence lengths within 4% of the 50-realization values. These investigations still used 30 realizations in the average because these 30 fields were already available from the normalized irradiance variance calculations.

The irradiance ratio provided an indicator of the appropriate final beam radius to use to avoid excessive scatter of energy off the grid. The maximum β_0^2 for a given grid varies with the final beam radius because larger radii scatter energy off the grid sooner and cause aliasing at lower β_0^2 . To characterize this behavior, 64x64, 128x128, and 256x256 grid simulations were run at turbulence strengths $\beta_0^2 = [5 \times 10^{-4}, 5 \times 10^2]$ for final beam radii of 4/8, 5/8, 6/8, and 7/8 grid radius, and the resulting irradiance ratios (average irradiance at center divided by average irradiance at grid radius) were plotted versus β_0^2 . Figure (46) shows the plot for the 256x256 grid. Again, the minima correspond to the onset of peaking and occur at lower β_0^2 for larger final beam radius. Linear least squares fit of the final beam radii to these β_0^2 values for the minimum

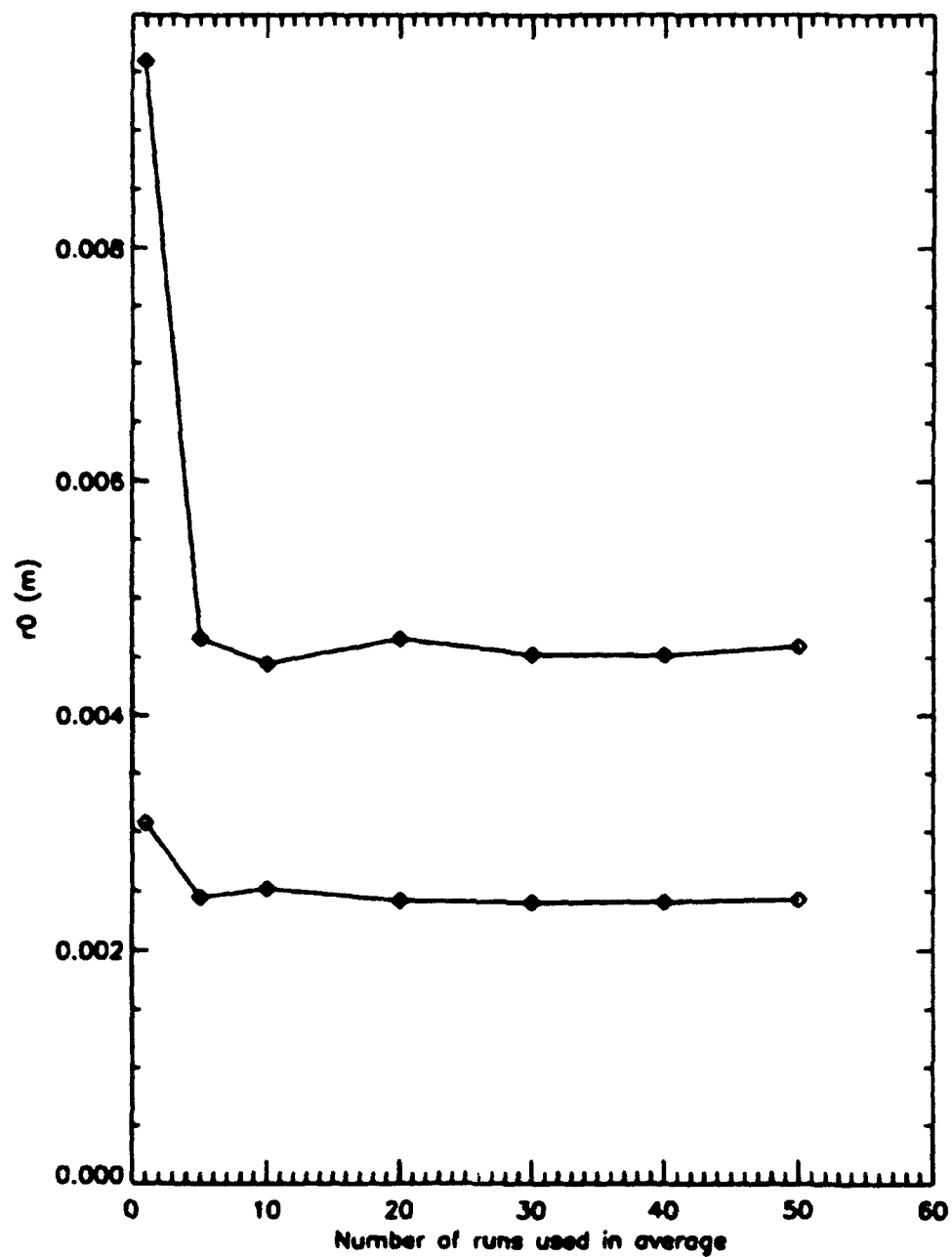


Figure 48 Coherence length as a function of the number of realizations used in the average atmospheric MTF (top: $\beta_0^2 = 3$; bottom: $\beta_0^2 = 20$).

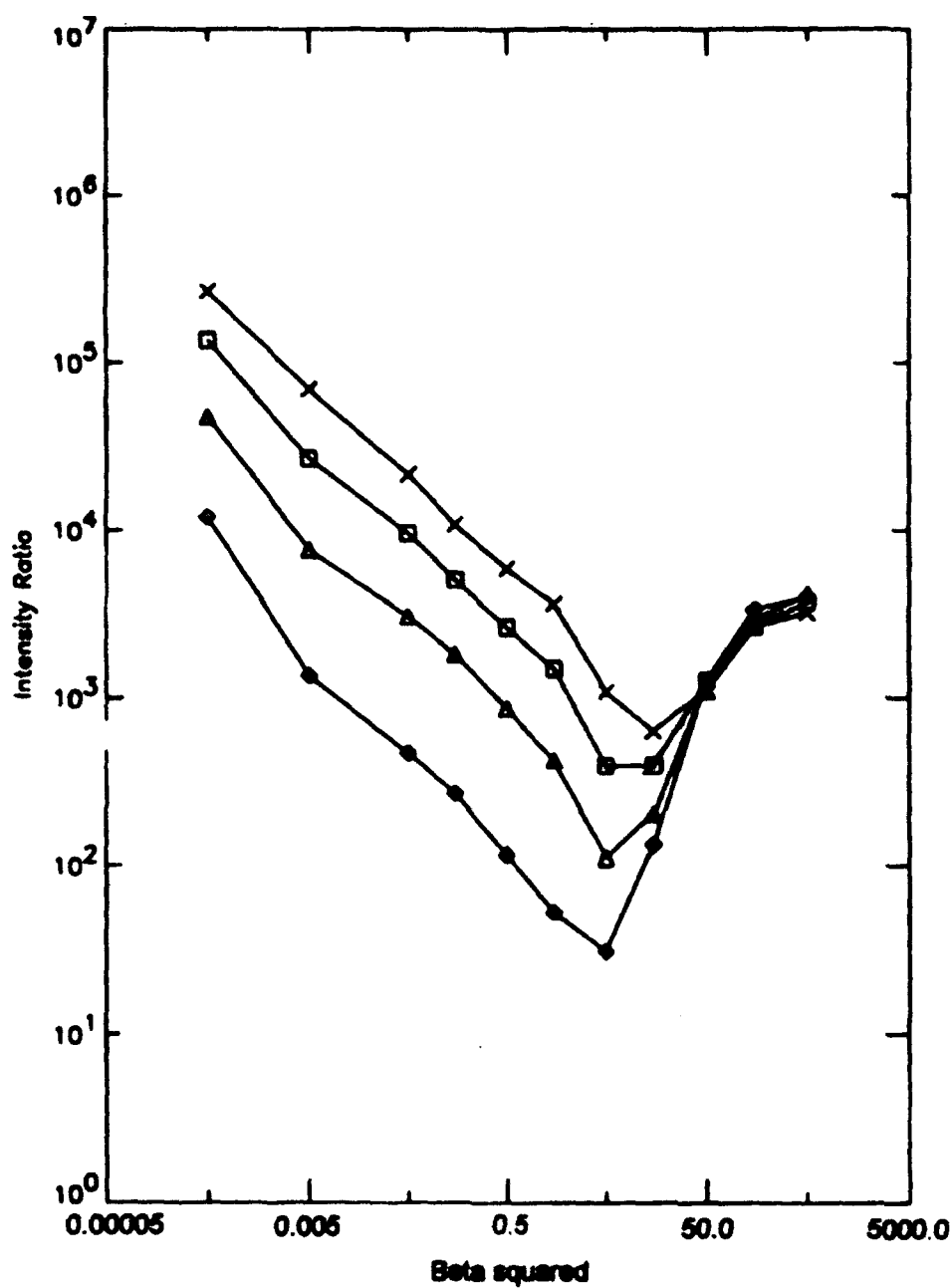


Figure 46 Irradiance ratio versus turbulence strength for final beam radii of 4/8 (X's), 5/8 (squares), 6/8 (triangles) and 7/8 (diamonds) of the 256x256 grid radius.

irradiance ratios indicates that a final beam radius of approximately 0.7 grid radius corresponds with the 10% energy aliased cutoff β_0^2 for the grids. A final beam of 0.7 grid radius provided the largest illuminated central region while still meeting the 10% aliased energy criterion. To be somewhat conservative, these investigations used a final beam radius = 0.5 grid radius to reduce further the energy scattered off the grid.

G. PHASE SCREENS

1. Phase Screen Generation

With the split-step method, the effects of turbulence along the optical path are introduced into the simulation by dividing the optical path into steps and applying a random phase to the complex E-field at each step. As long as the steps are small enough that geometrical optics approximately applies, the E-field only acquires a random phase change as it propagates across each step (Knepp, 1983). Diffraction as the field propagates across many steps then produces the amplitude variations. The random phases are assumed to be Gaussian distributed about a zero mean with variance proportional to the turbulence strength C_n^2 and possessing spatial structure function consistent with the assumed Kolmogorov turbulence and appropriate inner scale. Knepp (1983) and Martin and Flatté (1988) describe the process of generating the phase screen with these characteristics, as discussed below.

The phase screen generation begins in the spatial frequency domain by imposing the proper spatial structure function. An $N \times N$ grid of complex numbers $\Theta_0(\kappa_x, \kappa_y)$ is formed whose real and imaginary parts are each Gaussian distributed random numbers with zero mean and unity standard deviation. This $\Theta_0(\kappa_x, \kappa_y)$ represents the Fourier transform of a grid of uncorrelated Gaussian distributed random numbers $\theta_0(x, y)$ representing phases. The proper spatial structure function corresponding to turbulence statistics is imposed upon the random phases $\theta_0(x, y)$ by applying a filter $A(\kappa_x, \kappa_y)$ to $\Theta_0(\kappa_x, \kappa_y)$

$$\Theta(\kappa_x, \kappa_y) = A(\kappa_x, \kappa_y) \Theta_0(\kappa_x, \kappa_y). \quad (119)$$

Taking the magnitude of both sides of Eq. (119), squaring, assuming that the filter function is real, and then taking expectation values gives

$$\langle |\Theta(\kappa_x, \kappa_y)|^2 \rangle = A^2(\kappa_x, \kappa_y) \langle |\Theta_0(\kappa_x, \kappa_y)|^2 \rangle = A^2(\kappa_x, \kappa_y), \quad (120)$$

where use was made of the fact that the Gaussian random numbers $\Theta_0(\kappa_x, \kappa_y)$ have a variance of 1. The two-dimensional power spectral density of the phase $F_s(\kappa_x, \kappa_y)$ is related to $\Theta(\kappa_x, \kappa_y)$ by (Goodman, 1985)

$$F_s(\kappa_x, \kappa_y) = \langle |\Theta(\kappa_x, \kappa_y)|^2 \rangle (\Delta \kappa)^2, \quad (121)$$

where $\Delta \kappa$ represents the grid element size in the spatial frequency domain.

The Hankel transform of the power spectral density $F_s(\kappa)$ gives the phase structure function $D_s(\rho)$ that characterizes the spatial distribution of the phase fluctuations of the E-field (Tatarski, 1961)

$$D_s(\rho) = \int_{-\infty}^{\infty} [1 - J_0(\kappa \rho)] F_s(\kappa, 0) \kappa d\kappa, \quad (122)$$

where local isotropy has been assumed. Tatarski derived the relation between the two-dimensional power spectral density of phase fluctuations $F_s(\kappa_x, \kappa_y)$ and the three-dimensional spectrum of index of refraction fluctuation, $\Phi_n(\kappa)$,

$$F_s(\kappa, 0) = 2\pi k^2 L \Phi_n(\kappa), \quad (123)$$

where $\kappa = \sqrt{\kappa_x^2 + \kappa_y^2}$. This sequence of steps means that the phase screen can have the proper spatial statistics by starting with the proper spectrum of refractive index fluctuations (hence, the proper structure function).

The spectrum of index of refraction fluctuations assuming Kolmogorov turbulence with inner scale is

$$\Phi_n(\kappa, z) = 0.033 C_n^2(z) \kappa^{-11/3} F(\kappa \ell_0), \quad (124)$$

where $F(\kappa \ell_0)$ gives the inner scale dependence for inner scale ℓ_0 (see Fig. 8).

Substituting Eq. (124) into Eq. (123) gives the power spectral density of phase fluctuations

$$F_s(\kappa, z) = 2\pi k^2 L (0.033) C_n^2(z) \kappa^{-11/3} F(\kappa \ell_0), \quad (125)$$

and using Eq. (121) specifies the proper form for $\Theta(\kappa_x, \kappa_y)$, the corresponding Fourier transform of the random phases

$$\langle |\Theta(\kappa_x, \kappa_y)|^2 \rangle = (\Delta \kappa)^{-2} 2\pi k^2 L (0.033) C_n^2(z) \kappa^{-11/3} F(\kappa \ell_0). \quad (126)$$

Equation (120) then gives the corresponding filter function $A(\kappa_x, \kappa_y)$ to apply to the array of complex numbers $\Theta_0(\kappa_x, \kappa_y)$

$$A(\kappa_x, \kappa_y) = (\Delta\kappa)^{-1} \sqrt{2\pi k^2 L (0.033) C_n^2(z) \kappa^{-11/3} F(\kappa l_0)}. \quad (127)$$

Since the Kolmogorov spectrum ($\propto \kappa^{-11/3}$) has a singularity at $\kappa = 0$, the $\kappa=0$ point in the filter function is set to zero, removing overall piston (i.e. common phase offset over whole screen) from the phase (Cochrane, 1985) and keeping the spectral energy finite. Conversion to a discrete grid representation occurs by substituting $\kappa_x = n_x \Delta\kappa$, $\kappa_y = n_y \Delta\kappa$, $\kappa^2 = (\Delta\kappa)^2 (n_x^2 + n_y^2)$, and $\Delta\kappa = 2\pi/(N \Delta x)$, where Δx is the grid element size in the x-y domain and (n_x, n_y) are grid coordinates. The Fourier transform (FT) of the filtered array of random variables gives the phase screen in the spatial domain

$$\theta(x, y) = 0.0984 k \sqrt{C_n^2(z) L} (N \Delta x)^{5/6} FT \left[\left(\sqrt{n_x^2 + n_y^2} \right)^{-11/6} \Theta_0(n_x, n_y) \right]. \quad (128)$$

Since this phase screen is actually complex-valued, both the real and imaginary parts represent valid random phase screens that were separately applied to the E-field (Cochrane, 1985).

2. Low Spatial Frequency Correction

Due to the finite size of the grid, the above phase screen will not have the proper structure function for separations of the order of the grid width. Low spatial frequency components, especially tilt-type terms, are under-

represented (Cochrane, 1985). These computer simulations incorporate an algorithm formulated by Cochrane that employs an expansion of the phase screen in a Karhunen-Loeve basis set (whose components are mutually orthogonal) to correct some of the low spatial frequency terms.

The general idea of the low frequency correction builds upon the above procedure to generate a phase screen. The low spatial frequency contribution to the phase screen is a superposition of orthogonal low spatial frequency terms, just like the superposition of complex exponential terms by Fourier transform in the phase screen generation process above. The strength of each low spatial frequency term is a Gaussian random variable with an appropriate variance, just as the Gaussian random numbers above were filtered to give the proper variance and thus determine the strength of the corresponding complex exponential in the spatial domain. Thus, the two objectives involve finding an appropriate set of orthogonal low spatial frequency functions, and determining the corresponding variances applicable to atmospheric turbulence.

An arbitrary function can be expanded in terms of Karhunen-Loeve functions that are orthogonal by definition. To determine a set of Karhunen-Loeve functions appropriate for Kolmogorov turbulence, Cochrane builds on the work of Noll and (1975) considers expansion of an arbitrary function $\phi(r,\theta)$ over a circular aperture of radius R in terms of Zernike

polynomials (Born and Wolfe, 1970)

$$\phi(r, \theta) = \sum_{j=1}^{\infty} a_j Z_j(\rho, \theta), \quad (129)$$

where ρ represents the normalized distance r/R , a_j are the expansion coefficients, and Z_j are the Zernike polynomials. With $W(r/R)$ representing the aperture function, the coefficients are

$$a_j = (1/R^2) \int d^2r W(r/R) \phi(r, \theta) Z_j(r/R, \theta). \quad (130)$$

Noll assumed that these coefficients were Gaussian random variables with zero mean and with a covariance

$$\langle a_j^* a_{j'} \rangle = \int d\rho \int d\rho' W(\rho) W(\rho') Z_j(\rho, \theta) \langle \phi(R\rho) \phi(R\rho') \rangle Z_{j'}(\rho', \theta'). \quad (131)$$

Fourier transforming to the spatial frequency domain

$$\langle a_j^* a_{j'} \rangle = \iint d\kappa d\kappa' Q_j^*(\kappa) \Phi(\kappa/R, \kappa'/R) Q_{j'}(\kappa'), \quad (132)$$

where $Q_j(\kappa)$ represents the Fourier transform of the j th Zernike polynomial, and $\Phi(\kappa/R, \kappa'/R)$ represents the Kolmogorov spectrum of phase fluctuations. Noll analytically performed the integrals to give a covariance matrix in which the terms represent the expected covariances due to Kolmogorov turbulence.

Cochrane (1985) notes that the Zernike polynomials cannot be used to form an orthogonal expansion of the turbulence-distorted phase because the expansion coefficients are correlated, indicated by nonzero off-

diagonal elements in Noll's covariance matrix. However, the eigenvectors of the Zernike covariance matrix serve as a Karhunen-Loeve basis set. These eigenvectors K_p can represent turbulence because they are not correlated, i.e. each eigenvector K_p is formed by superposition of Zernike polynomials in such a way that the K_p are orthogonal, satisfying the first objective. Additionally, the corresponding eigenvalue λ_p multiplied by $(D/r_0)^{6/5}$ (where D is the aperture diameter and r_0 is Fried's coherence length (Fried, 1965)) gives the appropriate variance for that K_p spatial component corresponding with Kolmogorov turbulence, satisfying the second objective.

Specifically, the low spatial frequency contribution to the phase screen can be expanded in terms of these Karhunen-Loeve components K_p (Cochrane, 1985)

$$\phi(r) = \sum_{p=1}^{p_{\max}} \gamma_p K_p\left(\frac{r}{D/2}\right), \quad (133)$$

where p_{\max} represents the number of low spatial frequency Karhunen-Loeve terms included and the coefficients γ_p are Gaussian random numbers with variance λ_p and scaled by $(D/r_0)^{6/5}$ to the specific strength of turbulence used. The simulations use the first five terms ($p_{\max} = 5$) as a compromise between completeness of low spatial frequency correction and computational efficiency.

Figure (47) shows a surface plot of one realization of the first two terms of the correction, which are very close to x- and y-tilt (i.e. phase terms linear in x and y, respectively). Figure (48) shows a realization of the 3rd, 4th, and 5th correction terms, which resemble the wavefront aberrations associated with defocussing and astigmatism in a conventional imaging system. To implement the low spatial frequency phase correction, (1) the scalar product was formed between the initial Fourier transform phase screen and each Karhunen-Loeve function K_p , giving the relative strength of that K_p in the initial phase screen; (2) this amount of each spatial component K_p was then subtracted from the phase screen; and (3) the K_p component was then added back to the phase screen in the proper amount given by the product of a Gaussian random number γ_p with variance λ_p and the factor $(D/r_0)^{5/3}$ to scale to the particular strength of turbulence used.

Cochrane's computer routines only calculate the Karhunen-Loeve correction terms over the largest circle that fits inside the calculation grid, as shown in Figs. (47) and (48). Correction of the E-field over the entire computer simulation grid requires the Karhunen-Loeve terms be calculated over an area that is at least $\sqrt{2}$ larger on each side than the field grid (Cochrane, 1985). If the E-field grid size N is chosen as a power of 2, then the Karhunen-Loeve grid must be $2N \times 2N$. These simulations however used only an $N \times N$ grid (1024×1024) because the Sun SparcStations could not handle the memory

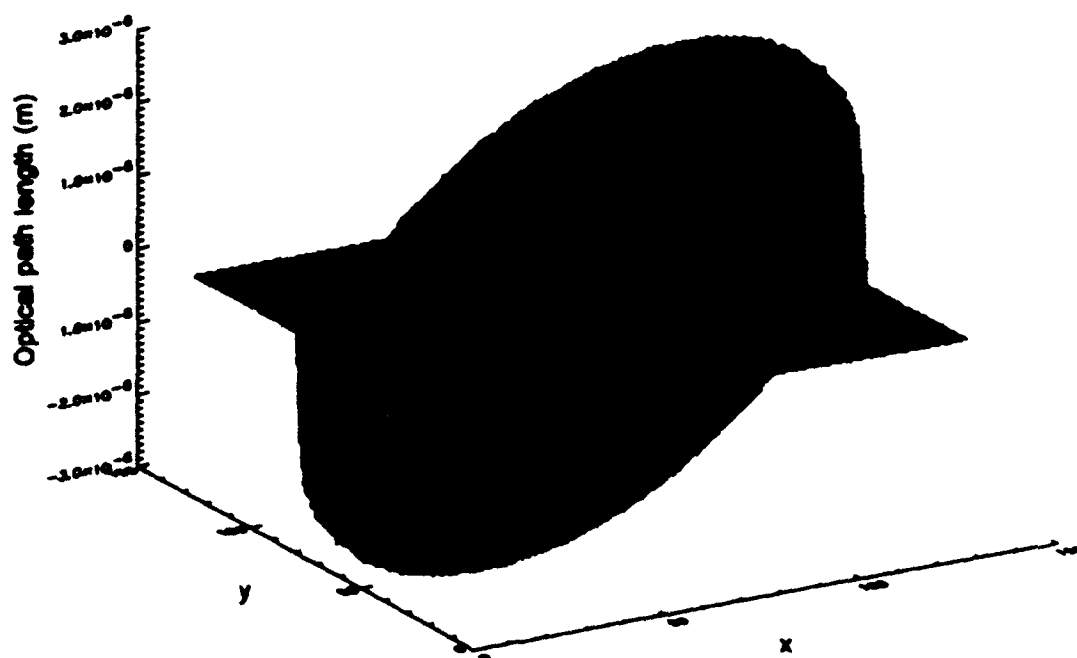


Figure 47 Terms 1 and 2 of Karhunen-Loeve low spatial frequency correction to phase screen, represented in optical path length for wavelength = 500 nm.

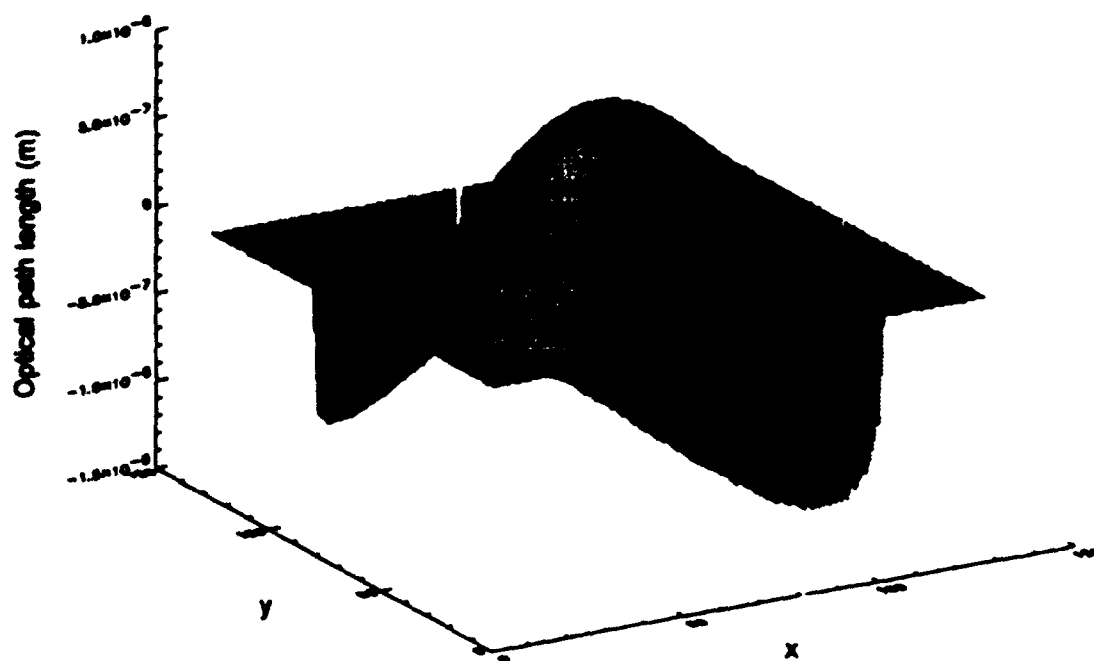


Figure 48 Terms 3, 4, 5 of Karhunen-Loeve low spatial frequency correction to phase screen, represented in optical path length for wavelength = 500 nm.

requirements of the doubled grid (2048x2048) without a major revision of the propagation code. Since the source function was chosen to minimize energy scattered off the grid, very little energy fell in the uncorrected corners of the grid and the simulation remained valid.

Noll's covariance matrix assumes Kolmogorov turbulence spectrum with zero inner scale making the Karhunen-Loeve correction terms strictly apply only to this spectrum. These simulations however incorporate nonzero inner scales into the spectrum of refractive index fluctuations. Because the first five Karhunen-Loeve terms cover scale sizes on the order of the grid width, which is much larger than the inner scale size l_0 , the Karhunen-Loeve correction terms derived for zero inner scale remain valid for correcting nonzero inner scale phase screens.

Cochrane (1985) showed that such low spatial frequency correction greatly improved the phase structure function. Two terms corrected the structure function to within 10% of the theoretical Kolmogorov behavior, and five terms corrected to within 5%, compared with 30 - 1000% discrepancies without any correction at low spatial frequencies. Figure (49) plots the normalized irradiance variances from computer simulations as a function of β_0^2 for zero Karhunen-Loeve low frequency correction, two-term correction, and five-term correction. Zero correction underestimated the irradiance variance in the Rytov regime by approximately 5%, and the two-term tilt-type correction also

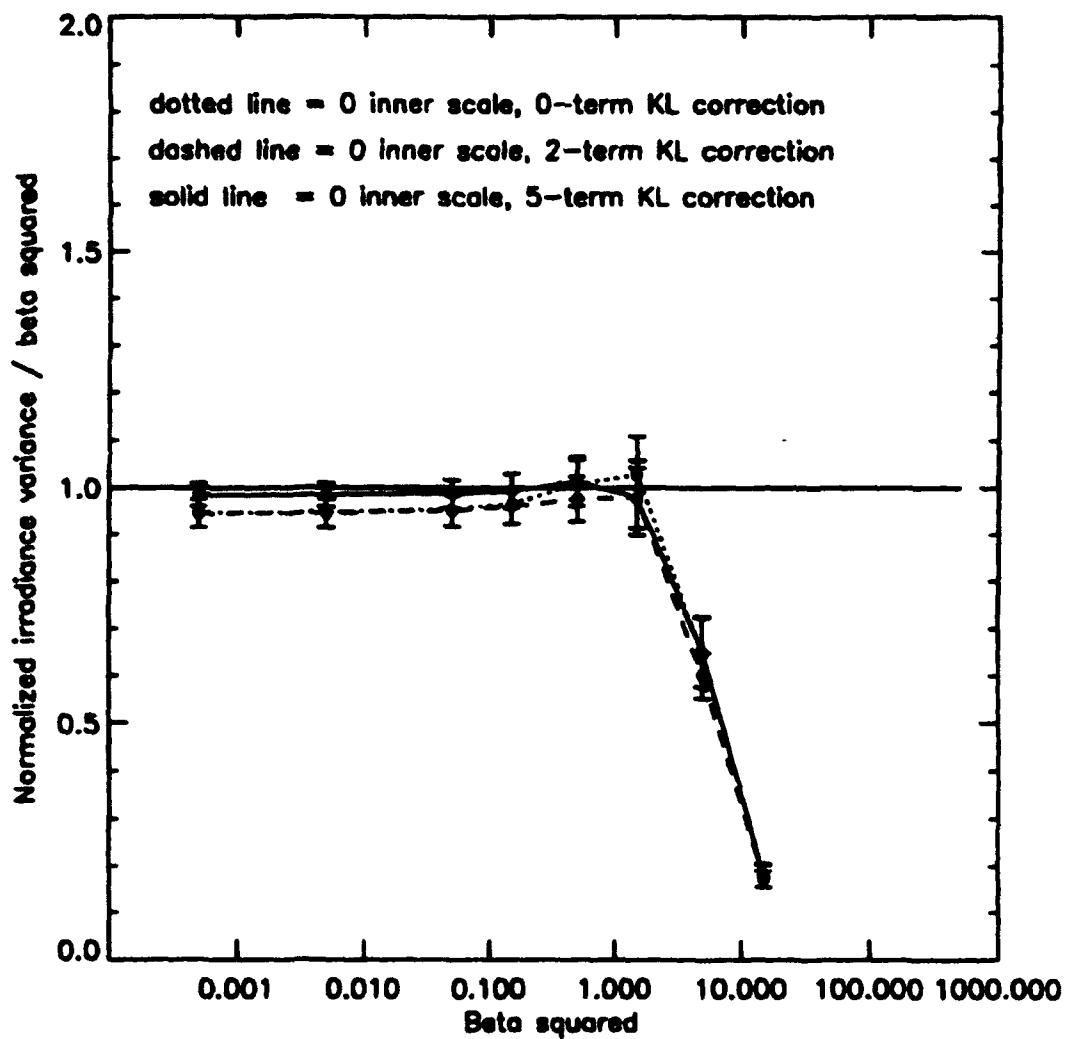


Figure 49 Normalized irradiance variance, normalized by β_0^2 , versus turbulence strength for zero (dotted), two-term (dashed), and five-term (solid) Karhunen-Loeve low spatial frequency corrections to phase screens.

underestimated by about 5%. The five-term correction with its focussing type terms raised the variance to within about 2% of the theoretical variance. In the saturation regime, the two- and five-term corrections fit better. Figure (50) plots the coherence length r_0 , normalized by the theoretical coherence length, as a function of turbulence strength for zero, two-, and five-term Karhunen-Loeve low spatial frequency corrections. In the Rytov regime where simulation should closely approximate theory, the zero correction overestimated the coherence length by approximately 35%. The tilt-type correction (two terms) estimated the coherence length within about 5%, and the five-term correction achieved agreement within about 2%. These behaviors formed the guideline that some type of low spatial frequency correction was required to achieve valid coherence lengths from computer simulation.

This low spatial frequency correction method remained computationally feasible because the Noll covariance matrix only needed to be calculated once and because only a few terms of the Karhunen-Loeve expansion were used. However, the code can become memory intensive because it saves a full $N \times N$ grid for each Karhunen-Loeve function in addition to the $N \times N$ phase screen itself. Implementation with 2048×2048 or larger grids becomes problematical except on very large computers with about one gigabyte of RAM. Fried(1993) has proposed a simpler x- and y-tilt correction algorithm and indicates that this performs almost as well as including the higher order

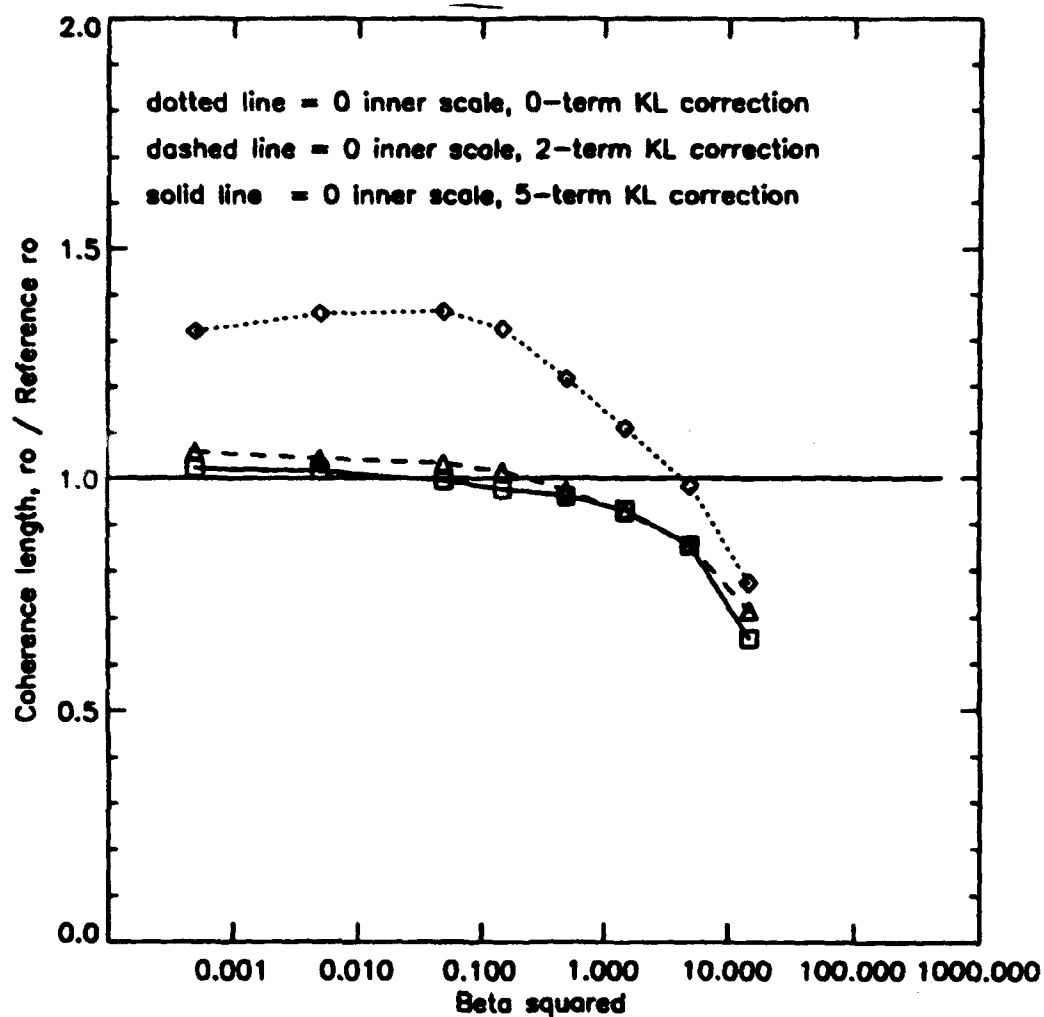


Figure 50 Spherical wave coherence length, normalized by theoretical coherence length, versus turbulence strength for zero (dotted), two-term (dashed), and five-term (solid) Karhunen-Loeve low spatial frequency corrections to phase screens.

Karhunen-Loeve terms, while being less memory intensive and faster than the Karhunen-Loeve correction method. Figs. (49) and (50) indicate that the tilt-only correction may systematically underestimate the normalized irradiance variance by about 5% and overestimate the coherence length of a spherically diverging wave by about 5% in the Rytov regime. Depending on the application, the Karhunen-Loeve correction to higher order terms may prove a useful refinement.

H. COHERENCE LENGTH

The coherence length of the E-field was calculated from the atmospheric MTF with the theory outlined in Chapter II, but the actual implementation of the MTF calculation and parameterization of the coherence length r_0 required careful consideration. The calculation methods that worked best for these investigations are discussed in this section.

Equation (60) of Chapter II relates the atmospheric MTF and the spherical wave structure function to the coherence properties of the E-field

$$MTF_{atmos} = e^{-\frac{1}{2} D(\rho)} = \frac{\langle \tau(\rho) \rangle_{long\ exposure}}{\tau_o(\rho)} = \frac{\langle \langle U(\rho') U(\rho'+\rho) \rangle \rangle}{\langle W(\rho') W(\rho'+\rho) \rangle}. \quad (134)$$

Again, $U(\rho)$ represents the E-field and $W(\rho)$ represents the aperture function.

The autocorrelations of U and W indicated in Eq. (134) could be done by

summing the complex products of the E-fields over multiple pairs of points or by implementing the autocorrelation via FFT techniques. Both versions were tried for these investigations and produced similar results, but the FFT version provided a much more thorough autocorrelation with greater computational efficiency.

The FFT autocorrelation technique used the MCF introduced earlier. Equation (57) defined the mutual coherence function as

$$MCF = \langle U^*(r_1, t_1) U(r_2, t_2) \rangle, \quad (135)$$

which, for a single time $t_1 = t_2 = t$ and assuming homogeneity, may be written as the spatial autocorrelation of the E-field

$$MCF(r'') = \int d^3r U^*(r) U(r + r''). \quad (136)$$

Substituting Eq. (136) into the Fourier transform identity,

$$MCF(r') = \int d^3r' \left[\int d^3r'' MCF(r'') e^{-i2\pi r' \cdot r''} \right] e^{+i2\pi r' \cdot r'}, \quad (137)$$

gives

$$MCF(r') = \int d^3r' \left[\int d^3r'' \left[\int d^3r U^*(r) U(r+r'') \right] e^{-i2\pi r' \cdot r''} \right] e^{+i2\pi r' \cdot r'}. \quad (138)$$

Rearranging the integrations,

$$MCF(r') = \int d^3r' \left[\int d^3r U^*(r) \left[\int d^3r'' U(r+r'') e^{-i2\pi r' \cdot r''} \right] \right] e^{+i2\pi r' \cdot r'}. \quad (139)$$

Changing variables to $s = r + r''$, $r'' = s - r$, $d^3r'' = ds$,

$$MCF(r') = \int d^2r \left[\int d^2r' U^*(r') \left[\int d^2s U(s) e^{-i2\pi r' \cdot s} \right] e^{+i2\pi r' \cdot r} \right] e^{-i2\pi r' \cdot r'}. \quad (140)$$

The inner integral is the Fourier transform of $U(s)$ and is denoted by $FT[U]$.

The next innermost integral is the inverse Fourier transform of $U^*(r')$ and is denoted by $IFT[U^*]$. Then,

$$MCF(r') = \int d^2r FT[U] IFT[U^*] e^{-i2\pi r' \cdot r}, \quad (141)$$

which is yet another inverse Fourier transform, symbolically written

$$MCF(r') = IFT[FT[U] IFT[U^*]]. \quad (142)$$

Equation (142) expresses the autocorrelation (MCF) of the E-field in terms of Fourier transform techniques easily implemented with discrete Fourier transforms.

This Fourier transform method of calculating the autocorrelation of a function is faster and more complete than the more laborious technique of averaging the products of the E-field at point pairs. The product $E^*(r_1)E(r_2)$ is complex, but because of the averaging that occurs in the autocorrelation, the real part attains a stable value while the imaginary part averages toward zero. For the FFT implementation on a 1024x1024 grid, the imaginary part is typically $\sim 10^{-6}$ while the real part ranges between 0 and numbers on the order of unity. The point pairs technique produces an equivalent real part but reduces the imaginary part down to only $\sim 10^{-3}$. These investigations used the FFT version for all autocorrelations. Additionally, the autocorrelations were normalized by their

zero lag values to ensure that the magnitude of the MTF_{atmos} calculated by Eq. (134) lies between 0 and 1.

Because the spherical wave structure function refers to points across a spherical wavefront, U and W must similarly represent the E-field across a spherical surface. However, the computer simulation implements the E-field on a plane perpendicular to the axis of propagation and incorporates the spherical wave nature of the E-field by applying a quadratic phase curvature across the plane. To convert from this plane representation of the E-field in the simulation to a spherical surface representation appropriate for the autocorrelation calculations of Eq. (134), the quadratic phase factor across the plane must be removed from the E-field. This effectively assumes that the amplitude and the phase fluctuations of the E-field across the plane of the computational grid closely approximate the E-field across the spherical wave. This assumption is justified because the maximum physical separation of the true spherical reference surface from the plane surface of the grid is at most 1/50 the coherence length of the E-field. However, the removal of the quadratic phase curvature from the E-field of the grid proves crucial to the autocorrelation of U because the quadratic phase factor undergoes ~130 multiples of 2π phase change between the center and the outer edge of the grid for these simulations and would otherwise completely obscure the actual E-field fluctuations.

Propagation with a plane or beam wave requires a different approach to remove the proper amount of phase curvature. For a plane wave, the wavefront coincides with the plane of the grid so that no phase curvature needs to be removed. A pure beam wave (Gaussian profile) exhibits a spherical phase with a radius of curvature larger than the propagation distance L , and this phase could be calculated analytically and removed. However, the use of a finite E-field confined to the propagation grid introduces phase effects other than simple quadratic curvature. Fortunately, the E-field propagated through zero turbulence contains this phase curvature information (Walters, 1994). For spherical wave propagations, the removal of the phase curvature by the analytical calculation and by using the zero turbulence propagated field provided identical coherence lengths. These investigations used the latter method for the coherence length calculations for all beam-like and plane-wave-like propagations.

Equation (134) requires that the autocorrelation of U must be averaged over multiple realizations to achieve the long exposure MTF. To implement this requirement, the autocorrelations from several realizations were calculated and averaged together, and a coherence length then determined via Eq. (134). This method produced coherence lengths that agreed with theory within ~5% in the Rytov regime. Recalling Fig. (45) for the coherence length versus number of realizations used in the average, the number of fields included in the MTF

average may be as few as 5, though 20 provided a more statistically reproducible coherence length. Again, these simulations used 30 realizations because these fields had already been generated for the normalized irradiance variance calculations.

Figure (51) plots the coherence lengths calculated from the average MTF and also plots the average of coherence lengths calculated with single realization MTF's. The average of individual realization coherence lengths exceeded the averaged MTF coherence length by ~20% at low turbulence strengths but eventually agreed within 5% near the saturation regime. The single realization MTF's showed a larger coherence length at low turbulence strengths because the contributions from low spatial frequency components had not been reduced through averaging. At these low turbulence strengths, multiple realizations were required to average these low spatial frequency contributions and to achieve the appropriate long exposure MTF. At higher turbulence strengths near saturation, the E-field had more energy at high spatial frequencies that dominated the MTF. The autocorrelation for a single realization now averaged over many coherence lengths and yielded an MTF close to the average MTF for multiple realizations.

Using a finite beam to approximate a spherically diverging wave produced a radial dependence of the average irradiance that affected the coherence length calculation, but only to a small degree. To compensate for

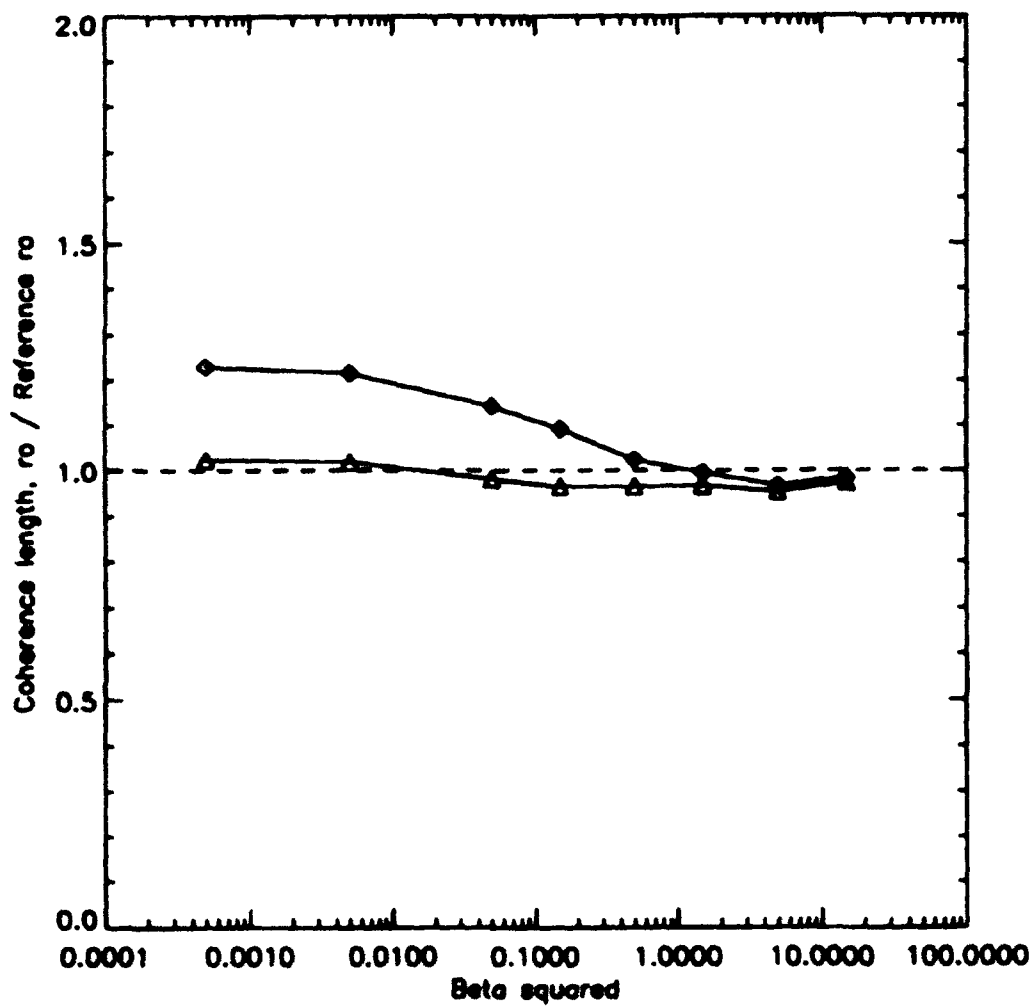


Figure 81 Coherence lengths r_0 obtained by averaging r_0 's from individual realizations (diamonds) and from averaging the MCF's of individual realizations prior to calculating r_0 (triangles).

this radial dependence, each E-field was divided by the radial average E-field magnitude from the 30 realizations. Similar to the irradiance variance calculation, this average E-field was calculated by dividing the grid into rings one grid element wide, taking the square root of the average intensity for each ring over the 30 realizations, and then performing an area weighted, running mean across the rings to smooth the variations. While this radial compensation proved essential for the normalized irradiance variance calculation, it only changed the coherence length by ~1%, which was significantly less than the ~5% discrepancy from the low spatial frequency correction.

The above considerations allowed calculation of the right-hand side of Eq. (134) for the atmospheric MTF. Because of the statistical nature of the propagation through turbulence, no set of realizations yielded an atmospheric MTF that exactly followed the exponential rolloff with distance predicted by the left-hand side of Eq. (134). Methods had to be developed to parameterize these atmospheric MTF's from the simulations and extract an appropriate coherence length corresponding to the structure function $D(r)$.

For the case of Kolmogorov turbulence, Fried (1966, p. 1380-1383) derived the wave structure function and expressed it in terms of the single coherence length parameter r_0 ,

$$D(r) = 6.88 \left(\frac{r}{r_0} \right)^n, \quad (143)$$

where $n = 5/3$. The atmospheric MTF then becomes

$$MTF_{atmos} = e^{-3.44 \left(\frac{r}{r_0}\right)^n} \quad (144)$$

To extract the coherence length r_0 and the exponent n (allowing the possibility that n may vary), take the natural logarithm of both sides and rearrange (Walters, 1993)

$$-\frac{1}{3.44} \ln(MTF_{atmos}(r)) = \left(\frac{r}{r_0}\right)^n \quad (145)$$

Taking the natural logarithm again,

$$\ln\left(-\frac{1}{3.44} \ln(MTF_{atmos}(r))\right) = n \ln(r) - n \ln(r_0). \quad (146)$$

This has the linear form $y = ax + b$, where y represents the left hand side, $a = n$, $x = \ln(r)$, and $b = -n \ln(r_0)$. The atmospheric MTF can now be characterized with two parameters, r_0 and n , or just the single parameter r_0 assuming $n = 5/3$.

To implement these parameterizations, the atmospheric MTF was first calculated from the E-field using the autocorrelation methods above and then radially averaged to yield $MTF_{atmos}(r)$ for use in Eq. (146). A linear least squares fit calculation provided the slope $a = n$ and the intercept $n \ln(r_0)$, giving r_0 . To obtain the single parameter characterization, n was set to $5/3$ in

Eq. (146) and least squares techniques applied to obtain the intercept and thus the single parameter r_0 .

Figure (52) shows the coherence lengths calculated with these least squares methods, divided by the Rytov theory coherence length for Kolmogorov turbulence. The two parameter characterization with both exponent n and coherence length r_0 never provided a consistent, smoothly varying coherence length. At low turbulence strengths in the Rytov regime where the E-field coherence length is larger than the calculation aperture, the two parameter fit predicted coherence lengths up to 50% higher than the theoretical value and thus appears unreliable. Additionally, it showed an anomalous bump around $\beta_0^2 \sim 0.5$. The single parameter least squares technique with $n = 5/3$ accurately characterized the coherence length within 5% at low turbulence strength, but still showed the bump at $\beta_0^2 \sim 0.5$.

An alternate technique to obtain a single parameter characterization assumed $n = 5/3$ in Eq. (144) and used a binary-type search, or iterative fit, to find the coherence length r_0 that minimized the variance between the average $\text{MTF}_{\text{atmos}}(r)$ and the right-hand side of Eq. (144). Though not analytical, the resulting r_0 gave an MTF that often fit the actual $\text{MTF}_{\text{atmos}}(r)$ more closely by eye than the least squares methods, especially for low turbulence where coherence lengths were larger than the grid size. To implement the technique, an initial large range of r_0 (for example, 0 to 100 m) was divided in half, the midpoint r_0 's

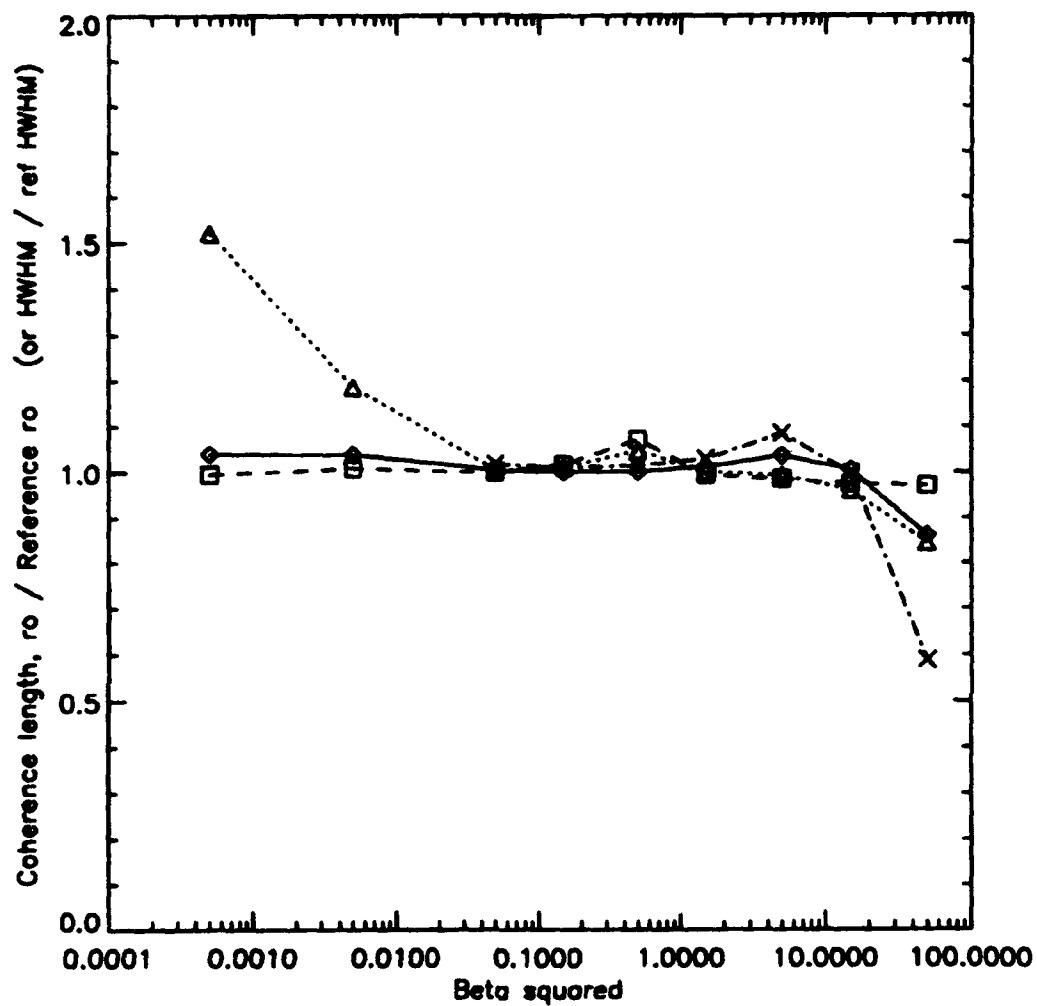


Figure 52 Coherence lengths calculated by one-parameter (dashed line) and two-parameter (dotted line) least squares techniques, the iterative fit technique (solid line), and the HWHM (dash-dot line).

of each half were substituted into Eq. (144), and the variances were calculated. Whichever r_0 provided the least variance became the middle of the next range, and the other r_0 became the new high or low boundary. The process was then repeated, so that each iteration reduced the range of possible r_0 by 1/3. This procedure was iterated 100 times or until the variance was less than 1×10^{-7} .

Figure (52) shows the coherence lengths predicted by this iterative fit method along with the coherence lengths from the one- and two-parameter least squares fits, all divided by the Rytov theory coherence length for Kolmogorov turbulence. The iterative fit coherence length was ~5% too large at low turbulence but did not show the anomalous bump around $\beta_0^2 \sim 0.5$.

In the saturation regime where turbulence is high and/or path lengths are long, multiple scattering becomes significant and saturates the irradiance variance (Martin and Flatté, 1988). Correspondingly, this physical phenomenon may also affect the coherence length and modify the value of n or the form of Eq. (144) for the saturation regime. The half width at half maximum (HWHM) provided a coarser, one parameter method of characterizing the atmospheric MTF that did not depend on any assumptions about the form of the structure function and could be calculated directly from the atmospheric MTF by linearly interpolating between the pair of points bounding $MTF_{atmos}(r) = 1/2$. Figure (52) plots the HWHM, divided by the HWHM predicted by Rytov theory assuming Kolmogorov turbulence. The HWHM plot starts at $\beta_0^2 = 0.05$ because lower

turbulence strengths gave a coherence large enough that the $MTF_{atmos}(r)$ had not reached half its maximum value within the calculation region. The HWHM lengths followed the theoretical values within 5% in the Rytov regime and did not show the anomalous bump around $\beta_0^2 \sim 0.5$. Note that the iterative fit coherence lengths agreed with the HWHM plot better than the least squares techniques. The HWHM and iterative fit r_0 proved to be the most stable parameterizations of the E-field coherence length, and were used in all subsequent coherence length comparisons and plots.

Other factors were also considered in the coherence length calculation. As stated earlier, some choices for point source, such as the Airy-type source required more energy at high spatial frequencies than others, such as a narrow Gaussian. While this difference produced < 2% effect in the normalized irradiance variance calculations, it appeared to have more effect on coherence length calculations. Figure (53) shows that an Airy-type source produced coherence lengths up to 10% higher at low turbulence strengths than those from the Gaussian-type source of Eq. (109). Therefore, only the latter type source was used for further investigations.

For an arbitrary spectrum of refractive index fluctuations $\Phi_n(\kappa, z)$, the integral formulation Eq. (61) provided the wave structure function for the atmospheric MTF in Eq. (134). Specifically, numerical integration of Eq. (61) for the spectra with grid cutoff, Gaussian, and Hill/Frehlich viscous convective

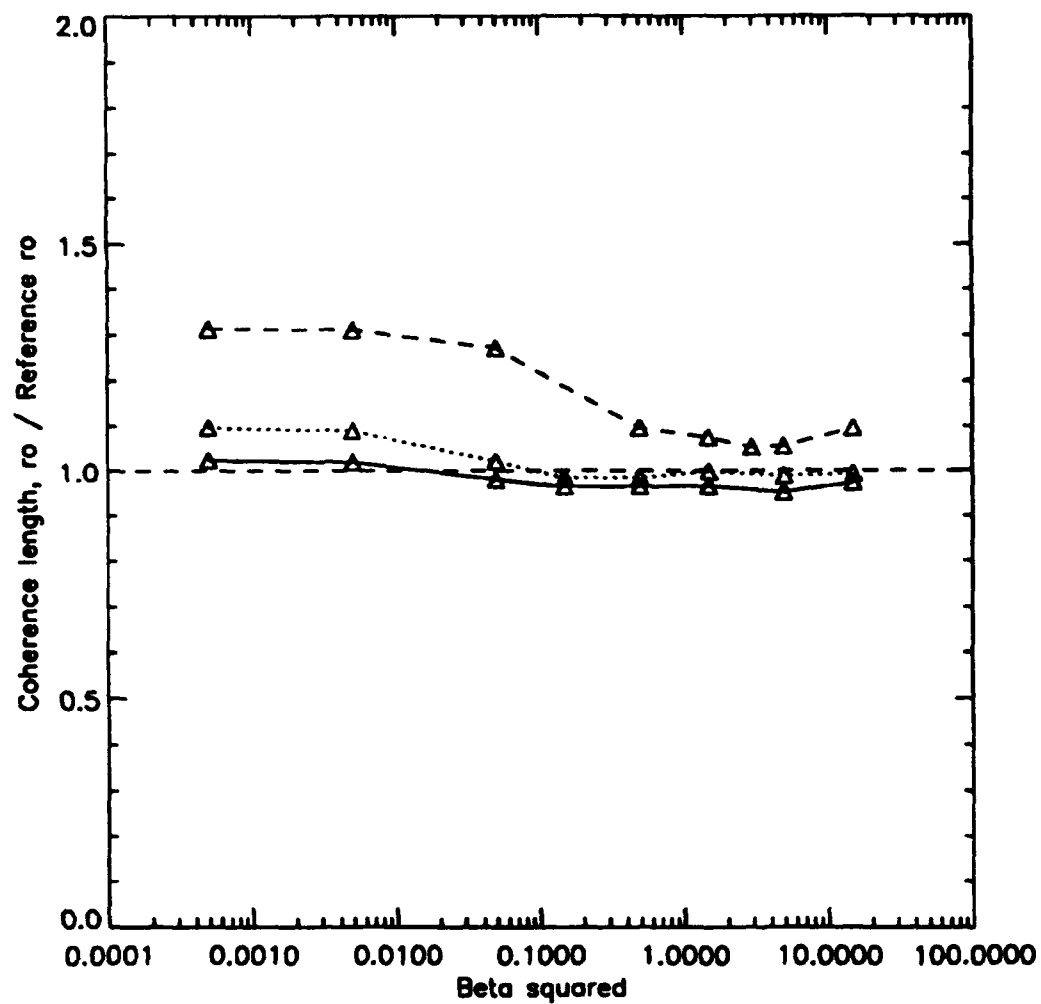


Figure 53 Iterative fit coherence lengths versus turbulence strength for Airy-type source (dotted), Gaussian-type source (solid), and Gaussian-type source with zero Karhunen-Loeve low spatial frequency corrections (dashed).

enhancement inner scales allowed comparison of theory (Eq. (134)) and the simulation $MTF_{atmos}(r)$ (described in Chapter IV). However, in the structure function numerical integration, care had to be exercised in properly treating the low spatial frequency portion of the integrand since the spectra contained a $\kappa^{-11/3}$ singularity as κ approached zero. This low frequency portion was critical to obtain coherence lengths that approached the Kolmogorov theoretical values in the Rytov regime. The integral was successfully evaluated by integrating analytically for $0 < \kappa < \kappa_{min}$, (where $\kappa_{min} \sim 1 \times 10^{-4} \text{ m}^{-1}$) (Walters, 1994) since the inner scale function $F(\kappa \ell_0) = 1$ here and this portion of the spectrum remains Kolmogorov. The remaining portion of the integral that contained the inner scale contribution was carried out numerically. More realistic spectra could also have included an outer scale, but again no universal form of outer scale exists due to anisotropy of the atmosphere at large scale sizes. When included in the numerical integrations for test purposes, an outer scale raised the coherence length compared to the Kolmogorov case. However, these investigations did not use an explicit outer scale in the simulations.

IV. RESULTS

A. NORMALIZED IRRADIANCE VARIANCE

The computer simulation guidelines and considerations discussed in Chapter III were implemented to investigate the behavior of the normalized irradiance variance and E-field coherence length in the Rytov and saturation regimes for the grid cutoff, Gaussian, and Hill/Frehlich viscous-convective enhancement inner scales. Specifically, the simulations apply to stratospheric propagation with propagation distance $L = 200$ km, wavelength $\lambda = 500$ nm, strengths of turbulence $\beta_0^2 = [5 \times 10^{-4}, 50]$, and inner scale sizes $[0, 15]$ cm. The simulations used a 1024×1024 grid with grid element size given by Eq. (92), an Airy-type source modified to produce a final zero turbulence irradiance pattern with edges apodized by a Gaussian (Eq. (109)) and width corresponding to half the grid width, 32 phase screens utilizing a five-term Karhunen-Loeve low spatial frequency correction, and 30 realizations in each set of runs. The central 256×256 portion of each propagated E-field was used for the normalized irradiance variance and coherence length calculations.

For the Gaussian inner scale values of 0 (grid cutoff), 5, 10, and 15 cm, Fig. (54) plots the normalized irradiance variance versus turbulence strength β_0^2 in the Rytov regime from both numerical integration of the equation from Rytov-Tatarski theory, Eq. (34) (dotted lines), and from computer simulations

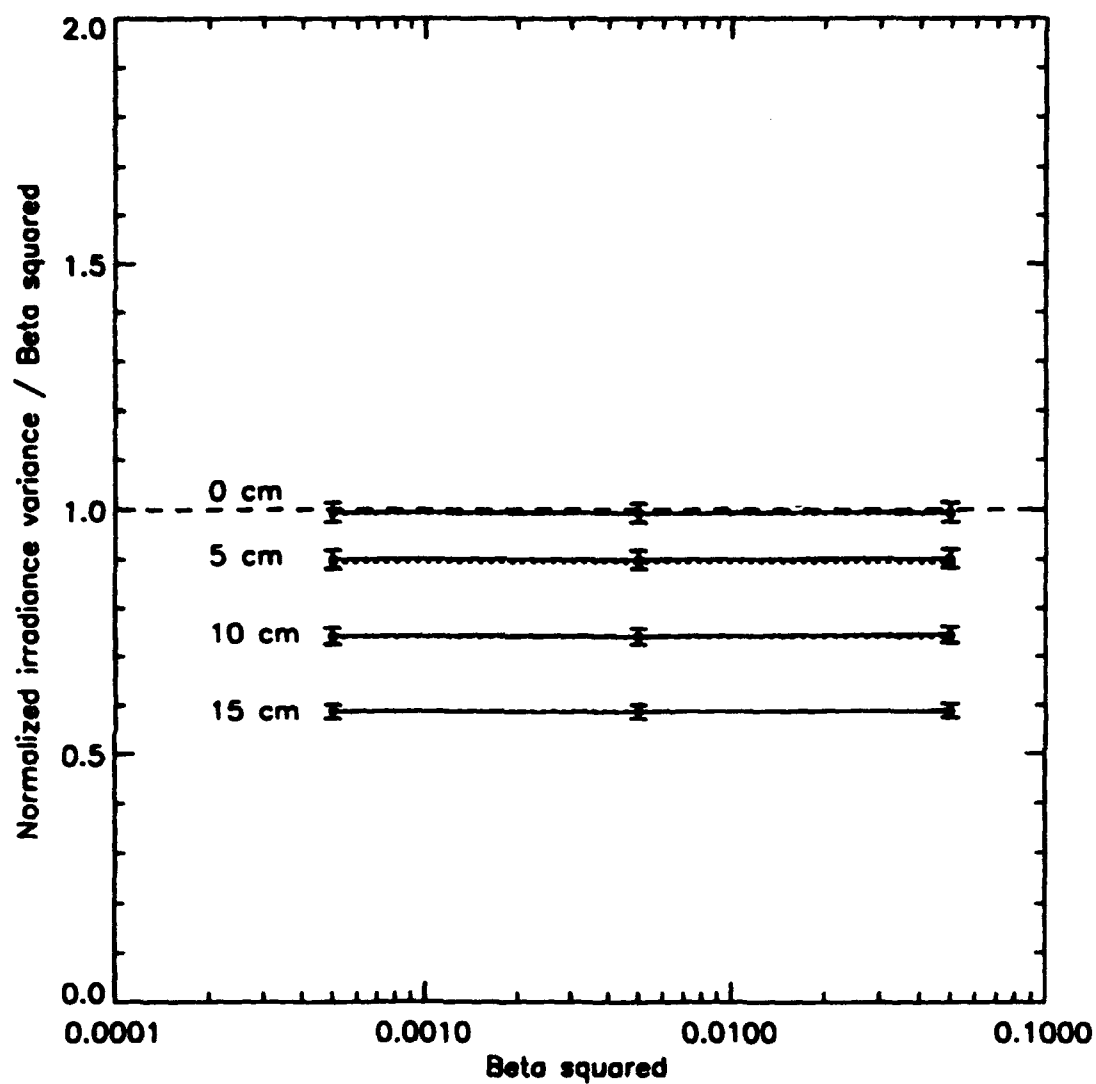


Figure 54 Normalized irradiance variance (divided by β_0^2) from simulation (solid) and numerical integration (dotted) for Gaussian inner scales of 0, 5, 10, 15 cm.

(solid lines). All values are normalized by β_0^2 . Numerical integration values for 0 cm inner scale agreed within 1% of the theoretical zero inner scale values. The difference resulted because the numerical integration was limited to spatial frequencies below the grid cutoff κ_{max} . Larger grid cutoff values gave closer agreement. The simulation normalized irradiance variances agreed within 2% of the numerical integration values for all four inner scale values examined. Nonzero Gaussian inner scales reduced the normalized irradiance variance below the zero inner scale value (by 10%, 25%, and 40% for the 5, 10, 15 cm cases, respectively). Intuitively, the finite inner scale suppressed the higher spatial frequency index of refraction fluctuations and thus reduced the variance.

Figure (55) plots the normalized irradiance variance (divided by β_0^2) for the single turbulence strength $\beta_0^2 = 5 \times 10^{-4}$ and Gaussian inner scale sizes of 0 (grid cutoff), 5, 10, and 15 cm. The numerical integration values (dotted line) and computer simulation values (solid line) showed an almost linear decrease of the normalized irradiance variance with increasing inner scale size in the Rytov regime. As Flatté, Wang, and Martin (1993) point out, the Gaussian inner scale does not accurately describe the inner scale observed in the atmosphere but retains usefulness because it facilitates some theoretical calculations.

For the Hill viscous-convective enhancement inner scale sizes of 0 (grid cutoff), 5, 10, and 15 cm, Fig. (56) plots the normalized irradiance variance in

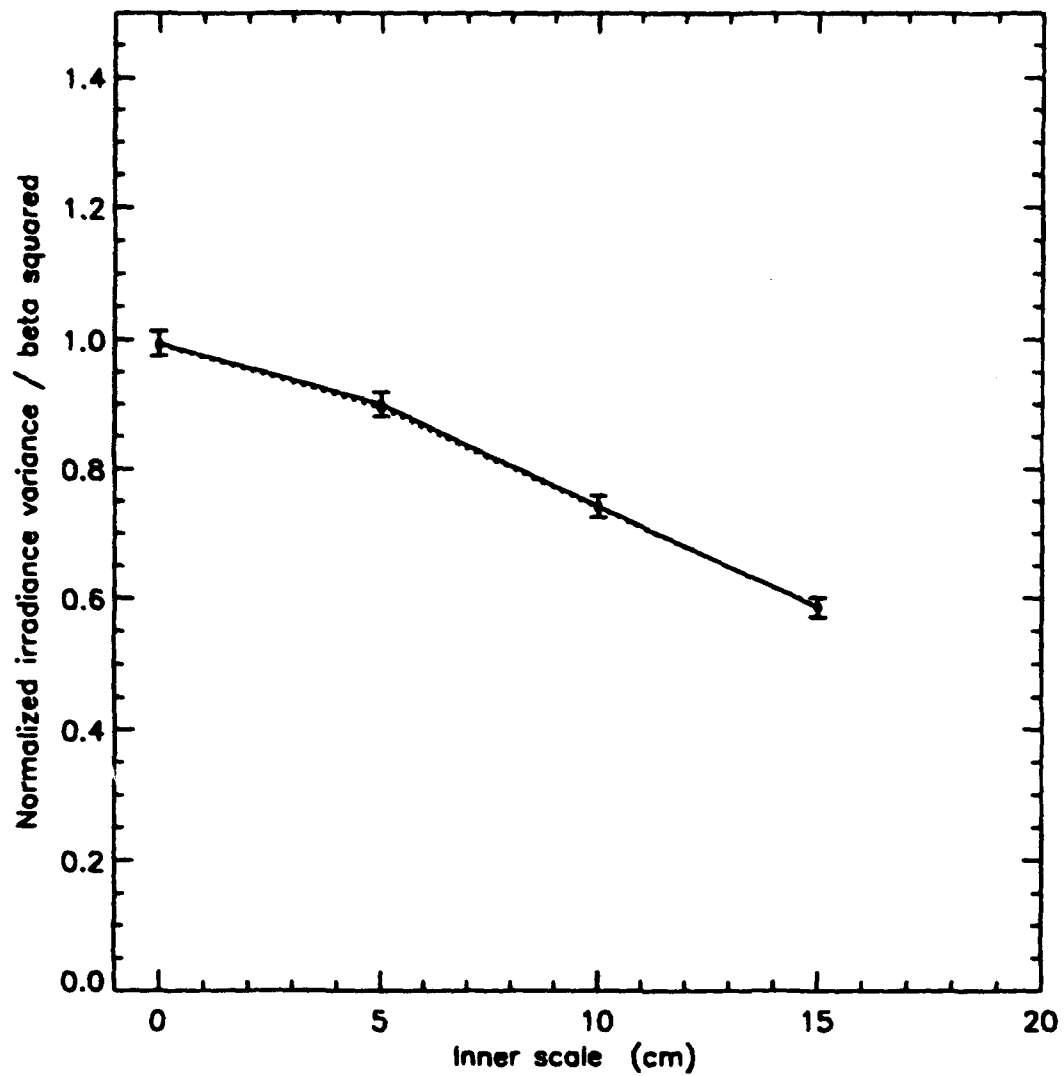


Figure 55 Normalized irradiance variance from simulation (solid) and numerical integration (dotted) for Gaussian inner scales of 0,5,10,15 cm at $\beta_0^2 = 5 \times 10^{-4}$.

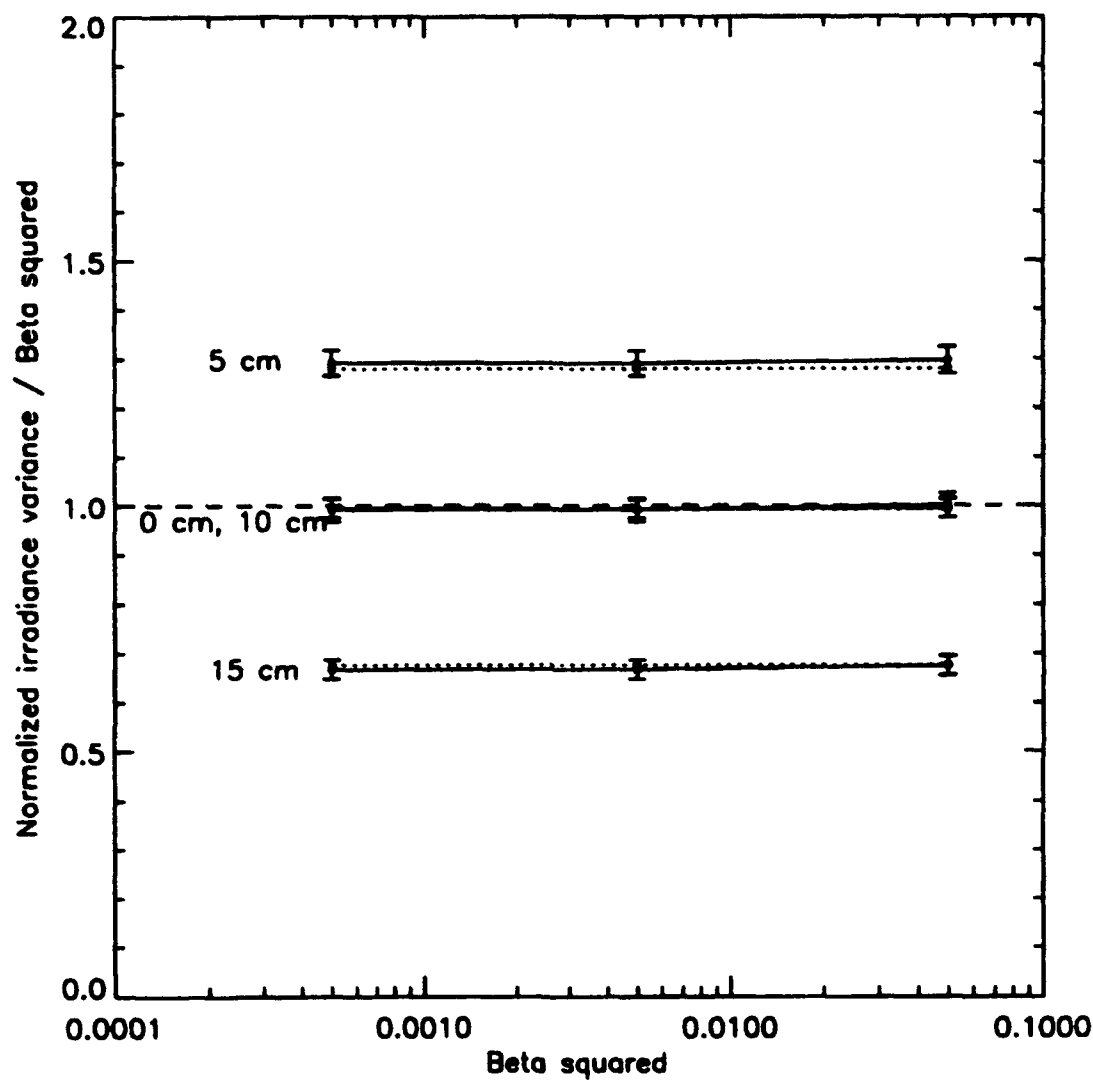


Figure 56 Normalized irradiance variance (divided by β_0^2) from simulation (solid) and numerical integration (dotted) for Hill viscous-convective enhancement inner scales of 0,5,10,15 cm.

the Rytov regime versus turbulence strength β_0^2 . Numerical integration of the Rytov-Tatarski theory, Eq. (34) (dotted lines), and computer simulation (solid lines) agreed within 2%. For the smaller inner scales, the normalized irradiance variance exceeded the zero inner scale values (by 30% for the 5 cm case). The viscous-convective enhancement of the strength of higher spatial wavenumber fluctuations near the inner scale wavenumber increased the variance. Yet, for large enough inner scale, the rolloff beyond the enhancement suppressed the higher spatial frequency fluctuations enough to eventually reduce the variance below the zero inner scale variance (by 30% for the 15 cm case). The 10 cm values happened to lie within 1% of the 0 cm values.

Figure (57) plots the normalized irradiance variance (divided by β_0^2) for the single turbulence strength $\beta_0^2 = 5 \times 10^{-4}$ and the Hill viscous-convective enhancement inner scale sizes of 0 (grid cutoff), 2, 3, 4, 5, 6, 7, 10, and 15 cm. Numerical integration of the Rytov-Tatarski results (dotted line) and computer simulation (solid line) clearly illustrated the rising and then falling behavior of the normalized irradiance variance with increasing inner scale size in the Rytov regime. The normalized irradiance variance achieved a maximum for $\ell_0 \sim 4$ cm, which was about 30% of the Fresnel length $R_f = \sqrt{\lambda L / 2\pi} = 12.6$ cm.

The dashed line in Fig. (57) shows simulation values using the Frehlich parameterization of the viscous-convective enhancement inner scale. The Frehlich inner scale shifted the plot slightly to smaller inner scale sizes,

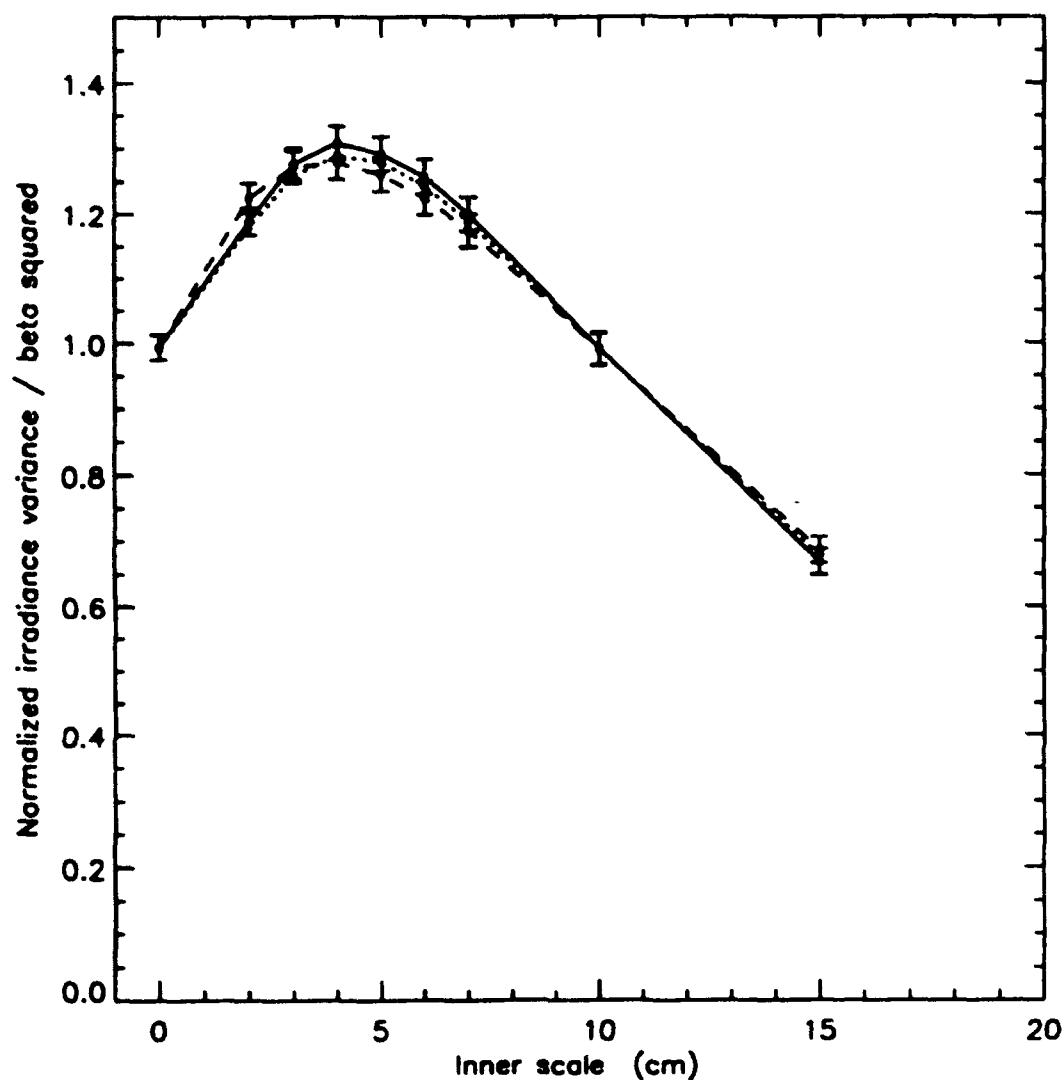


Figure 57 Normalized irradiance variance (at $\beta_0^2 = 5 \times 10^{-4}$) from Hill (simulation=solid, numerical int.=dotted) and Frehlich (simulation=dashed) inner scales of 0,2,3,4,5,6,7,10,15cm.

maximized at 2% less than the Hill maximum, and matched the Hill values within 3% over the range of inner scale plotted. Additionally, simulation runs using 4 cm Hill and Frehlich inner scales agreed within 3% over the range of turbulence strengths $5 \times 10^{-4} < \beta_0^2 < 50$. Thus, the Hill and Frehlich versions of the viscous-convective enhancement inner scale perform almost identically.

Previous investigations have illustrated the dramatic monotonic rise in normalized irradiance variance in the saturation regime as the inner scale size increases (Martin and Flatté, 1988). Figure (58) shows normalized irradiance variance from computer simulations for 0 (grid cutoff), 5, 10, and 15 cm Gaussian inner scales and a propagation path of 200 km. Figure (59) shows a corresponding plot for 0 (grid cutoff), 5, 10, and 15 cm Hill inner scales. The turbulence values range from the Rytov regime (low turbulence with $\beta_0^2 \leq 1$) to the saturation regime (high turbulence, $\beta_0^2 \geq 1$). The Rytov regime showed again the behaviors illustrated with Figs. (54) - (57). Increasing Gaussian inner scale size produced monotonically decreasing normalized irradiance variance. Martin and Flatté (1988, 1990) provided similar plots of normalized irradiance variance with a Gaussian inner scale. The Hill viscous-convective enhancement caused the normalized irradiance variance to rise and then fall as the inner scale size increased. However, in the saturation regime, the normalized irradiance variance increased monotonically with increasing inner scale size for both the Gaussian and Hill inner scales. The transition in

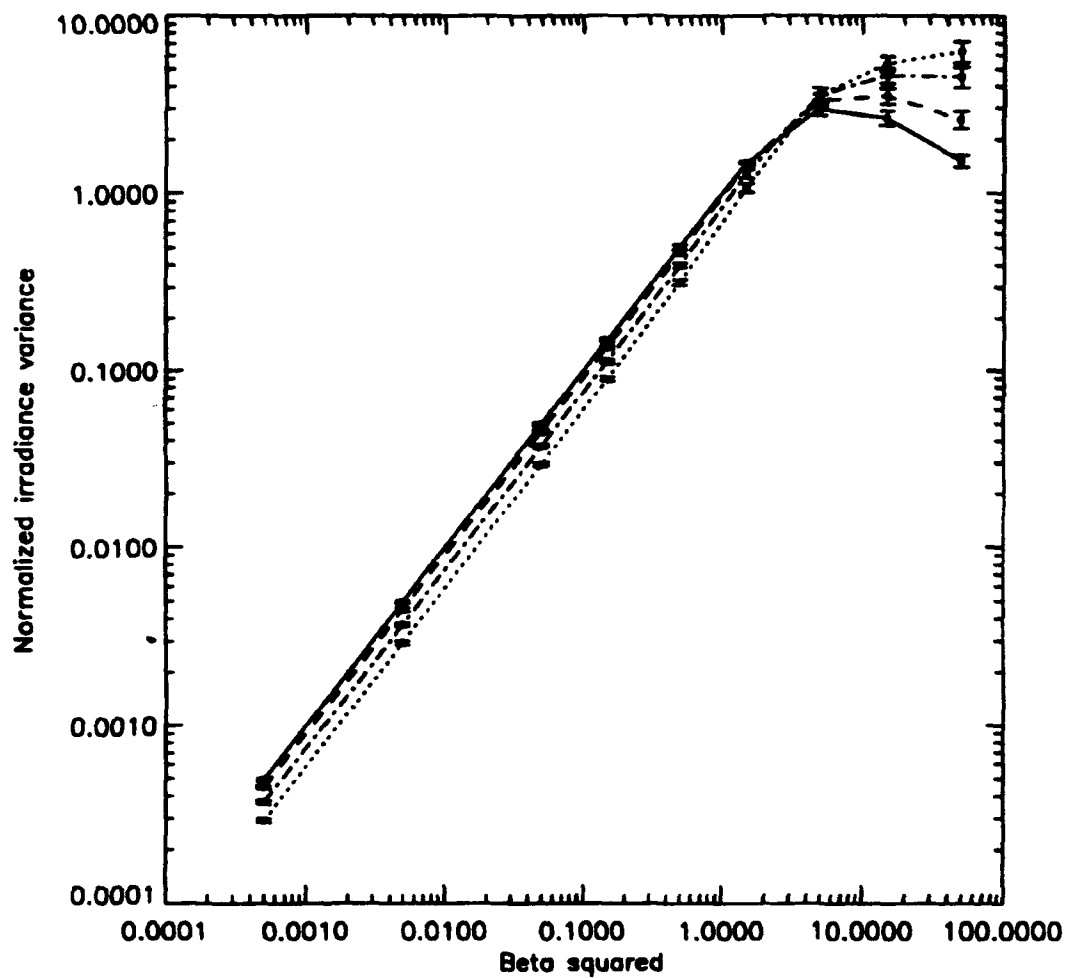


Figure 58 Normalized irradiance variance over Rytov and saturation regimes for Gaussian inner scales of 0 (solid), 5 (dashed), 10 (dash-dot), and 15 cm (dotted).

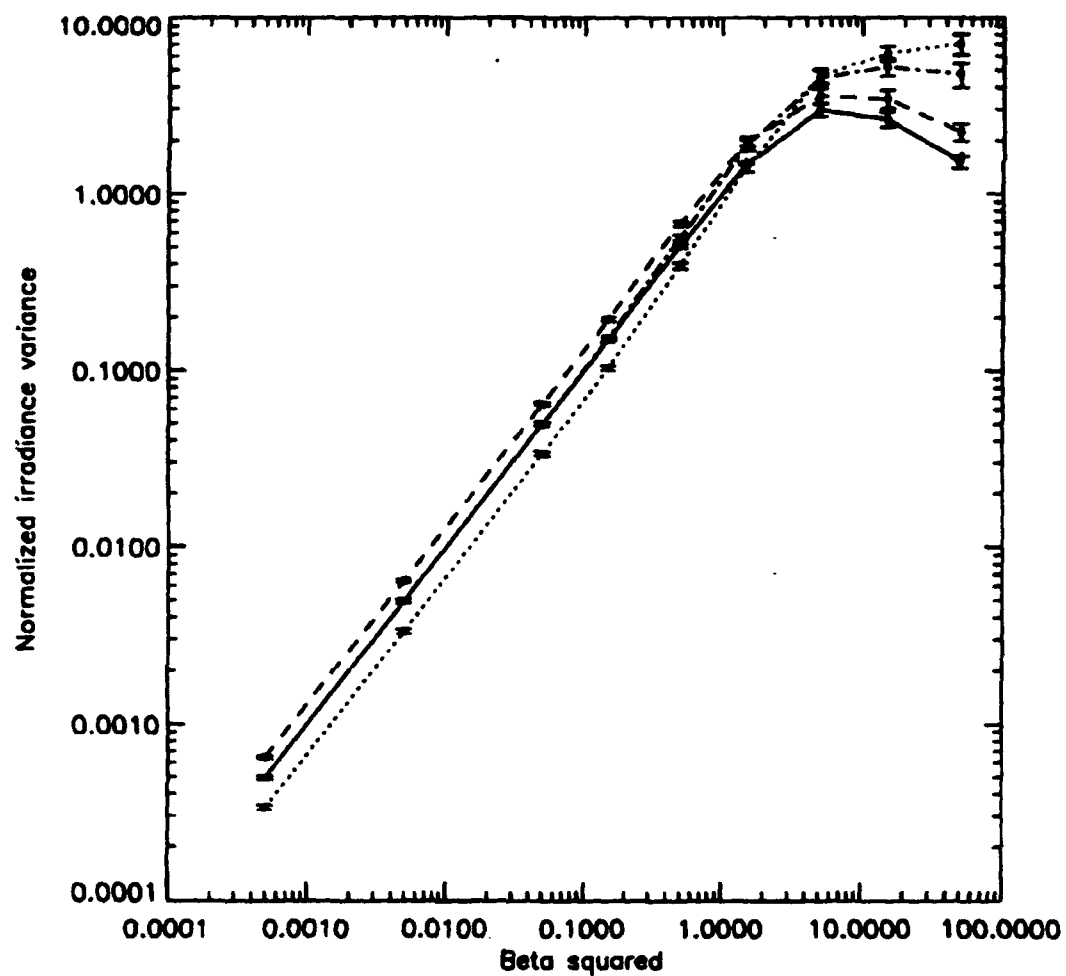


Figure 59 Normalized irradiance variance over Rytov and saturation regimes for Hill viscous-convective enhancement inner scales of 0 (solid), 5 (dashed), 10 (dash-dot), and 15 cm (dotted).

behavior occurred with the onset of saturation around $\beta_0^2 \sim 1$. This crossing behavior has been plotted for the log intensity variance with the viscous-convective inner scale by Hill and Clifford (1978).

Figures (54) - (57) illustrate the close agreement between numerical integration and computer simulation values for the normalized irradiance variance at low strengths of turbulence. This agreement provided a validity check on these computer simulations that incorporated an inner scale.

B. COHERENCE LENGTH

Coherence lengths of the E-field were calculated from the same 1024x1024 simulation runs used for the normalized irradiance variance calculation. The average atmospheric MTF was formed from 30 realizations using the FFT autocorrelation method, and then the corresponding coherence length r_0 and HWHM were calculated. The iterative fit r_0 's were used for comparisons because they most closely followed the HWHM behavior. The HWHM may provide the coarsest measure of coherence length but, since it requires no assumptions about the form of the MTF, it may also be the most reliable.

Figure (60) shows the coherence length r_0 from numerical integration of Eq. (61) for an approximately zero inner scale and normalized by the theoretical

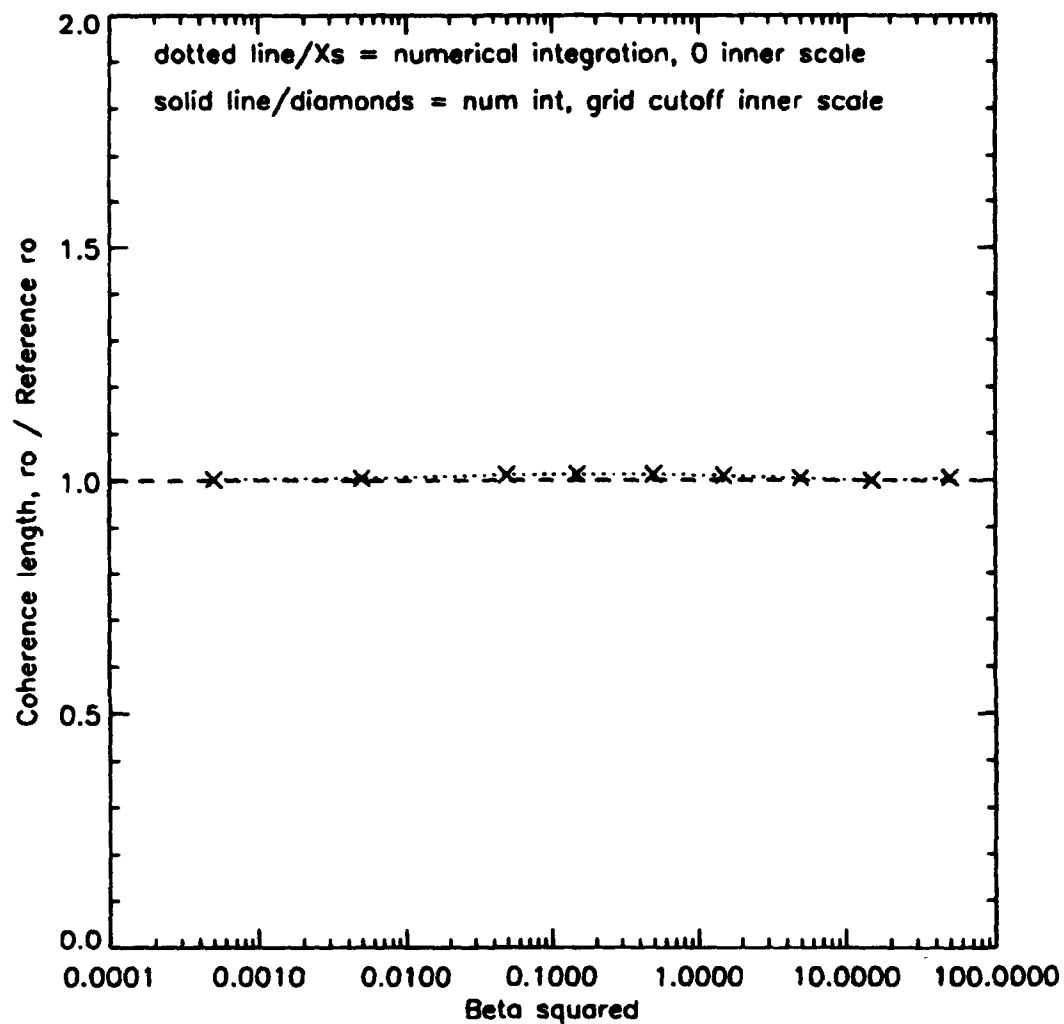


Figure 60 Coherence length from numerical integration for zero inner scale versus turbulence strength. Values normalized by Kolmogorov turbulence zero inner scale coherence length.

Kolmogorov turbulence zero inner scale coherence length r_0 of Eq. (66). This plot indicates that the numerical integration coherence lengths calculated in these investigations were accurate within 2%.

Figure (61) shows the coherence length r_0 from numerical integration of Eq. (61) with the grid cutoff $\kappa_{\max} = 318$ rad/m for the 1024x1024 grid. The grid cutoff did not affect the coherence length until $\beta_0^2 \approx 1.5$. Above that level of turbulence, the absence of the very high spatial frequency contribution to the integral caused the coherence length to become larger than the theoretical zero inner scale value. The grid cutoff inner scale implicit in the computer simulations with the finite grid should have a similar effect at these high turbulence values.

Figure (62) shows the coherence length r_0 , normalized by the theoretical coherence length, from computer simulation of a spherically diverging E-field. In the Rytov regime, the simulation agreed with theory to within the ~5% overestimation due to using only five terms in the Karhunen-Loeve low spatial frequency correction to the phase screens (see Fig. (50)). In the saturation regime, the simulation coherence length (solid line) dropped below the theoretical prediction (by ~25% at $\beta_0^2 = 50$) and the HWHM (dotted line) mirrored this decrease. For strong turbulence, the first order perturbation theory basis for coherence length appears to lose validity, as it did for the normalized irradiance variance in the saturation regime.

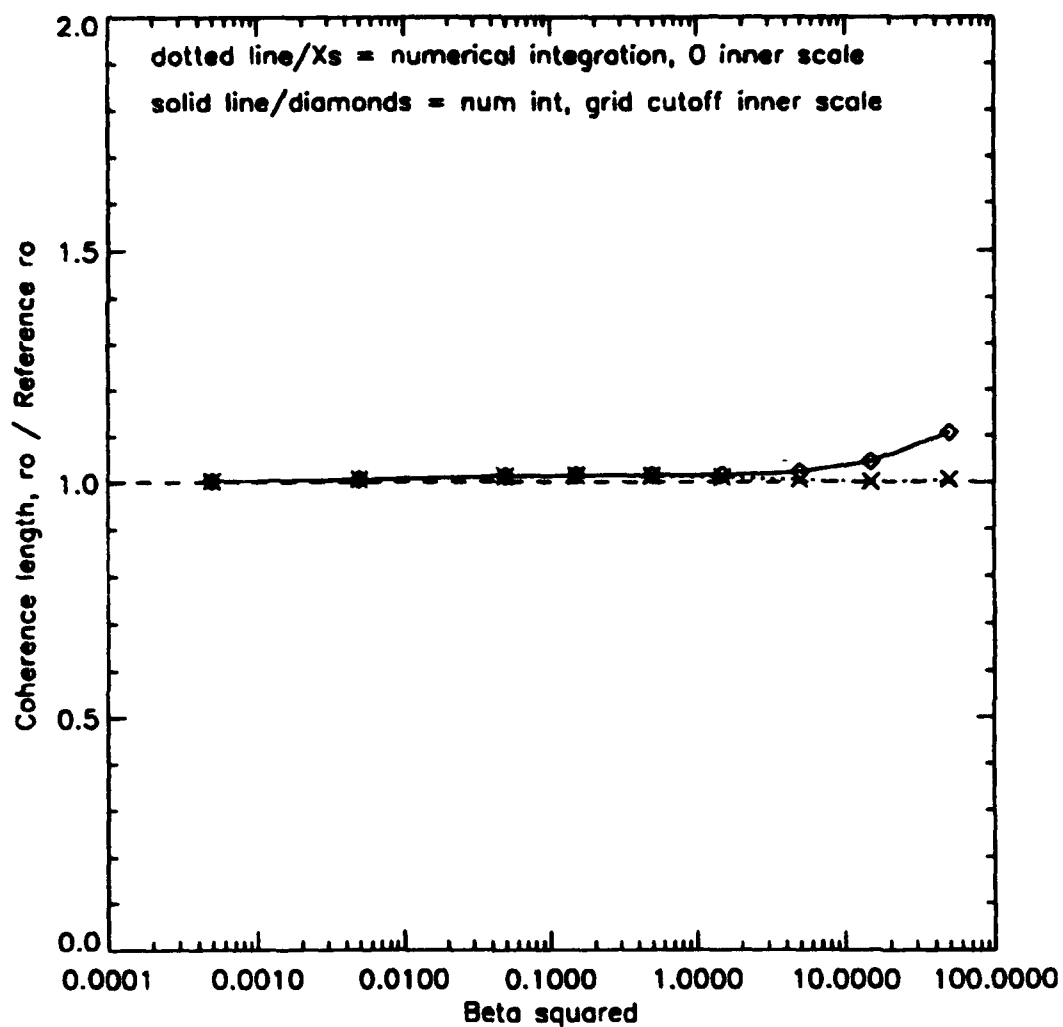


Figure 61 Coherence length from numerical integration for grid cutoff inner scale versus turbulence strength. Values normalized by Kolmogorov turbulence zero inner scale coherence length.

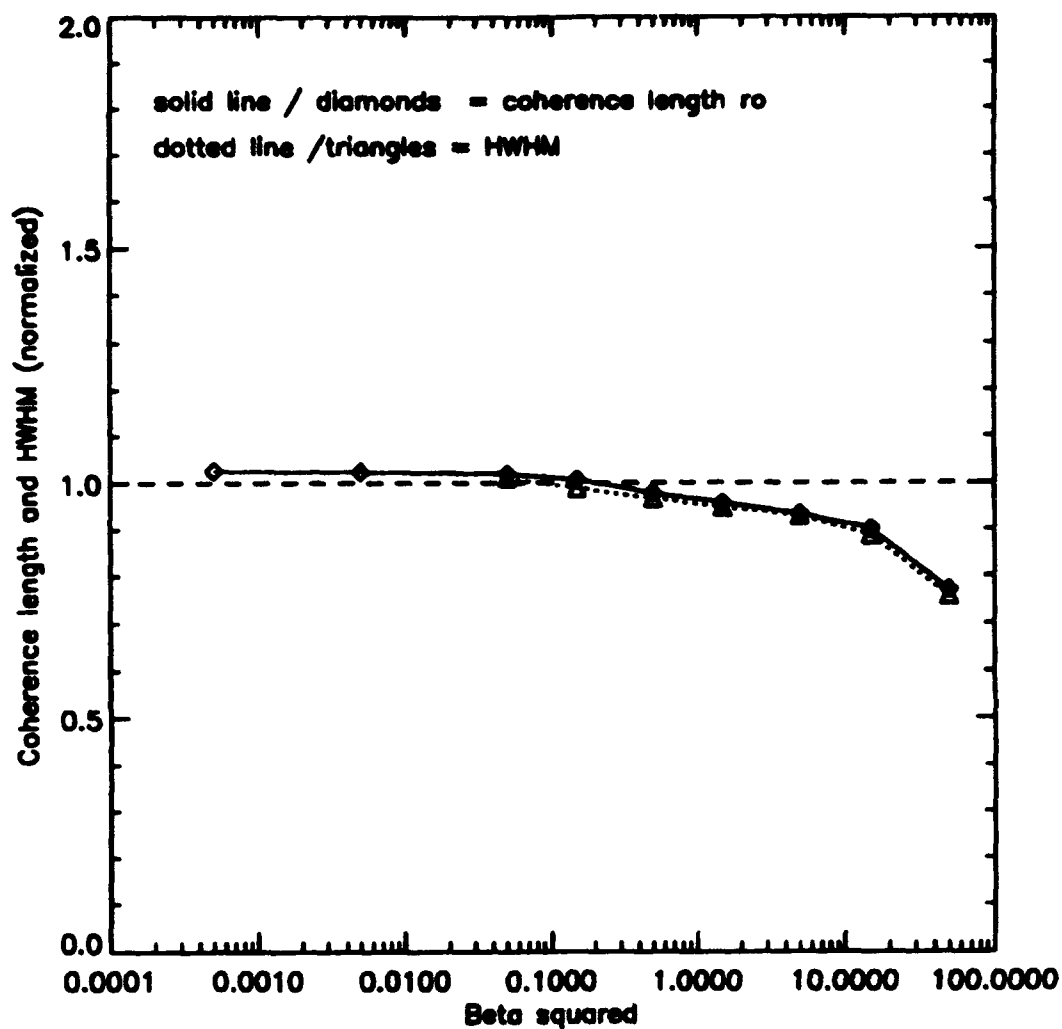


Figure 62 Coherence length r_0 (solid line) and HWHM (dotted line) for spherical wave propagation through turbulence (Values normalized by theoretical coherence lengths).

The drop in coherence length presumably came from strong scattering in high turbulence, but a possible origin in the computer simulation was also considered. The simulations started with an approximate point source to emulate spherical divergence of the E-field and required the E-field to remain basically confined within the simulation grid over the propagation. The resulting E-field properties could have differed from those of a true spherical wave. To investigate this possibility, the width of the final irradiance pattern was varied such that wider final irradiance fields (hence narrower sources) more closely approximated a true point source. Figure (63) plots the results and shows that increasing the final irradiance width (diamond, then triangle, then square, then X) actually lowered the coherence length in the saturation regime while still following the theory in the Rytov regime. This behavior indicated that the observed decrease in the saturation regime was physical and not due to simulation constraints.

To further investigate this phenomenon, beam wave (i.e. divergence intermediate between spherical and plane waves) and plane wave approximations were propagated on a 512x512 grid in which the width of the source varied from 4 grid elements (Δx) to 384 grid elements (3/4 of the grid width). Figure (64) plots the resulting coherence lengths and indicates that, based on the behavior in the Rytov regime, the 4 Δx source (circles) produced the spherical wave having large divergence of the E-field, the intermediate

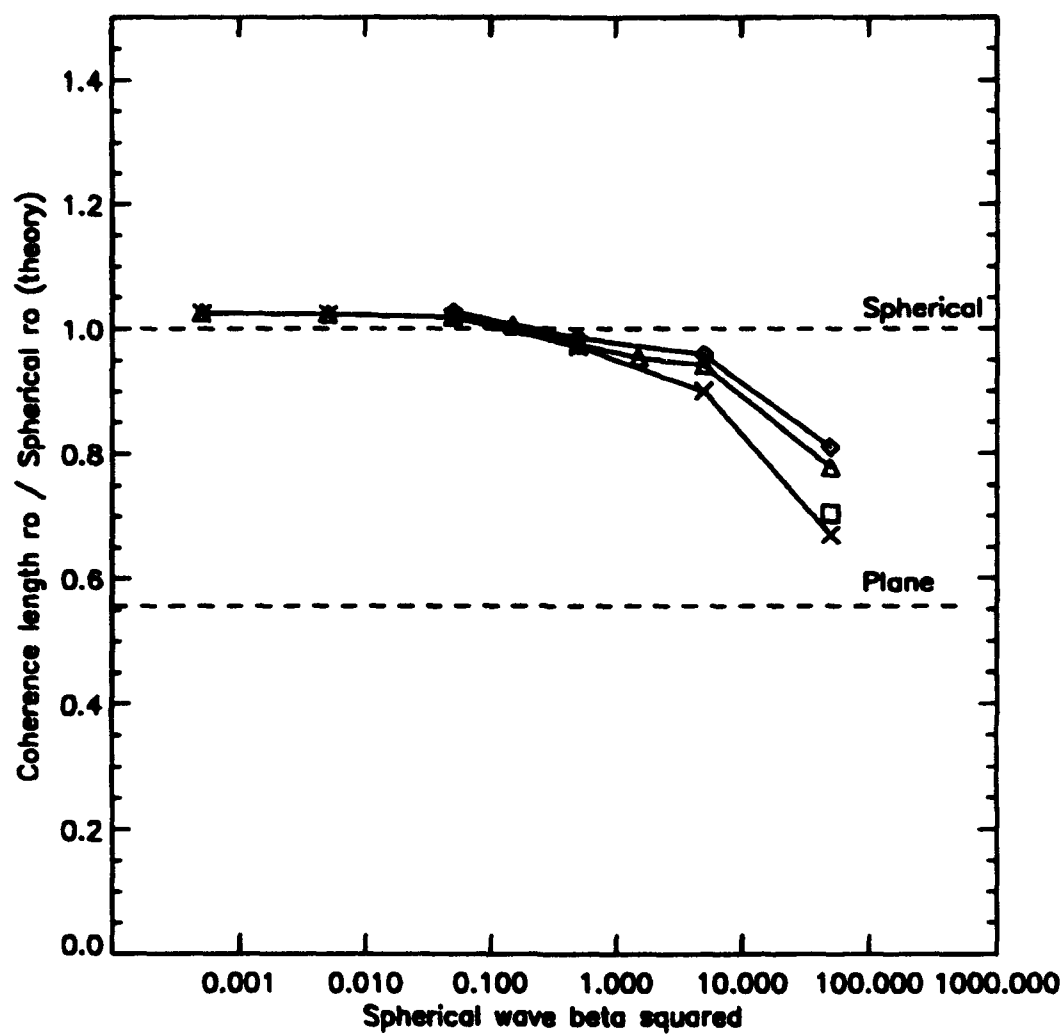


Figure 63 Coherence lengths r_0 for varying amounts of spherical divergence, hence final irradiance pattern width: diamond = $4/8$, triangle = $5/8$, square = $6/8$, X = $7/8$ grid width.

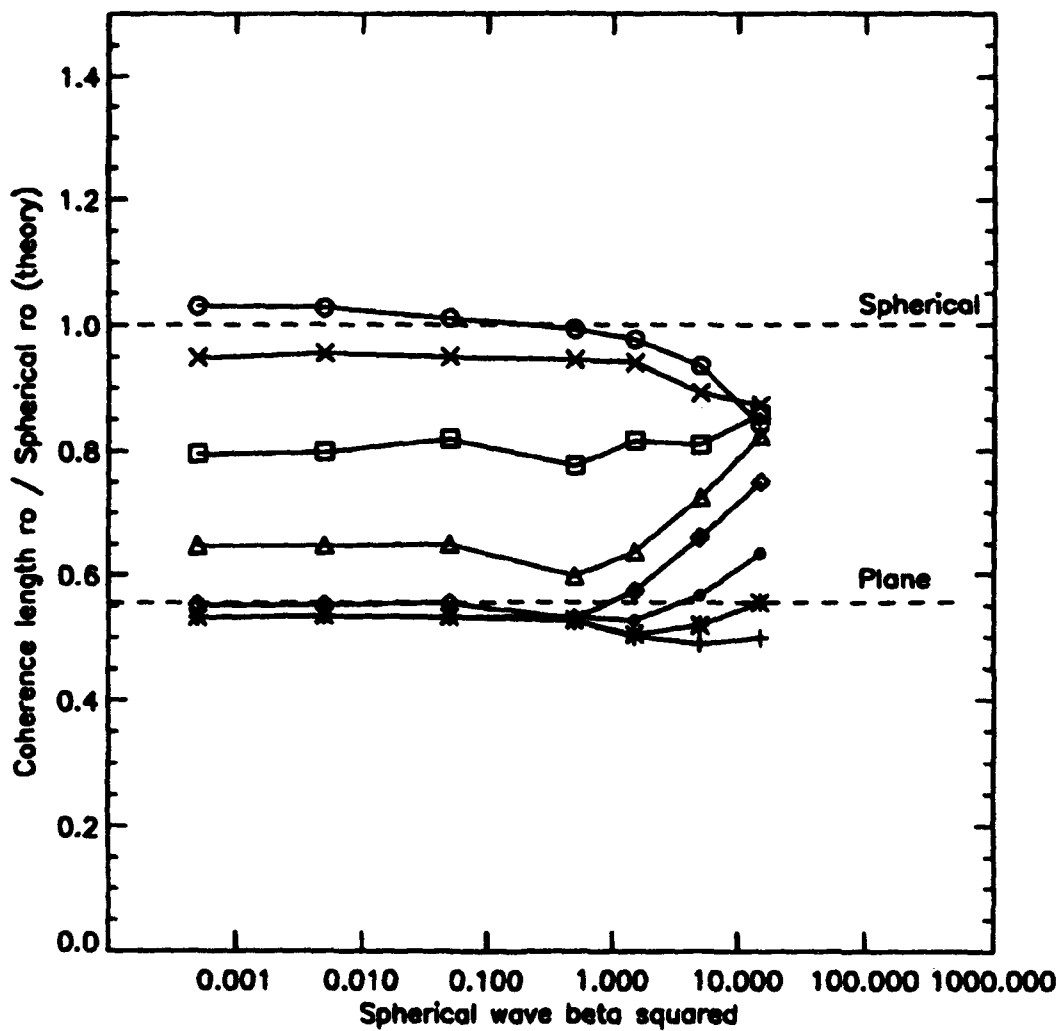


Figure 64 Coherence lengths for increasing source width on a 512x512 grid: circles= $4\Delta x$ (spherical wave); X's= $8\Delta x$, squares= $16\Delta x$, triangles= $32\Delta x$, diamonds= $64\Delta x$, dots= $128\Delta x$, asterisks= $256\Delta x$, pluses= $384\Delta x$ (plane wave).

source sizes ($X=8 \Delta x$, square = $16 \Delta x$, triangle = $32 \Delta x$, diamond = $64 \Delta x$) produced beam wave divergences, and wide sources (dot = $128 \Delta x$, asterisk = $256 \Delta x$, plus = $384 \Delta x$) produced plane waves.

However, as the turbulence strength approached the saturation regime, the behaviors changed. The spherical-type propagation coherence length dropped $\sim 15\%$ at $\beta_0^2 = 15$, the beam wave propagations actually increased in coherence length, and the plane wave propagations first decreased $\sim 5\%$ before increasing $\sim 15\%$ at $\beta_0^2 = 15$. Some of the unevenness in the beam wave coherence lengths occurred because smaller regions of the E-field were used to calculate the coherence lengths due to the relatively small size and divergence of these waves.

The cause of these behaviors requires further investigation, but a hypothesis can be made. As noted earlier, the spherical wave coherence length probably decreased below theory for strong turbulence where the Rytov-Tatarski first order perturbation theory was no longer valid. Strong scattering may have induced spherical divergence of the beam waves, increasing the coherence length, and caused the plane wave approximations to diverge like beam waves for high turbulence.

Recapping the above results, investigations of coherence length via computer simulation indicated that first order perturbation theory for coherence lengths loses validity in the saturation regime, just as it did for normalized

irradiance variance. The behavior of coherence length in the saturation regime for spherical, beam, and plane wave cases requires further research.

These investigations then examined the effect of inner scale upon coherence length for a spherically diverging beam, utilizing the 1024x1024 realizations run for the normalized irradiance variance calculations. Figure (65) shows the coherence length r_0 from numerical integration of Eq. (61) for Gaussian inner scales of 5, 10, and 15 cm. The Gaussian inner scale made the coherence lengths larger by reducing the energy at high spatial frequencies. Larger inner scales monotonically produced larger coherence lengths from numerical integration at a given turbulence strength ($\sim 8\%$ larger at $\beta_0^2 = 1$ (beginning of saturation regime) for $l_0 = 15$ cm). A plot of HWHM from numerical integration for Gaussian inner scales would appear similar since the theoretical HWHM is proportional to the Kolmogorov coherence length r_0

$$HWHM = 0.382 r_0. \quad (147)$$

Figure (66) shows the coherence length r_0 and Fig. (67) shows the HWHM from wave optics computer simulations with Gaussian inner scales of 5, 10, and 15 cm (solid lines), superimposed upon the numerical integration predictions of Fig. (65) (dotted lines). The r_0 and HWHM simulation values agreed well with theory for $\beta_0^2 < 0.1$, but started deviating from theory even before $\beta_0^2 = 1$, i.e. the onset of saturation for the normalized irradiance variance. In the saturation regime, computer simulation r_0 and HWHM still

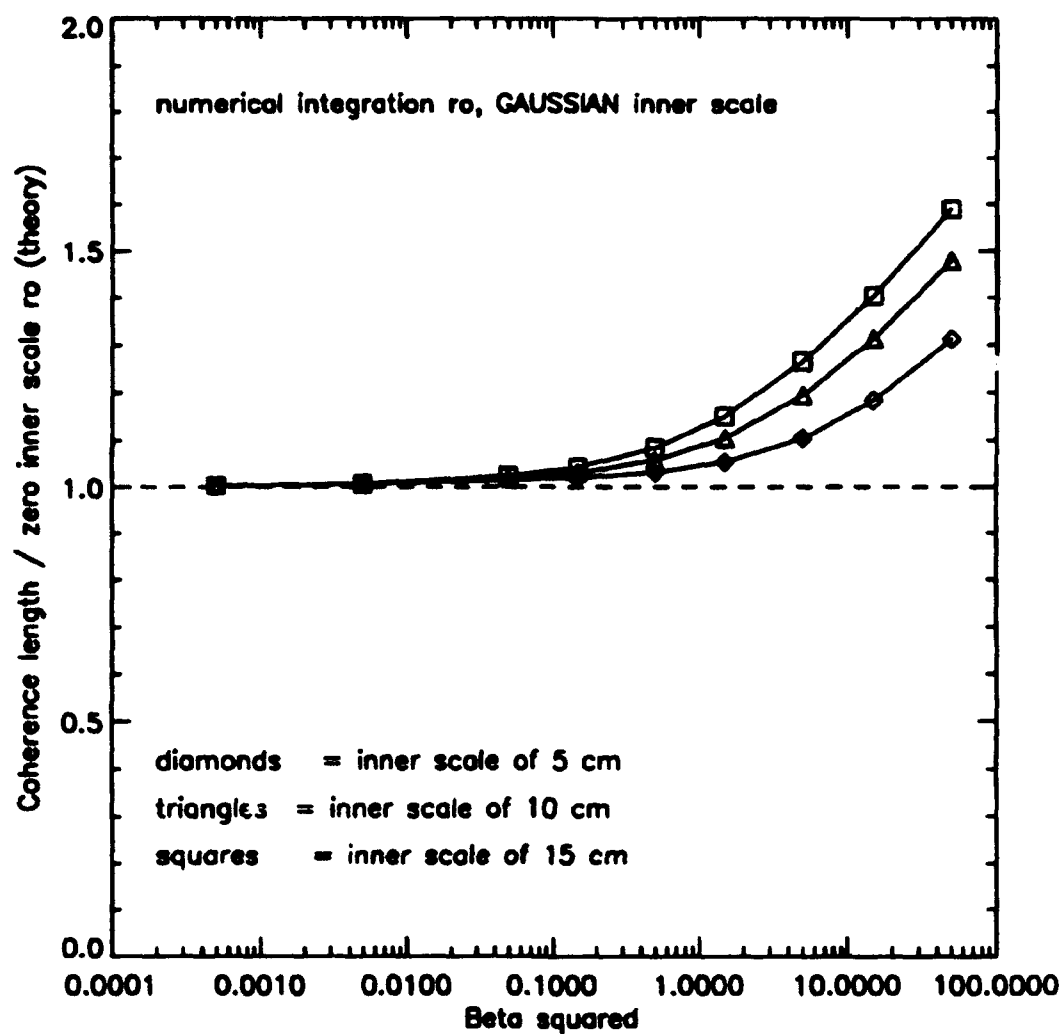


Figure 65 Coherence length r_0 from numerical integration for Gaussian inner scales of 5, 10, and 15 cm, normalized by the theoretical zero inner scale coherence lengths.

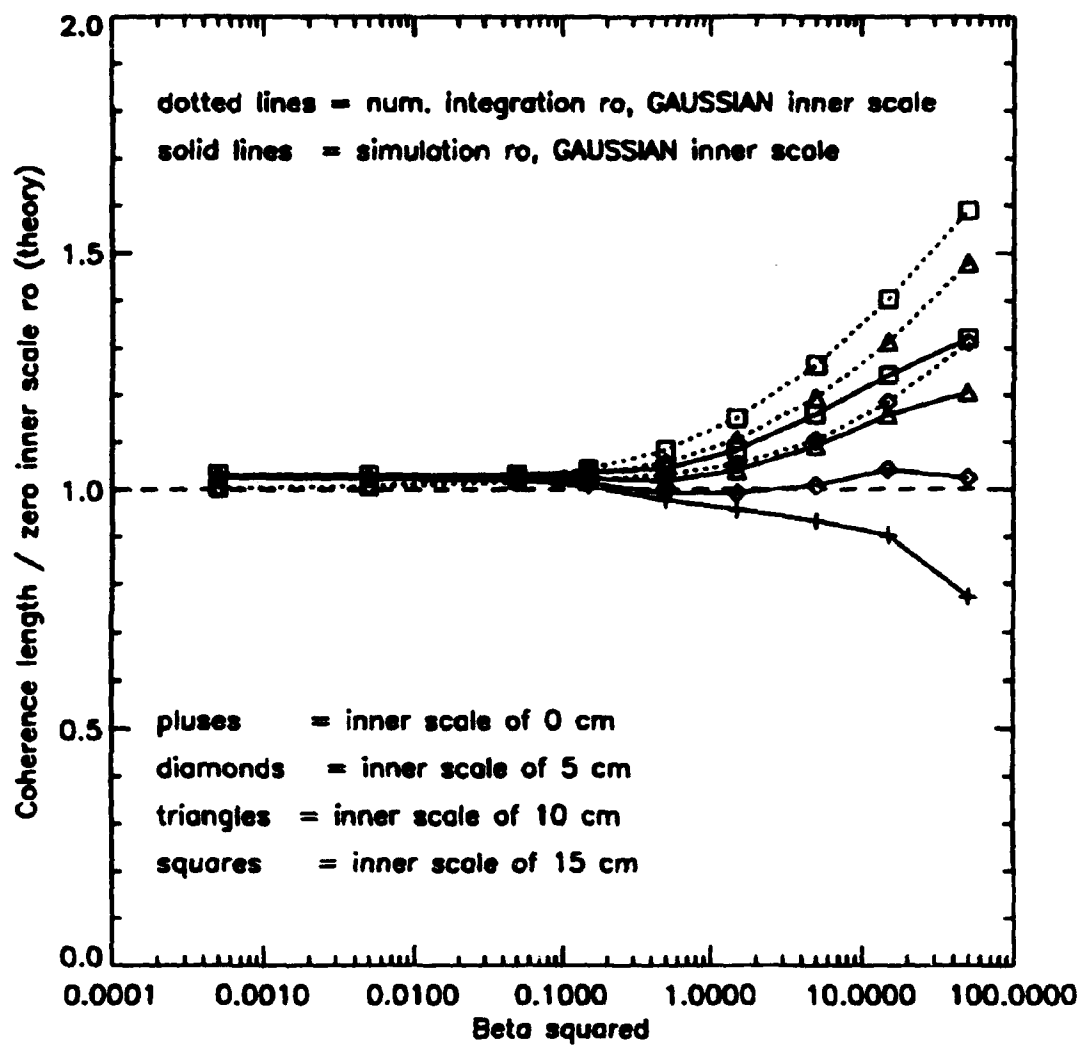


Figure 66 Coherence lengths r_0 from computer simulation with Gaussian inner scales of 5, 10, and 15 cm; values normalized by the theoretical zero inner scale coherence lengths.

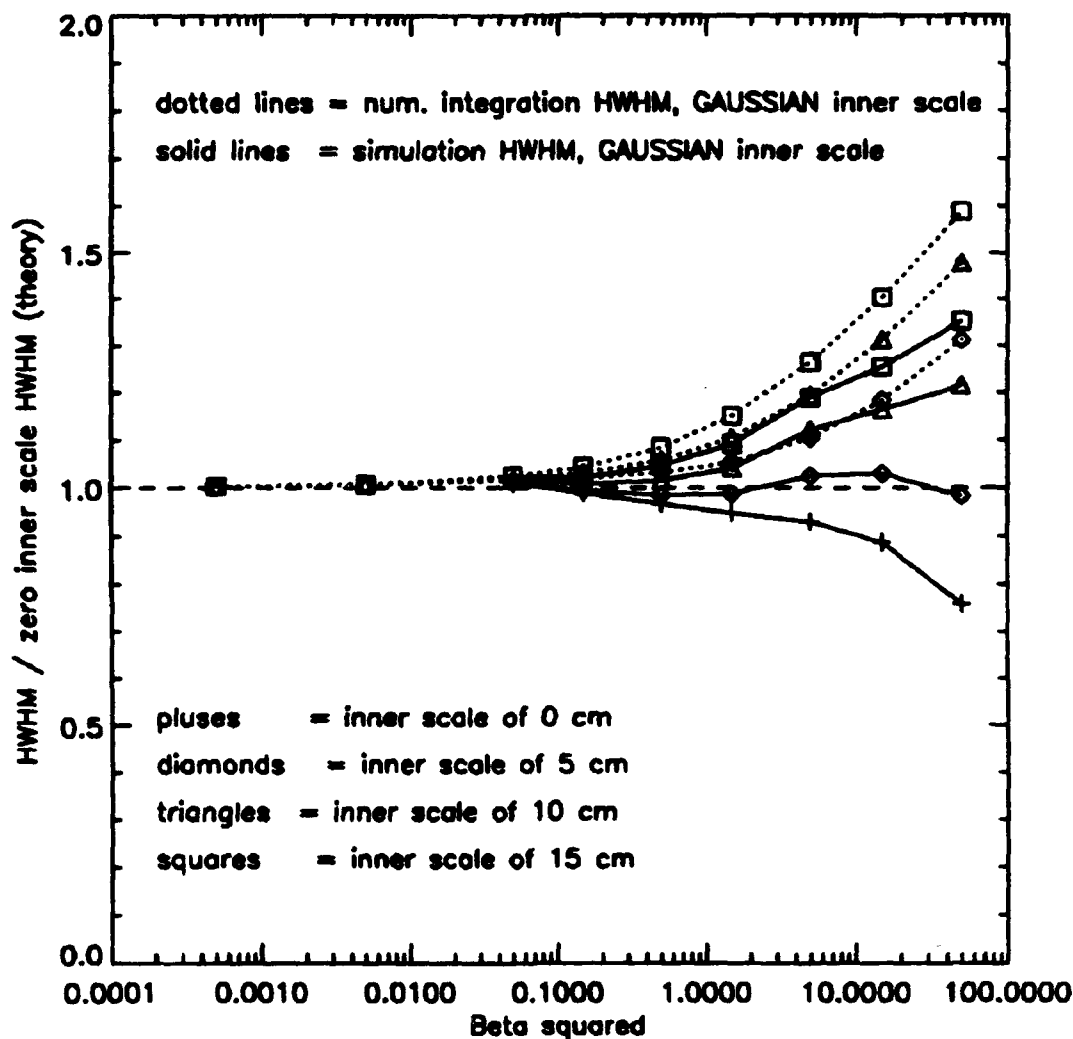


Figure 67 HWHM's from computer simulation with Gaussian inner scales of 5, 10, and 15 cm; values normalized by the theoretical zero inner scale HWHM's.

agreed well with each other, and their behavior showed a combination of decrease in coherence length due to saturation regime turbulence and increase in coherence length due to inner scale.

To elucidate the effects of inner scale by itself, Figs. (68) and (69) show the same plots of computer simulation coherence length r_0 and HWHM, but now normalized by the computer simulation zero inner scale r_0 and HWHM values, respectively, effectively removing the saturation contribution. These plots clearly show that, even in the saturation regime, inner scale increased the coherence length (solid lines) similarly to the predictions of theory (dotted lines).

The next set of figures plots coherence length and HWHM for propagations through turbulence with the Hill viscous-convective enhancement inner scale. Figure (70) plots the predicted coherence lengths from numerical integration of Eq. (61). Note that the numerical integration coherence lengths dropped ~5% in the range $\beta_0^2 = [0.1, 1]$ before increasing for higher turbulence strength. Figures (71) and (72) plot the computer simulation coherence lengths r_0 and HWHM, normalized by the theoretical values for spherical waves. In the Rytov regime, the coherence length r_0 decreased (~5% for $l_0 = 15$ cm) even for very low turbulence ($\beta_0^2 < 0.1$)z, but then increased in the saturation regime as for the Gaussian inner scale. Figures (73) and (74) plot the same coherence lengths r_0 and HWHM's but divided by the zero inner scale computer simulation values to emphasize the effect of inner scale. Figure (73) clearly shows the

small decrease in coherence length r_0 in the Rytov regime, and both plots show the general agreement between theory and computer simulation for the effect of inner scale upon coherence length in the saturation regime. In summary, the inner scale increased the coherence length in the saturation regime as much as 50% compared to the zero inner scale case, and more than compensated for the decrease from strong scatter.

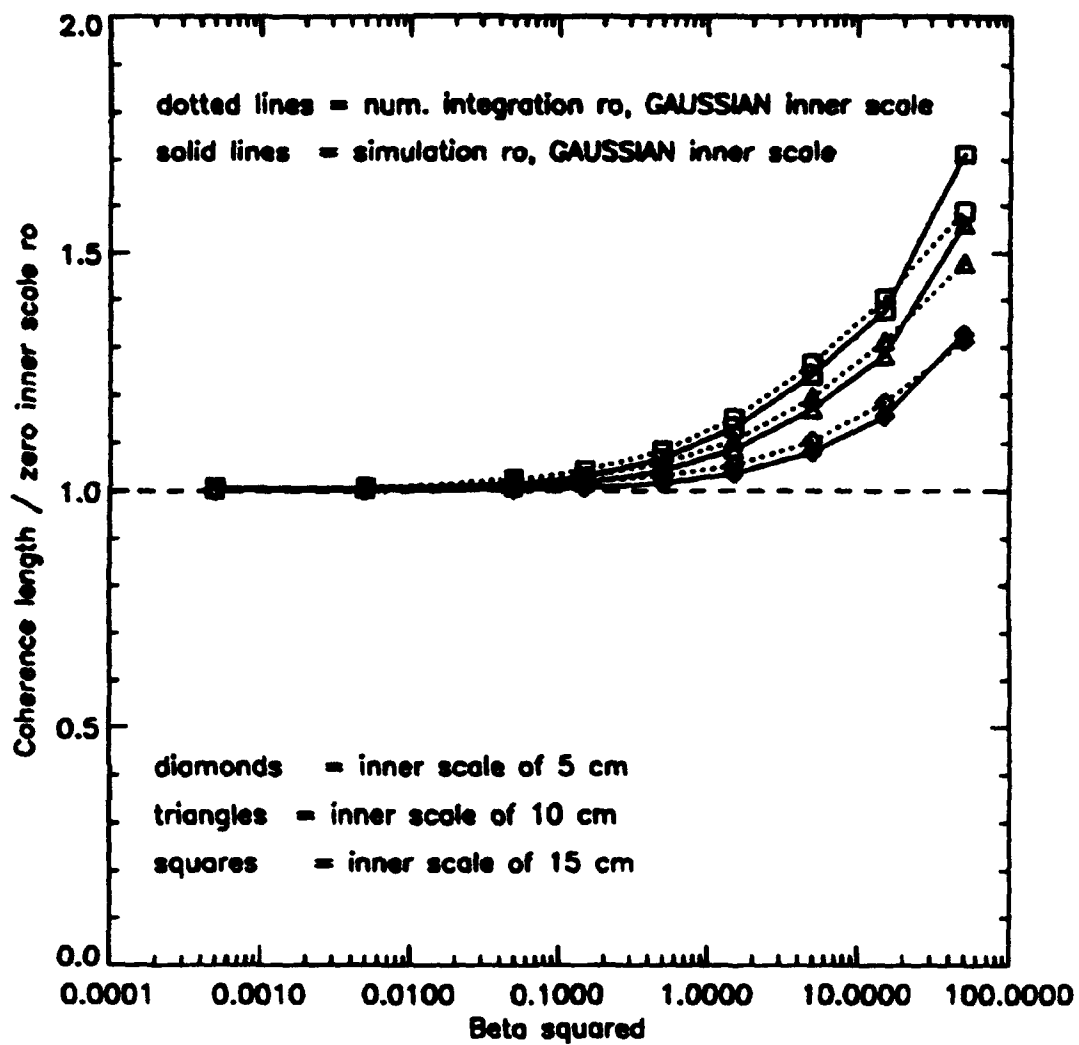


Figure 68 Coherence lengths r_0 from computer simulation for Gaussian inner scales of 5, 10, and 15 cm; values normalized by computer simulation zero inner scale r_0 .

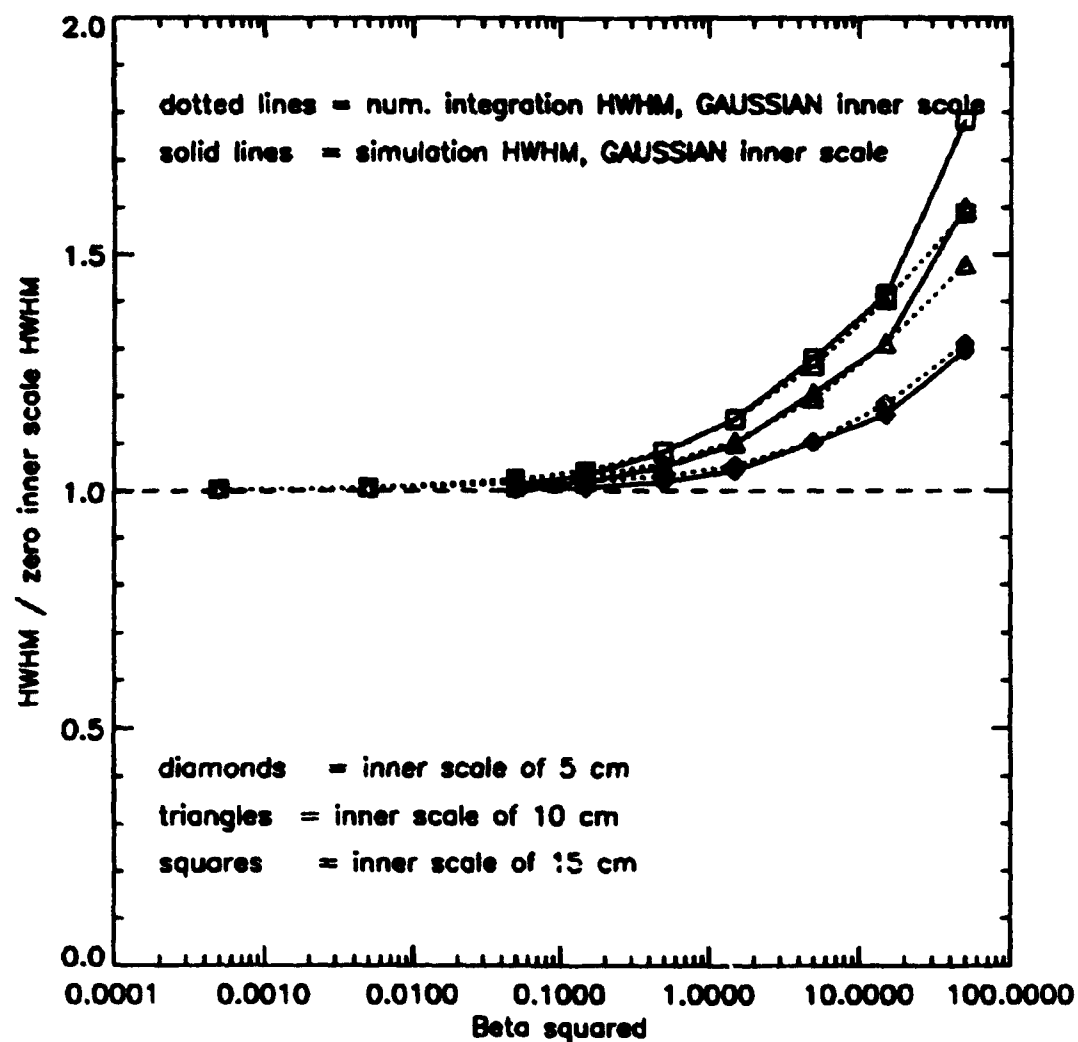


Figure 69 HWHM's from computer simulation with Gaussian inner scales of 5, 10, and 15 cm; valued normalized by computer simulation zero inner scale HWHM's.

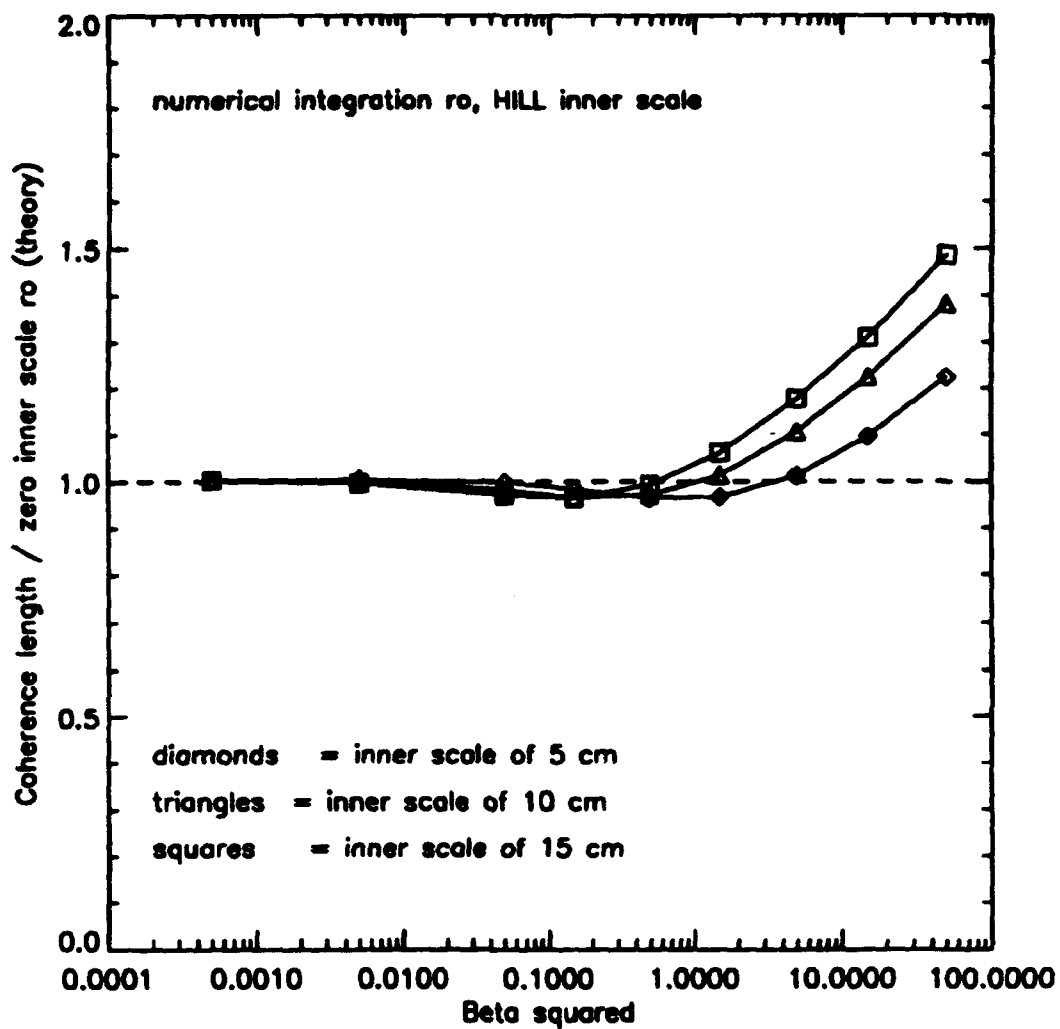


Figure 70 Coherence length r_0 from numerical integration for Hill viscous-convective enhancement inner scales of 5, 10, and 15 cm, normalized by the theoretical zero inner scale coherence length.

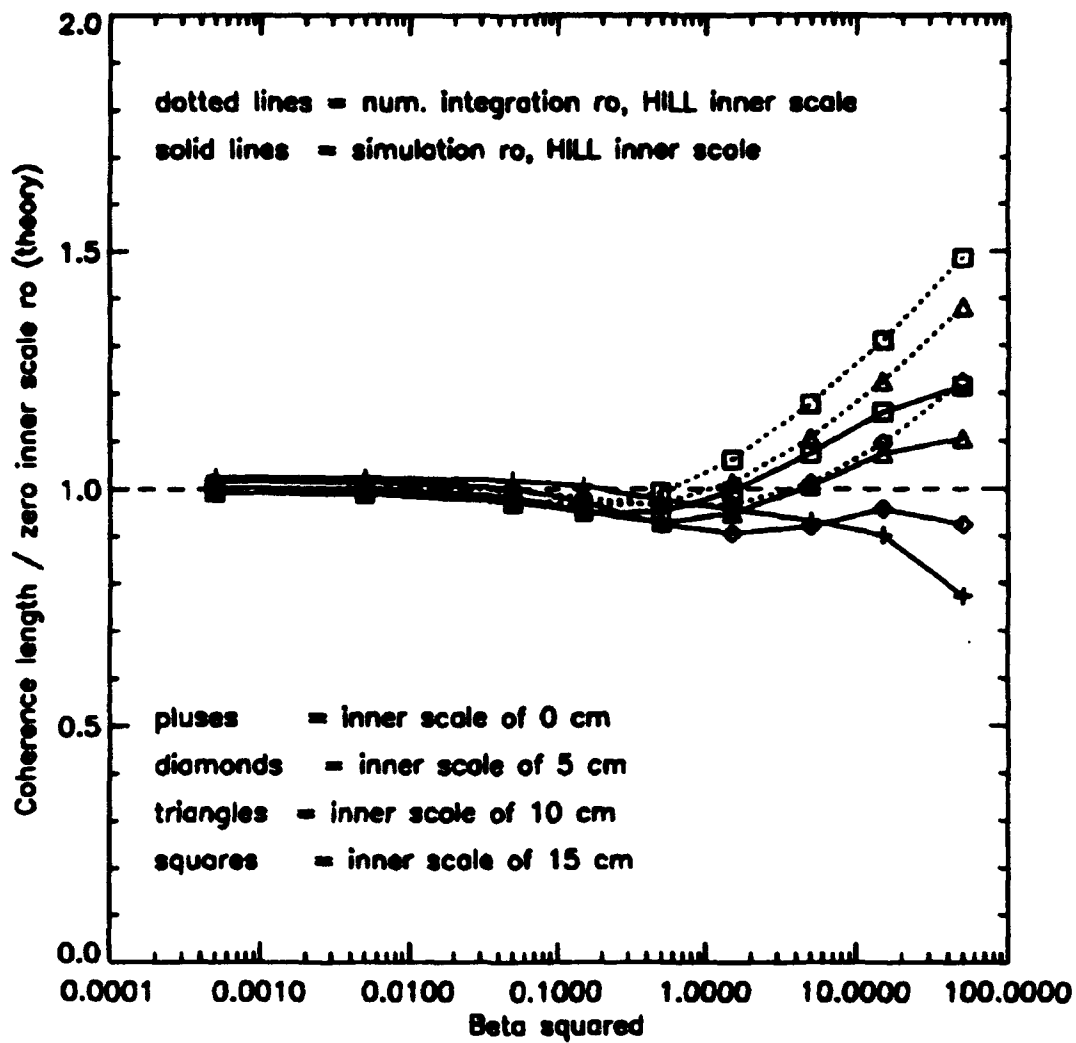


Figure 71 Coherence lengths r_0 from computer simulation with Hill viscous-convective enhancement inner scales of 5, 10, and 15 cm; values normalized by the theoretical zero inner scale coherence lengths.

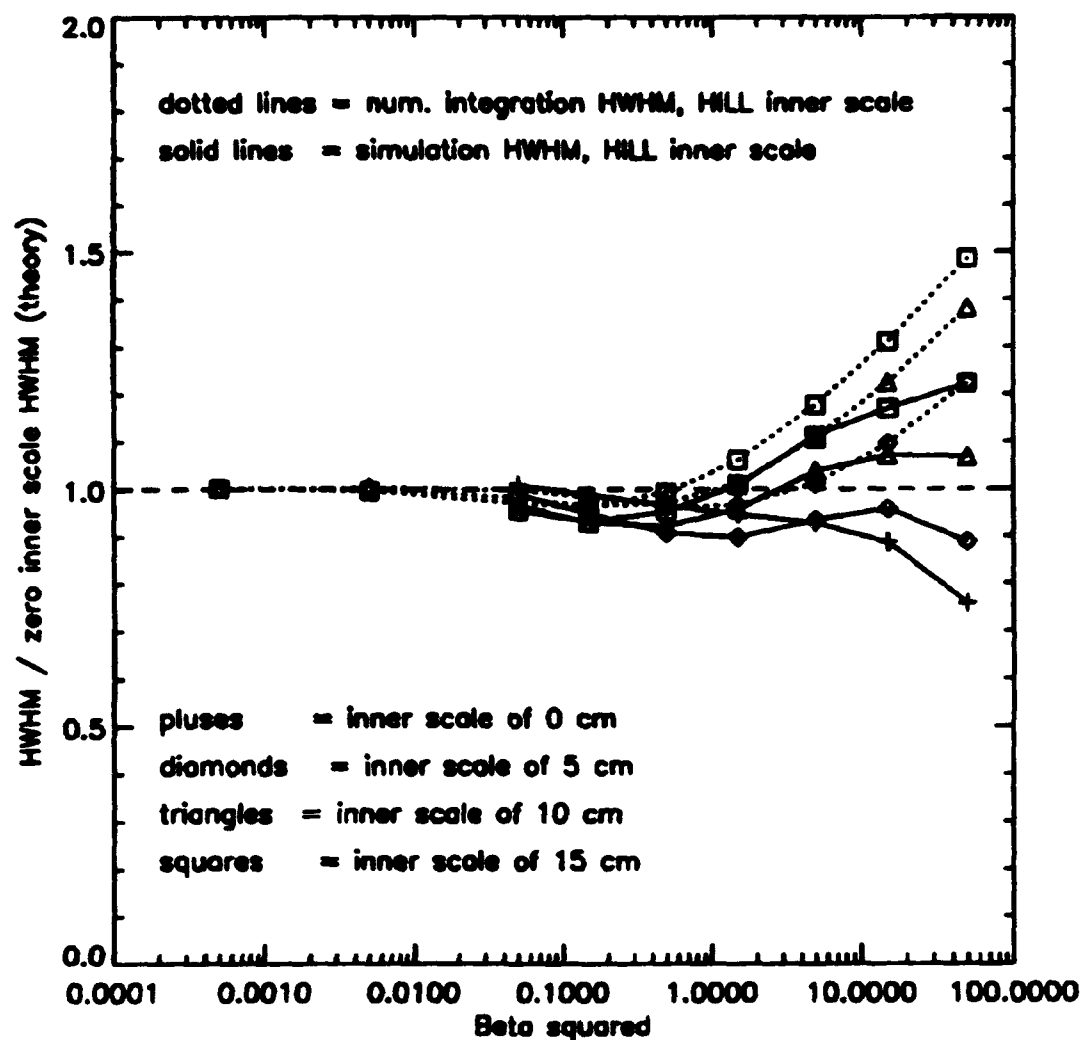


Figure 72 HWHM's from computer simulation with Hill viscous-convective enhancement inner scales of 5, 10, and 15 cm; values normalized by the theoretical zero inner scale HWHM's.

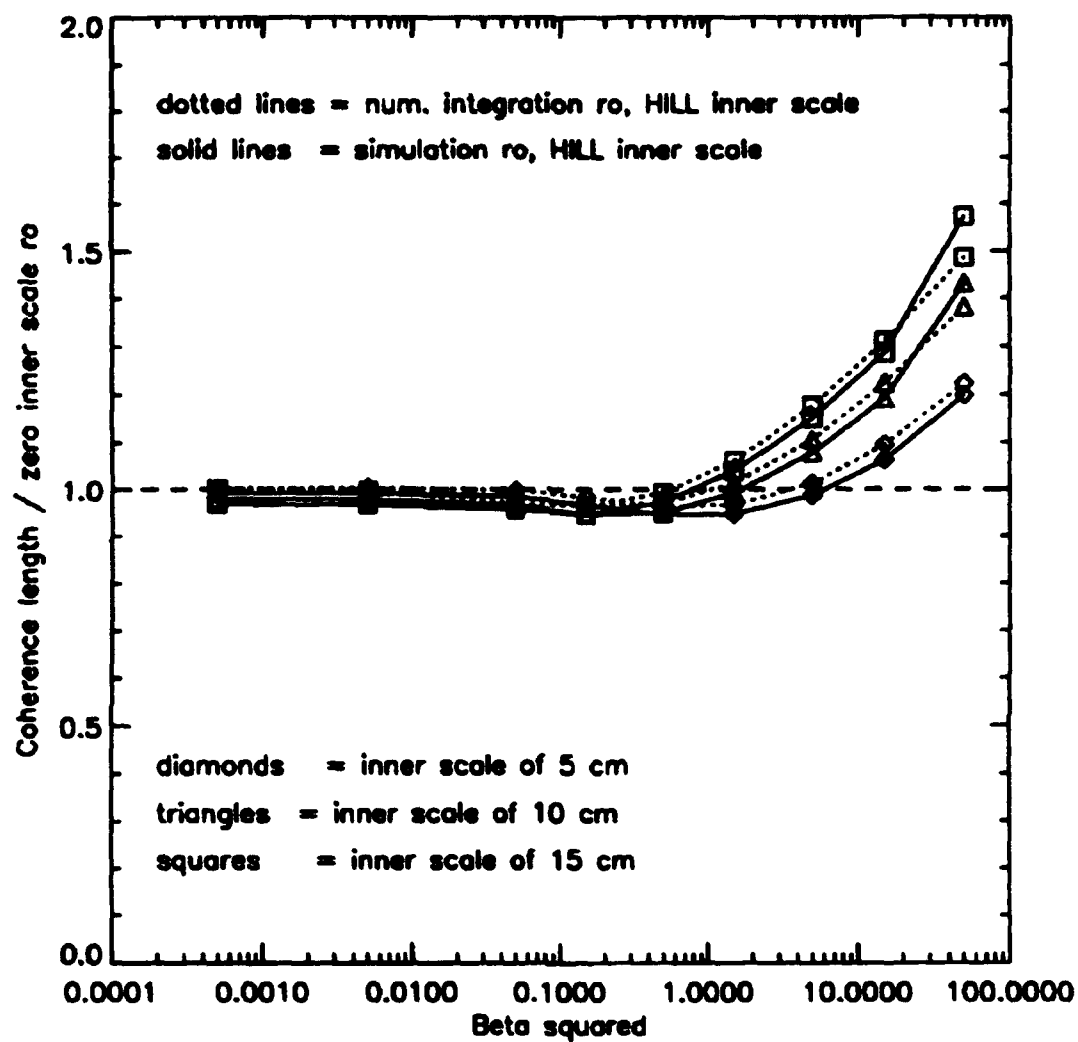


Figure 73 Coherence lengths r_0 from computer simulation for Hill viscous-convective enhancement inner scales of 5, 10, and 15 cm; values normalized by computer simulation zero inner scale r_0 .

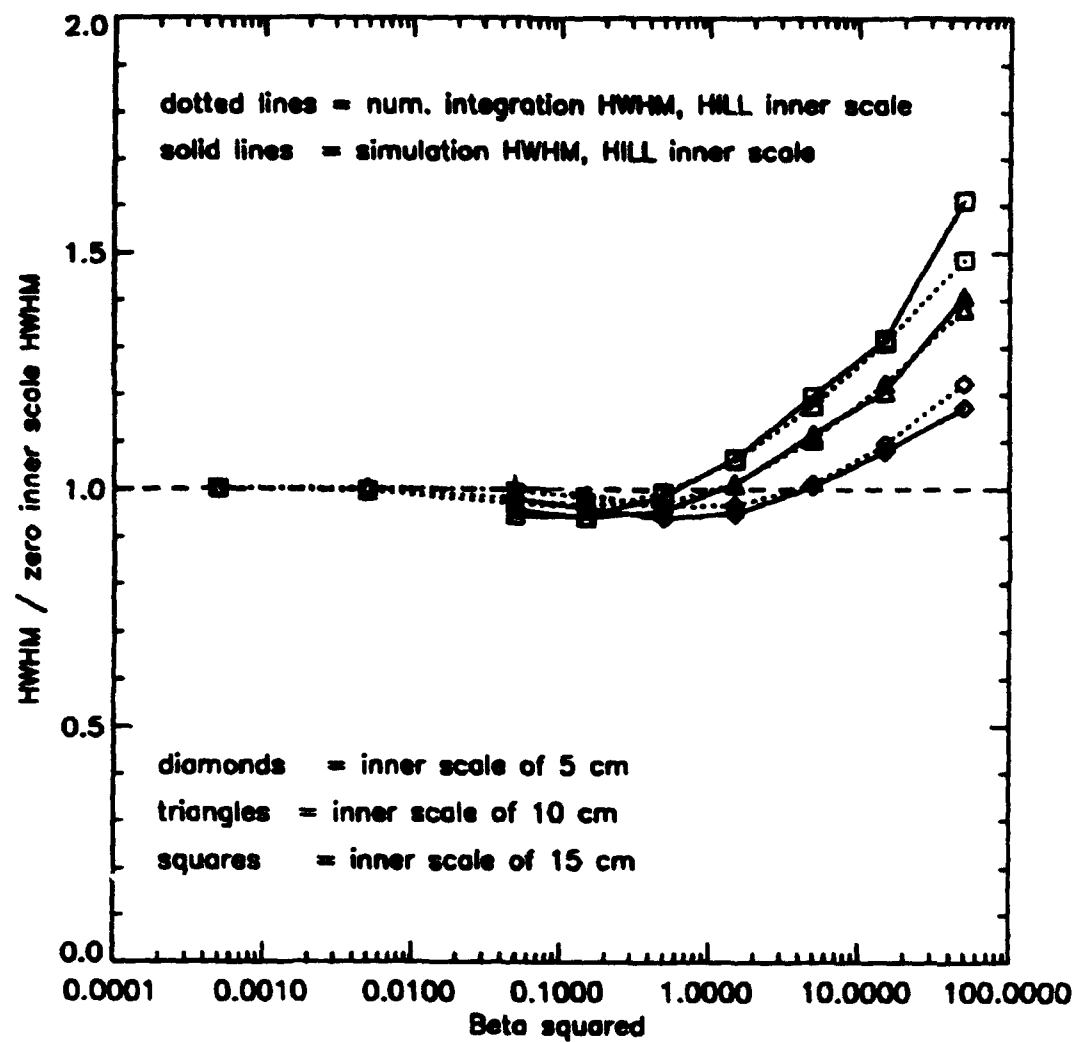


Figure 74 HWHM's from computer simulation with Hill viscous-convective enhancement inner scales of 5, 10, and 15 cm; valued normalized by computer simulation zero inner scale HWHM's.

V. CONCLUSIONS

Variations in the index of refraction within a turbulent medium alter an E-field propagating through the medium. The Rytov-Tatarski, perturbation theory predicts the effects of the turbulence upon the irradiance statistics and coherence length of the propagating E-field. Computer simulations modeled the propagation of the E-field through the turbulent medium, producing irradiance and coherence statistics to compare with theoretical results.

These investigations used a split-step, Huygens-Fresnel, wave optics, computer simulation to model an E-field propagating through a turbulent stratosphere. The limits of validity of the simulations were determined based upon aliasing considerations, choice of source, and robustness of statistical calculations, and produced the following guidelines:

- The element size for an NxN grid should satisfy $\Delta x = \sqrt{\lambda L / N}$.
- The maximum turbulence strength for which an NxN grid produces valid E-fields is given by $\beta_0^2 \approx 0.1 N^{0.9}$.
- A coherence length $r_0 \approx 2.5 \Delta x$ corresponds to the maximum turbulence strength for which an NxN grid produces valid E-fields.
- The number of phase screens should be ≥ 30 .
- The number of realizations should be ≥ 30 .
- Low spatial frequency corrections to phase screens improve the accuracy of the normalized irradiance variance by 5% and of the E-field coherence length by 30%.

- Half width at half maximum of the atmospheric MTF and an iterative fit r_0 provide the most stable parameterizations of the E-field coherence length.
- Telltale signs of aliasing include a fine-grained irradiance pattern, a boxed perimeter of the irradiance pattern, and peaking of energy toward the center of the computation grid.

This research investigated the effect of (1) zero inner scale, (2) Gaussian inner scale, (3) Hill's and (4) Frehlich's viscous-convective enhancement inner scales, and (5) grid cutoff inner scale on the normalized irradiance variance of a spherical wave propagating through a turbulent medium. For the Rytov regime, the normalized irradiance variances with grid cutoff, Gaussian, and Hill/Frehlich viscous-convective enhancement inner scales were compared to the zero inner scale case and to the values from numerical integration of the Rytov-Tatarski predictions. For low turbulence strengths, the variances obtained from the simulations agreed within 2% of the values from the numerical integrations. The grid cutoff inner scale, implicit in discrete grid wave optics computer simulations, affected the variance negligibly compared to a true zero inner scale at low turbulence strengths with the large 1024x1024 grid. Application of a Gaussian inner scale reduced the normalized irradiance variance as much as 40% for small β_0^2 compared to the zero inner scale case. The more realistic Hill viscous-convective enhancement inner scale raised the normalized irradiance variance by up to 30% for smaller inner scale values, but for larger values of inner scale eventually reduced the variance below the zero inner

scale value as much as 30%. The latter contrasted with the behavior in the saturation regime ($\beta_0^2 > 1$) where larger inner scales continually enhanced the normalized irradiance variance. The Frehlich parameterization of the viscous-convective enhancement gave normalized irradiance values that agreed within 3% of the Hill inner scale values over the entire range of turbulence strengths investigated.

The coherence of the E-field was studied by computing the average atmospheric MTF from the propagated fields. Parameterizing the MTF with a coherence length r_0 and half width at half max (HWHM) allowed comparison of the coherence length of the E-field with the predicted coherence length from the Rytov-Tatarski-Fried theory. In the Rytov regime, simulation coherence lengths and HWHM's for spherical and plane wave approximations agreed within 5% of the theoretical coherence lengths/HWHM's for zero inner scale. However, in the saturation regime, the spherical wave coherence length decreased as much as 25% below the theory. Similar decreases resulted for different widths of the final E-field. Beam wave approximations gave coherence lengths that increased toward the spherical wave values in the saturation regime, while plane wave approximations deviated from ~5% below to ~15% above the theory in the saturation regime. Increasing inner scale increased the coherence length of a spherically diverging E-field by up to 50% relative to the zero inner scale

case in the saturation regime. The amount of the increase agreed with numerical predictions from the analytic theory.

Several avenues for further research exist. Larger grid sizes and finer mesh could explore the behavior of normalized irradiance variance and coherence length at higher turbulence strengths. In particular, the behavior of coherence length for spherical, beam, and plane waves in strong turbulence conditions need a more precise description. The atmospheric MTF's from simulation and theory could be compared directly, rather than through a coherence length parameterization, and the structure functions could also be calculated and compared directly to investigate whether the 2/3 power law structure function holds in saturation. Simulations could allow $C_n^2(z)$ to vary along the path and could include an outer scale in the spectrum of refractive index fluctuations to study the effects of large scale anisotropy of atmospheric turbulence on normalized irradiance variance and coherence length (possibly basing the $C_n^2(z)$ variations upon high frequency radar data that can resolve the large scale variations down to about 300 m). Larger (> 1 Gbyte RAM) and faster computing resources would provide the catalyst for all such further investigations of the propagation of an E-field through turbulence.

APPENDIX

Sample listing of YAPS event input file:

<u>EVENTS:</u>	<u>EXPLANATION:</u>
t 7	;debug flag and random number seed
0.0 0.053033	;zenith angle and r_0 at 0.5 microns
2	;number of wavelengths
0.5e-6 0.5e-6	;list of wavelengths
'surf' 'beam' 0 0 0 2.531058298 0.0 0.0 0.00	;surf name, vertex location, clear aperture, ;super-Gaussian exponent, inner scale
'surf' 'atmos1' 0 0 6250 8.0 0.0 0.0 0.00	;surf name, vertex location, clear aperture, ;super-Gaussian exponent, inner scale
'prof' 1024 1024 0.009886946 'none' 'dummy'	;surface size, grid element size, file flags
'end'	;end of surface summary
2 1024 1024	;number of fields and dimensions
'times' 0.0 0.090002	;time initialization
'thread' 0.0 1.0 1	;propagation start
'finit' 1 0.009886946 2 0 0 0 1 0 0 200000 +1	;initialize field
'apsrf' 1 1 'beam'	;apply aperture profile
'aptou' 1	;convert from amplitude/phase to complex
'chgfcsc' 1 0 0 1.0e+30	;change focus to apply spherical phase
'prop' 1 0 0 200000	;back propagate to create source
'fldcp' 1 2	;copy field to use as source later
'prop' 2 0 0 0	;propagate
'openfl' '/data/davis/c118' 11	;open field output file
'chgfcsc' 2 0 0 200000	;remove spherical phase from field
'svflddx' 2 11 385 640 385 640	;save field to output file
'fldcp' 1 2	;copy source field to working grid

(following three steps repeated 32 times to propagate a distance L)

```
'prop' 2 0 0 193750           ;propagate field
'mkscrm' 6250.0 1.0e-18 193750.0 'atmos1'
                                   ;create phase screen for  $\Delta z$ ,  $C_n^2$ , position
'apsrf' 2 1 'atmos1'           ;apply phase screen to field
```

(save the field)

```
'chgfcfs' 2 0 0 200000        ;remove spherical phase from field
'svflddx' 2 11 385 640 385 640 ;save field to output file
'fldcp' 1 2                    ;copy source field to working grid
```

(repeat above propagation 30 times)

.....
.....

```
'closefl' 11                   ;close output file
'end'                           ;end simulation
```

LIST OF REFERENCES

- Born, M. and Wolf, E., *Principles of Optics*, 5th edition, Pergamon Press, 1970.
- Cochran, G., "Phase screen generation", Report No. TR-663, The Optical Sciences Company, 1985.
- Codona, J.L., Creamer, D.B., Flatté, S.M., Frehlich, R.G. and Henyey, F.S., "Solution for the fourth moment of waves propagating in random media," *Radio Sci.* Vol. 21, No. 5, 805-814 (1986).
- Ellerbroek, B., United States Air Force Phillips Laboratory, Albuquerque, New Mexico (personal communication, 1993).
- Flatté, S.M., Wang, G. and Martin, J., "Irradiance variance of optical waves through atmospheric turbulence by numerical simulation and comparison with experiment," *J. Opt. Soc. Am. A* **10**, 2363-2370 (1993)
- Frehlich, R., "Laser scintillation measurements of the temperature spectrum in the atmospheric surface layer," *Journal of the Atmospheric Sciences*, Vol. 49, No. 16, 1494-1509 (1992).
- Fried, D.L., "Limiting resolution looking down through the atmosphere," *J. Opt. Soc. Am.*, Vol. 56, No. 10, 1380-1384, (1966).
- Fried, D.L., "Optical resolution through a randomly inhomogeneous medium for very long and very short exposures," *J. Opt. Soc. Am.*, Vol. 56, No. 10, 1372-1379 (1966).
- Goodman, J.W., *Introduction to Fourier Optics*, McGraw-Hill Book Company, 1968.
- Goodman, J.W., *Statistical Optics*, John Wiley & Sons, Inc., 1985.
- Hecht, E., *Optics*, Addison-Wesley Publishing Company, 1987.
- Hill, R.J. and Clifford, S.F., "Modified spectrum of atmospheric temperature fluctuations and its application to optical propagation," *J. Opt. Soc. Am.* **68**, 892-899 (1978).
- Hudgin, R.H., "Wave-front reconstruction for compensated imaging", *J. Opt. Soc. Am.*, Vol. 67, No. 3, 375-378, (1977)

Hufnagel, R.E., and Stanley, N.R., "Modulation transfer function associated with image transmission through turbulent media," J. Opt. Soc. Am., Vol. 54, No. 1, 52-61, (1964).

Ishimaru, A., *Wave Propagation and Scattering in Random Media*, Vol. II, Academic Press, 1978.

Knepp, D.L. "Multiple phase-screen calculation of the temporal behavior of stochastic waves," Proceedings of the IEEE, Vol. 71, No. 6, 722-737 (1983).

Kolmogorov, A., *Turbulence, Classic Papers on Statistical Theory*, (Friedlander, S.K. and Topper, L., editors) (Wiley-Interscience, 1961)

Lawrence, R.S. and Strohbehn, J.W., "A survey of clear-air propagation effects relevant to optical communications", Proc. of the IEEE, Vol. 58, No. 10, 1523-1545, (1970).

Martin, J.M. and Flatté, S.M., "Intensity images and statistics from numerical simulation of wave propagation in 3-D random media," Applied Optics, Vol. 27, No. 11, 2111-2126 (1988).

Martin, J.M. and Flatté, S.M., "Simulation of point-source scintillation through three-dimensional random media," J. Opt. Soc. Am. A Vol. 7, No. 5, 838-847 (1990).

Noll, R.J., "Zernike polynomials and atmospheric turbulence", J. Opt. Soc. Am., Vol. 66, No. 3, 207-211, (1976).

Roberts, P.H., "A Wave Optics Propagation Code", Report No. TR-760, The Optical Sciences Company, 1986.

Saleh, B.E.A., and Teich, M.C., *Fundamentals of Photonics*, John Wiley & Sons, Inc., 1991.

Tatarski, V.I., *Wave Propagation in a Turbulent Medium*, translated by R.A. Silverman (McGraw-Hill, New York 1961).

Walters, D.L., Naval Postgraduate School, Monterey, CA (personal communication, 1994).

Yura, H., presentation notes, The Aerospace Corporation, Los Angeles, CA, 1992.

INITIAL DISTRIBUTION LIST

		No. Copies
1.	Defense Technical Information Center Cameron Station Alexandria VA 22304-6145	2
2.	Library, Code 052 Naval Postgraduate School Monterey CA 93943-5002	2
3.	Dr. Donald L. Walters, Code PH/We Naval Postgraduate School Monterey, CA 93943	10
4.	Dr. David Fried, Code PH/F Naval Postgraduate School Monterey, CA 93943	1
5.	Dr. D. S. Davis, Code PH/Dv Naval Postgraduate School Monterey, CA 93943	1
6.	Dr. William B. Colson, Code PH/Cw Chairman, Physics Department Naval Postgraduate School Monterey, CA 93943	1
7.	Dr. James Miller, Code EC/Mr Naval Postgraduate School Monterey, CA 93943	1
8.	Dr. Barry Hogge, Attn: LI United States Air Force Phillips Laboratory Kirtland Air Force Base Albuquerque, New Mexico 87117	1

- | | | |
|-----|---|---|
| 9. | Dr. Russell Butts, Attn: LI
United States Air Force Phillips Laboratory
Kirtland Air Force Base
Albuquerque, New Mexico 87117 | 1 |
| 10. | Dr. Darrell Spreen, Attn: LI
United States Air Force Phillips Laboratory
Kirtland Air Force Base
Albuquerque, New Mexico 87117 | 1 |
| 11. | Dr. Brent Ellerbroek, Attn: LI
United States Air Force Phillips Laboratory
Kirtland Air Force Base
Albuquerque, New Mexico 87117 | 1 |
| 12. | Dr. Greg Cochrane, Attn: LI
United States Air Force Phillips Laboratory
Kirtland Air Force Base
Albuquerque, New Mexico 87117 | 1 |
| 13. | Jerry Lentz, Code PH/Lz
Naval Postgraduate School
Monterey, CA 93943 | 1 |
| 14. | LT Charles A. Davis
315 Grady Ave.
Tryon, N.C. 28782-3010 | 4 |